Planetesimal Formation in Weakly Turbulent Protoplanetary Disks

# Instabilities in Protoplanetary Disks and Their Effects on Planetesimal Formation in the Low Turbulence Limit

By Rishita Gudapati, B.Sc.

*A Thesis Submitted to the School of Graduate Studies in the Partial Fulfillment of the Requirements for the Degree Master of Science*

Master of Science (2022)

Department of Physics & Astronomy

McMaster University

Hamilton, Ontario

TITLE: Instabilities in Protoplanetary Disks and
Their Effects on Planetesimal Formation in
the Low Turbulence Limit

AUTHOR: Rishita Gudapati, B.Sc. (University of Waterloo)

SUPERVISOR: Dr. James Wadsley

NUMBER OF PAGES: 1, 107

# Abstract

This thesis uses hydrodynamic simulations to explore the properties of protoplanetary disks in the limit of weak turbulence and small particles. It characterizes the nature of the Kelvin-Helmholtz instability that is expected after the initial settling phase in disks containing small grains. These disks generate levels of turbulence consistent with observations. Values of the Shakura-Sunyaev turbulence parameter $\alpha$ are extracted directly from the simulations and are found to be approximately $\alpha = 2.7 \times 10^{-5}$. The implications of high and low values of $\alpha$ on planet formation are investigated, showing that planets can still form in disks with weak turbulence. We explore the associated constraints on planet formation and how they may affect the formation of planets at different radii within plausible planet forming disks.

# *Acknowledgements*

First and foremost, I would like to thank my supervisor Dr. James Wadsley for guiding my research over the last two years. I have learned a lot under his supervision and it has made me a better scientist, student, and colleague. I would also like to thank Dr. Joey Rucska for his invaluable personal and professional support. Regardless of how many questions I asked him, he was always happy to answer and went above and beyond in helping my transition to graduate school go smoothly. His research also laid the foundations upon which I could do my own work. Finally, I would like to thank myself for my perseverance. I couldn't have done it without me.

# Contents

# List of Figures

# Chapter 1

# Introduction

In the 300,000 years that modern humans have existed, we have transformed from a species of nomadic cave-dwellers with primitive tools into a global society that can communicate at the speed of light. Few of humanity's traits have remained constant in that time, but one of our most prevailing characteristics is our propensity for wonder when we look at the stars. It is therefore interesting to ask what drives this fascination; perhaps it speaks to some subconscious instinct for connection – both with each other and with the universe itself. Maybe the motivation is to be part of something bigger, or to make contact with the vastness beyond the horizon simply because it is out of reach. Or maybe our enamoration is, as Carl Sagan once said, a consequence of us being "a way for the cosmos to know itself."

Whatever the reason, we have a long history of trying to understand the cosmos. Archaeological discoveries going back as far as 32,000 years have showed evidence of people tracking, painting, and assigning stories to objects in the night sky (Rappenglück 2003). Since then, we have imaged more of the universe than we have of our own oceans. We've even stepped on the moon. However, our ability to study the heavens has always been limited because we are confined to our local celestial

neighbourhood. Some of our biggest questions have therefore been unknowable for so long: are there other worlds out there? What do they look like? Is there anyone on those worlds looking back and wondering the same things? It wasn't until 1879 that Agnes Mary Clerke took the first clear image of another planet in our solar system, and exoplanets were not even confirmed to exist until 1992. The good news is that, as humans entered the modern millennium, we brought with us an accelerating rate of technological advancement that finally helped us answer these questions.

The Kepler space telescope launched in 2009 and dramatically increased the number of known exoplanets. To date, there are over 5000 confirmed exoplanets and almost 3000 of them were confirmed by Kepler (Schneider et al. 2011; Akeson et al. 2013). The results of the mission highlighted the diversity in mass, size, composition, and orbital properties among planets as well as the limitless possibilities of how they could be arranged into solar systems (see Figure 1.1). The scale of Kepler's findings additionally provided the definitive conclusion that planetary systems are ubiquitous in the universe.

Our ability to observe and categorize so many new worlds was a major breakthrough in astronomy, but it only added fuel to another long-standing question: how did we get here? We now know that our solar system is not alone in the universe, but where did the Earth and all these other planets come from?

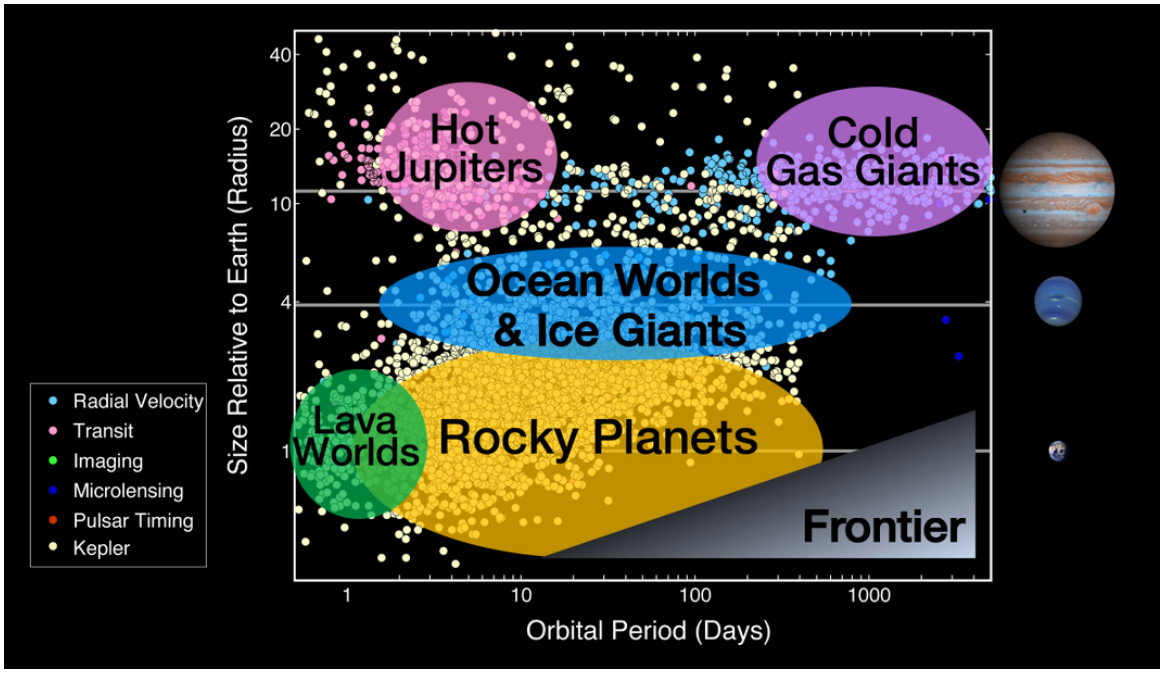


FIGURE 1.1: This image plots all the exoplanets confirmed by 2017 according to their sizes and orbital periods. Plot points are colour-coded to show the method of discovery, and a selection of planet types is highlighted. The Frontier represents the region of future research. NASA/Ames Research Center/Natalie Batalha/Wendy Stenzel.

The modern big picture of planet formation is based on the nebular hypothesis which can be traced back to Immanuel Kant's 1755 publication *Allgemeine Naturgeschichte und Theorie des Himmels* ("Universal Natural History and Theory of the Heavens"). He posits that solar systems are formed from a cloud (or "nebula") of gas and dust that orbits a central star. We know that this cloud collapses into a disk that differentiates into planets over time (Armitage 2020); in this section we provide an overview of the nature of these disks and summarize how the tiny dust grains inside them grow into massive planets.

While the nebular hypothesis provides a foundation for our understanding of planet formation, there are still many unanswered questions about the details of this process. For example, what conditions are required in the disk to form planets? Are there any barriers to growth, and if so how do we resolve them? These are some of the questions that will be explored in this thesis.

## 1.1 Protoplanetary Disks

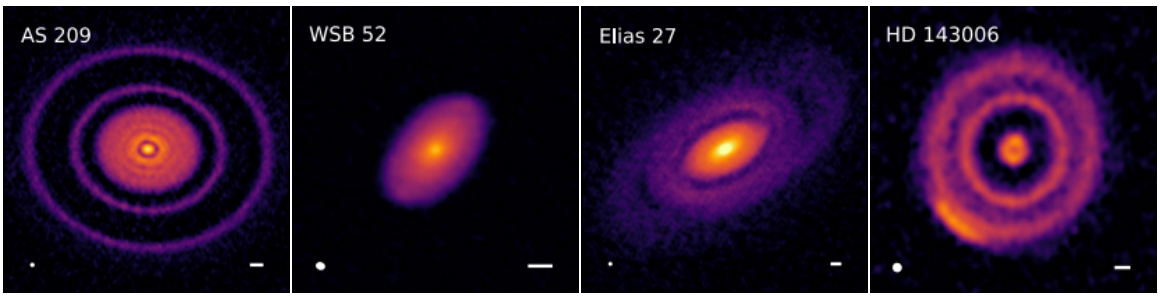


FIGURE 1.2: These high resolution images of nearby protoplanetary disks taken by ALMA illustrate the large variations in their shape and size. The scale bar in the bottom right of each image denotes 10 AU. ALMA (ESO/NAOJ/NRAO), S. Andrews et al. (2018).

The wide diversity in planetary systems reflects, in part, the physical conditions of the disks inside which the planets are formed. These disks are dense concentrations of gas

and dust rotating around young stars. The cool dust in these disks is ideally observed with infrared (IR) wavelengths or longer, and the molecules within the disks are also best visible in the mm/sub-mm. The Atacama Large Millimeter Array (ALMA) has been providing high resolution images of these disks since 2014, revealing that they are very often interspersed with rings. These gaps are observed in the dust continuum at a variety of orbital radii (Andrews et al. 2018), and it is thought that they are caused by giant planets clearing a path in their orbit around a young star (Andrews et al. 2016; Pinte et al. 2020).

Light from Young Stellar Objects (YSOs) interacts with dust in the disk, leading to re-emission of the energy at longer wavelengths. We therefore expect to see a near-infrared excess around these young stars when compared to their older counterparts. YSOs are classified as Class 0, Class I, Flat Spectrum, Class II, or Class III. Each subsequent classification is a later evolutionary stage, such that Class 0 stars are deeply embedded with the highest IR excess (seen as a blackbody spectrum of optically thick gas) and Class III stars have very wispy disks with weak IR excess. We see less of an IR excess in YSOs than we expect to: most disks correspond to Class II, which means that the dust in disks is disappearing at a fast rate (Armitage 2020). Estimates based on the missing IR excess suggest that disk lifetimes do not typically exceed 10 million years (Mamajek 2009). The collapse of both magnetic and non-magnetic molecular cores has been modelled numerically, and these simulations also support the idea that disks form within $\sim 10^4$ years (Yorke et al. 1993; Hueso and Guillot 2005). Important phases of planet formation have timescales that are estimated to be shorter than the lifetime of the Class 0 and Class I phases of YSO evolution, which goes to show that planet formation must be well underway in protoplanetary disks much earlier than previously assumed – even before the central star becomes optically

visible (Armitage 2020). While we have come a long way from painting constellations in caves, there is still a lot about the universe that we don't understand.

Since the release of those images by ALMA, there has been a resurgence of interest in the study of planet formation and the nature of protoplanetary disks. These disks are extremely complex, and are home to many different dynamical processes that are intricately connected by their interactions with one another. Additionally, many of these processes occur over thousands of years and cannot be observed in real-time. Therefore, an effective way to study protoplanetary disks is through the use of computer simulations.

### 1.1.1 Formation and Evolution of Disks

Molecular clouds are large structures of gas and dust that can be $10 - 100$ parsecs across. Within them are regions of higher density called cores from which stars and disks are formed. These cores have masses of order $\sim 1M_{\odot}$ and span a region of about 0.1 pc, inside which the number densities exceed $10^4$ cm$^{-3}$ particles per cubic centimeter (Myers 1985). When the core reaches some critical density, it begins to collapse under the influence of its own gravity. Most of the mass collects in the central region, causing it to heat up faster than the surrounding material and eventually form a protostar. The rest of the gas and dust forms a cloud that rapidly flattens as it collapses in order to conserve its angular momentum. This is how protoplanetary disks (sometimes called circumstellar disks) are formed (Nakamoto and Nakagawa 1994; Montmerle et al. 2006).

Typical sizes of protoplanetary disks are in the 100s of AU. As the disk evolves, angular momentum is transported to larger radii by turbulent viscosity (Section 1.1.4) and

the disk expands. Disk winds can remove excess angular momentum and prevent this expansion if they are present (Lynden-Bell and Pringle 1974; Hartmann et al. 1998). In young disks, the gas and dust extend out to a similar radius, but radial drift (Section 1.1.3) causes the size of the dust disk to shrink over time. Eventually, the gas disk will extend beyond the limits of the dust disk. (Ansdell et al. 2018).

By examining the amount of material required to create the planets, the minimum-mass solar nebula (MMSN) model (Weidenschilling 1977b; Hayashi 1981) provides a lower limit on the mass of the young disk around our Sun. Estimates of the MMSN place this limit at $0.01 M_\odot$ for our solar system (Armitage 2020). This is consistent with star formation simulations, which give expected disk masses of $1\% - 8\%$ the mass of the central star $M_*$ (Bate 2018). The MMSN is also comparable to the smallest observational estimates of protoplanetary disk masses around other stars (Ansdell et al. 2016). Some of the disk's initial mass will be lost over time as it drifts and accretes onto the star (Bitsch et al. 2015). Another possible source of mass depletion is photoevaporation (Armitage 2020).

### 1.1.2 Disk Structure

Protoplanetary disks are geometrically thin. If we balance the vertical component of stellar gravity acting on the disk with the vertical pressure gradient in the gas, the thickness of the disk can be described by the gas scale height $H_g$. In a typical disk we have $H_g/r \ll 1$ at a radial distance $r$ from the star (Armitage 2020).

$$H_g = \frac{c_s}{\Omega} \tag{1.1}$$

Here, $c_s$ is the isothermal sound speed and $\Omega$ is the Keplerian angular velocity:

$$c_s^2 = \frac{k_B T}{\mu m_p} \tag{1.2}$$

$$\Omega^2 = \frac{GM_*}{r^3} \tag{1.3}$$

The mass of a proton is $m_p$ and the mean molecular weight $\mu = 2.3$ for molecular gas. $k_B$ is the Boltzmann constant and $T$ is the temperature of the disk (Armitage 2020).

It is commonly assumed that the disk is vertically isothermal, and that its temperature depends only on its radial distance from the star. These are reasonable assumptions if the temperature of the gas is set by stellar irradiation. For flared disks, the temperature profile can be described as in Armitage (2020) where $L_*$ is the luminosity of the star and $\sigma_{sb}$ is the Stefan-Boltzmann constant:

$$T_{\text{disk}} = \left(\frac{L_*}{4\pi\sigma_{sb}}\right)^{1/4} \alpha^{1/4} r^{-1/2} \tag{1.4}$$

If the disk can absorb radiation from the star up to a height $h_p(r)$ above the mid-plane, then the disk is flared if $h_p/r$ increases with the orbital radius $r$:

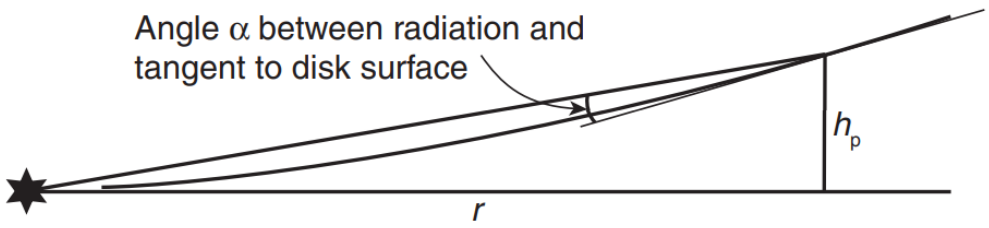


FIGURE 1.3: Schematic showing the structure of a flared disk (Armitage 2020).

A typical value for the irradiation angle is $\alpha = 0.05$ (Dullemond and Dominik 2005). This $\alpha$ is not related to the Shakura-Sunyaev turbulence parameter introduced in Section 1.1.4.

Rotating disks are supported against gravitational collapse by thermal pressure and centrifugal force. We can use the surface density of the gas disk $\Sigma_g$ to define a parameter that quantifies this stability (Toomre 1964):

$$Q \equiv \frac{c_s \kappa}{\pi G \Sigma_g} \tag{1.5}$$

Here, $G$ is the gravitational constant and $\kappa$ is the disk's epicyclic frequency. In a Keplerian disk, $\kappa = \Omega$. A disk is stable against strong instabilities (such as spiral modes) if $Q \gtrsim 3$. Most planet formation occurs within the inner 50 AU, and disks are stable in this region. Therefore, gravitational instabilities are not expected to play a significant role in the formation of most planets in any direct way.

As briefly discussed in Section 1.1, interspersed gaps in the dust continuum of protoplanetary disks are one of their most commonly observed large-scale structures. However, small particles like dust typically only make up about 1% of the total disk mass (Armitage 2020); the vast majority of the disk is dominated by gas while the dust settles into a thin layer along the mid-plane.

The surface density of the gas is commonly assumed to be a power law $\sim \Sigma_g \propto r^{-1}$ (Lynden-Bell and Pringle 1974; Andrews et al. 2009) and the dust surface density is initially $\Sigma_d = Z \times \Sigma_g$ (Drążkowska et al. 2021), where $Z$ is the dust-to-gas ratio. In the interstellar medium, $Z \sim 0.01$ (Bohlin et al. 1978), but observations of protoplanetary disks have suggested that $Z$ can be as large as 0.1 within them as a result of radial drift concentrating the dust (Long et al. 2017; Kama et al. 2020). Section 1.1.3 includes a

detailed description of radial drift.

It is important to note that the dust-to-gas ratio $Z$ differs from metallicity, which is usually defined as the mass of all material heavier than helium ("metals") divided by the total gas mass. This difference is due to the fact that dust is a mixture of solid compounds that can include both metals and hydrogen. One notable example is ice: solid water-ice is a significant component of our solar system beyond the ice line. Sometimes called the snow line or frost line, this is the radial point in the disk $r_{\rm ice}$ where temperatures are low enough for water to freeze into grains of solid ice. The result is a sharp increase in $Z$ (and consequently the initial surface density of solids) by a factor of $\sim 4$ at $r \geq r_{\rm ice}$ for a disk with solar-like composition (Hayashi 1981). In a disk that has a region dominated by turbulence, the ice line is slowly displaced inward due to changes in opacity resulting from grain growth and disk accretion. The position of the ice line remains fixed over time for a strictly radiative disk with no other source of heating (Jewitt et al. 2007; Hasegawa and Pudritz 2011). There exist different ice lines to describe the radial distances at which other volatile compounds like $CO_2$ and methane can solidify, but the ubiquity of water makes $r_{\rm ice}$ the most important one from a planet formation perspective (see Section 4.3).

### 1.1.3 Interactions Between Dust and Gas

As noted earlier, dust and gas can separate radially. This is due to drag. Particles that are smaller than the mean-free-path of gas molecules in the disk will feel Epstein drag (Epstein 1924; Weidenschilling 1977a). In this regime, spherical particles of radius $s$ traveling with velocity $\mathbf{v}$ relative to the surrounding gas experience a drag force $\mathbf{F}_D$.

For a particle travelling at a speed $v$ that is much slower than the mean thermal speed of the gas $v_{\rm th} = \sqrt{8/\pi}c_s$, this drag force is (Armitage 2020):

$$\mathbf{F}_D = -\frac{4\pi}{3}\rho_g s^2 v_{\rm th}\mathbf{v} \tag{1.6}$$

Here, $\rho_g$ is the volumetric gas mass density. We can describe the timescale required for Epstein drag to significantly modify the velocity of the particle by defining a characteristic stopping time:

$$t_{\rm stop} = \frac{mv}{|\mathbf{F}_D|} = \frac{\rho_m s}{\rho_g v_{\rm th}} \tag{1.7}$$

The Stokes number $\tau_s$ is then derived by comparing this stopping time to the orbital period $T_{\rm orb} = 2\pi\Omega^{-1}$

$$\tau_s = t_{\rm stop}\Omega \tag{1.8}$$

where $\rho_m$ is the internal density of the dust particle (it is also sometimes called the material density or specific weight). Note that $\rho_m$ is a property of an individual dust particle and should not be confused with $\rho_d$ which is derived from the total mass of all dust particles in a volume of space. Most small particles in the disk (excluding the innermost regions close to the star) experience Epstein drag (Birnstiel et al. 2016).

Since gas density and temperature decrease away from the star, a radially outward pressure gradient is created; as a result, the gas in a disk will orbit at slightly sub-Keplerian speeds. Dust particles are not affected by this pressure gradient and attempt to travel at Keplerian velocities. This means that dust grains feel a headwind during their orbit which causes them to lose angular momentum and spiral toward the star in a process called *radial drift*. The velocity of radial drift depends on the size of the dust grains, which is proportional to the Stokes number (Figure 1.4).

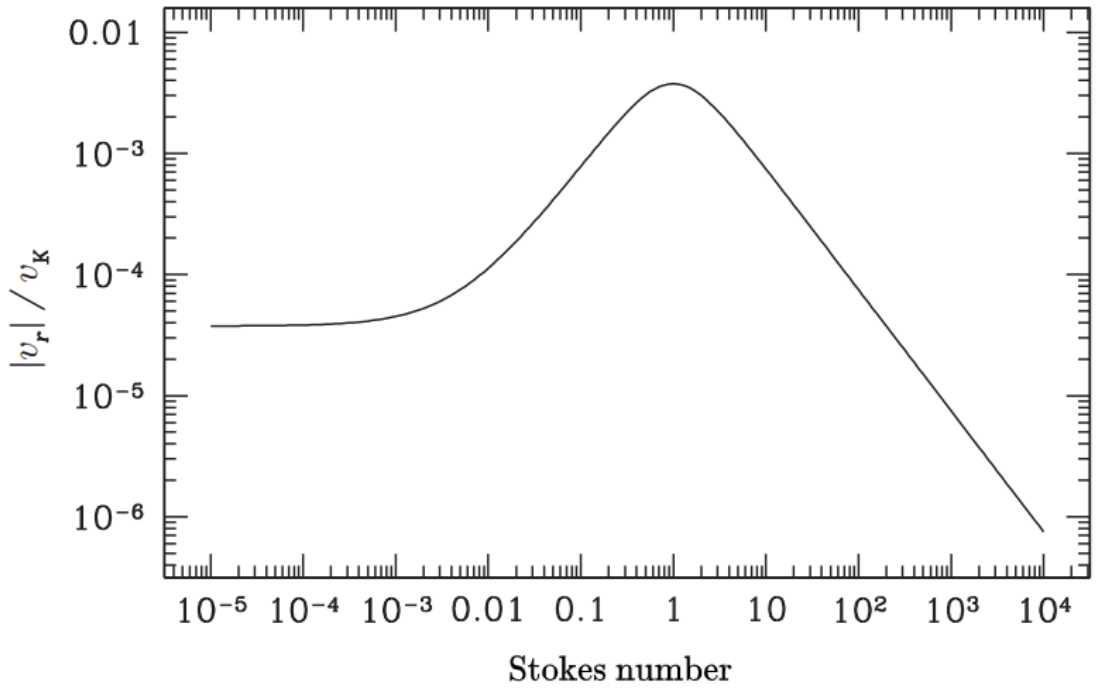


FIGURE 1.4: The radial drift velocity of particles at the disk mid-plane as a function of the Stokes number (Armitage 2020). $v_k = \sqrt{GM_*/r}$ is the local Keplerian velocity

Small grains are very well coupled to the gas, and large grains (planetesimals) travel on Keplerian orbits without significant drifting. Radial drift is highest in-between these two extremes, at a Stokes number of unity: at 1 AU, this corresponds to a particle around one-meter in size. Once the disk has formed, radial drift occurs on a timescale of $10^3$ years or less; this is much shorter than the lifetime of the disk, which implies that planetesimal formation must be very rapid (Armitage 2020).

### 1.1.4 Nature of Disk Turbulence

The gas in a protoplanetary disk experiences turbulent flow, which transports the gas and dust in eddies. This movement may facilitate collisions and sticking between dust particles, allowing them to grow (Brauer et al. 2008; Birnstiel et al. 2010; Drążkowska

et al. 2013). However, dust grain growth may also be slowed if turbulence is too strong (Cuzzi et al. 1993; Okuzumi and Ormel 2013; Gole et al. 2020). For these reasons, the characterization of turbulence in protoplanetary disks is crucial to our understanding of planet formation.

Turbulent flow is characterized by a high Reynolds number (Re), which is the ratio of inertial and viscous forces within a fluid:

$$\mathrm{Re} \equiv \frac{uL}{\nu_m} = \frac{u^4}{\epsilon \nu_m} \tag{1.9}$$

In protoplanetary disks, $u = c_s$ is the flow speed, $L = H_g$ is the characteristic length determined by convention, $\nu_m \sim D c_s$ is the molecular (or kinematic) viscosity of the gas with units [Length]$^2$ [Time]$^{-1}$ and $D$ is the mean-free-path of the gas. The probable onset of turbulence is expected for $\mathrm{Re} > 5 \times 10^5$ (Incropera et al. 1996).

Typical estimates of the Reynolds number in protoplanetary disks are very high, of order $\mathrm{Re} = 10^8 - 10^{11}$ (Cuzzi et al. 2001). Measurements of molecular line widths in interferometric data also tell us that the turbulence in protoplanetary disks is subsonic with Mach numbers $\ll 1$ (Guilloteau et al. 2012), which means that the flow is essentially incompressible (Almgren et al. 2006). Any supersonic turbulence would result in shocks that will quickly dissipate and force the turbulence back into the subsonic regime (Armitage 2020).

Large eddies in a turbulent fluid are unstable and break up into smaller eddies. This causes kinetic energy to be transferred to smaller and smaller scales until the eddies become so small that their energy is dissipated by $\nu_m$ into heat and they disappear

(Richardson 1922; Pope 2000) [1]. We can therefore characterize the flow with a mean rate of energy dissipation $\epsilon$ which has units [Length]$^2$ [Time]$^{-3}$.

Combining $\epsilon$ with $\nu_m$ gives the length scale at which viscous dissipation occurs:

$$l_K = \left(\frac{\nu_m^3}{\epsilon}\right)^{1/4} \tag{1.10}$$

$l_K$ is called the Kolmogorov scale, and it describes the size of the smallest eddies in the fluid (Kolmogorov 1941). If we take $\Lambda$ to be an upper limit on the size of eddies, we can define an *inertial range* spanning $\Lambda^{-1} \ll k \ll l_K^{-1}$ in which there is negligible dissipation and the dominant process is the transfer of kinetic energy from large eddies to small eddies by inertial effects. Here, $k$ is the wavenumber. Kolmogorov hypothesized that when Re was high, the energy entering the inertial range was in equilibrium with the amount of energy exiting it; therefore, the energy spectrum $E(k)$ in this regime depends only on $\epsilon$. From dimensional arguments, Kolmogorov surmised that $E(k) \propto \epsilon^{2/3} k^{-5/3}$ in the inertial subrange (Kolmogorov 1941; Pope 2000).

Since the turbulence in protoplanetary disks is subsonic and characterized by a large Re, it can be described by Kolmogorov's theory and its energy spectra should follow the power law $E(k) \propto k^{-5/3}$ in the inertial range. Völk et al. (1980) and Markiewicz et al. (1991) developed a formalism for describing grain collision velocities in Kolmogorov turbulence that was later solved analytically by Ormel and Cuzzi (2007). These models are frequently used in dust coagulation codes (e.g., Dullemond and Dominik 2005; Okuzumi et al. 2012) and hold up well when tested against numerical simulations

[1] The turbulent energy cascade was described in a poem by Lewis Fry Richardson as "big whorls have little whorls which feed on their velocity, and little whorls have lesser whorls and so on to viscosity" (Richardson 1922).

(Pan and Padoan 2015; Sakurai et al. 2021). Recent studies have suggested non-Kolmogorov turbulence is possible in the presence of magnetic fields (Gong et al. 2021), but the $k^{-5/3}$ profile is expected whenever the Mach number is low.

Consider a protoplanetary disk in local thermodynamic equilibrium that can efficiently radiate away viscous heat to become geometrically thin. We take the gas scale height as the maximum size of an eddy: $\Lambda = H_g$. Under the same assumptions of strong subsonic turbulence as before, we can do another dimensional analysis to describe the *turbulent viscosity* of this disk as $\nu_t = \alpha c_s H_g$. Note that $\nu_m \neq \nu_t$. The non-dimensional factor $\alpha < 1$ was first proposed by Shakura and Sunyaev (1973); it stores information regarding the efficiency of angular momentum transport from turbulence, and it is treated as a constant (although it might actually vary with temperature, composition, or density of the disk). A larger $\alpha$ means stronger turbulence (Armitage 2020).

The study of the origins, nature, and strength of $\alpha$ is still an active area of research. One popular hypothesis for the source of protoplanetary disk turbulence is the magnetorotational instability (MRI): temperatures in the disk interior where $r < 0.1$ AU can exceed 1000 K, causing the gas in this region to ionize and create a magnetic field. For a disk that is rotating with angular velocity $\Omega \propto r^{-3/2}$, this magnetic field is destabilizing (Balbus and Hawley 1991). Simon et al. (2012) estimate that turbulence caused by the MRI has a strength $\alpha \sim 0.01$ in the inner disk. This value of $\alpha$ is consistent with observed rates of disk accretion very close to the star (Hartmann et al. 1998).

However, ionization of the gaseous mid-plane is thought to be weak further away from the star (Turner and Drake 2009). For $r > 0.1$ AU, interactions between the magnetic field and the gas happen indirectly via non-ideal magnetohydrodynamics (MHD).

Some simulations of the turbulence in this region have estimated that $\alpha \sim 0.001 - 0.1$ (Simon et al. 2013; Simon et al. 2015). Others predict that the MRI does not work at all for non-ideal MHD, giving essentially no $\alpha$ (Bai and Stone 2013). Although simulations have not yet conclusively proven that the MRI cannot work in this region, observational constraints favour that conclusion. For example, Cleeves et al. (2015) suggest that $\alpha$ is much lower than 0.001 in this "dead zone" that can extend to $50-65$ AU in the disk around the K6 T-Tauri star TW Hydrae, which has a mass of $0.8M_{\odot}$ and luminosity $0.28L_{\odot}$. In more luminous stars, the inner edge of this dead zone is pushed to larger radii. The location of the outer edge of the dead zone depends on the amount of X-rays and cosmic rays present.

In all cases, the dead zone will coincide with the region where most planet formation occurs. There must be another source of turbulence in this part of the disk. Some examples of alternative sources of turbulence are the vertical shear instability, convective overstability, and the zombie vortex instability. See Lyra and Umurhan (2019) for an overview of these alternatives. Importantly, there may still be regions of the disk beyond the dead-zone that do experience MRI turbulence. This is also true for heights far above the mid-plane (Turner and Drake 2009).

The dusty mid-plane of a protoplanetary disk orbits at Keplerian speeds, while the gas above and below travels at slightly sub-Keplerian velocities due to impedence from a radial pressure gradient (see Section 1.1.3). The discrepancy between the speeds of the two layers results in a velocity gradient which leads to a vertical shear that can become unstable and generate a Kelvin-Helmholtz instability (KHI). The KHI is the most general form of the vertical shear instability, and it is a popular alternate hypothesis for the origin of turbulence in protoplanetary disks (Goldreich and Ward 1973; Cuzzi et al. 1993). A comparison between the characteristics of disk turbulence

and the properties of Kelvin-Helmholtz instabilities could help us understand if this is the case.

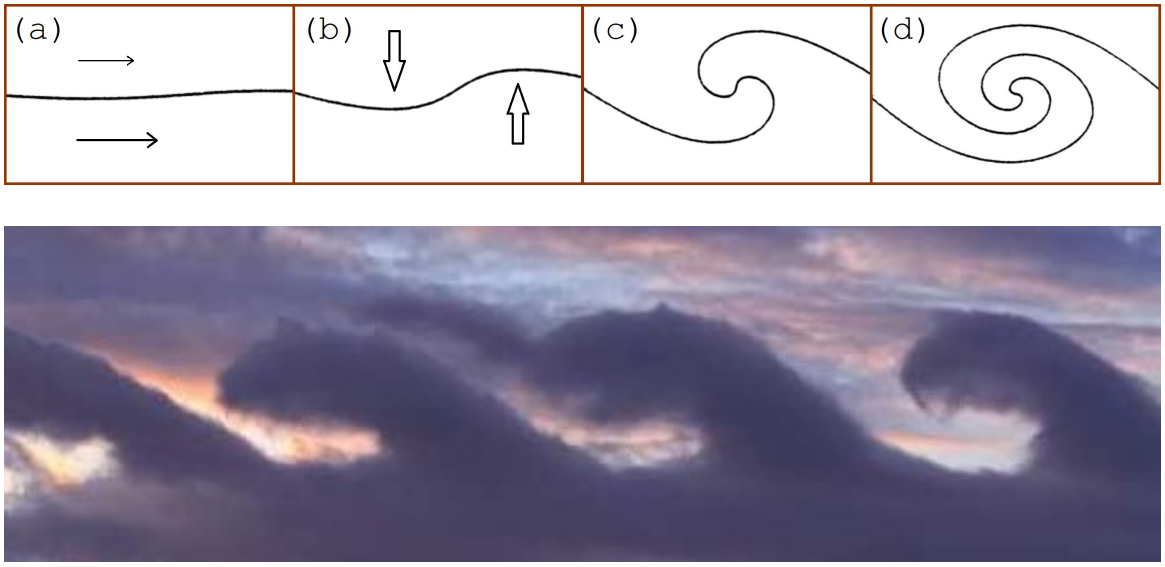


FIGURE 1.5: Two fluids moving at different speeds (a) create a vertical shear (b) that can grow to a point of non-linear instability (c, d). Kelvin-Helmholtz instabilities are commonly seen in cloud formations on Earth. Photograph modified from The International Cloud Atlas/June Grønseth.

It is important to note that the KHI only applies for an infinitely thin shear layer. For a finitely thin fluid layer, we can instead use the Richardson number to describe its stability:

$$\mathrm{Ri} \;=\; -\frac{g}{\rho}\frac{\partial\rho/\partial z}{(\partial u/\partial z)^2} \tag{1.11}$$

In this equation, $g$ is the magnitude of vertical gravity, $\rho$ is the density of the fluid, $u$ is its flow speed, and $z$ is the height at the point of interest. Classically, $\mathrm{Ri} > 0.25$ indicates stability (Chandrasekhar 1961) but we will revisit this limit in Chapter 3. In a protoplanetary disk, $g \sim \Omega^2 H_d$ is dominated by the vertical component of the

star's gravity, and $\rho = \rho_g + \rho_d$ is the total density. The dust scale height $H_d$ is much smaller than the gas scale height $H_g$ as a result of dust settling to the mid-plane.

Observational evidence has produced estimates on the upper limit of $\alpha \sim 10^{-2} - 10^{-3}$ in protoplanetary disks via measurements of line widths or the study of disk evolution (Hartmann et al. 1998; Flaherty et al. 2015; Teague et al. 2016). However, methods based on disk evolution are unable to constrain $\alpha$ if there are disk winds, so these estimates are probably not relevant. Additionally, an upper limit is insufficient in describing the exact nature of turbulence in disks. Research has shown that there are multiple ranges of $\alpha$ within this limit that have very different effects on planet formation (Gole et al. 2020). It is therefore important to provide more precise estimates of $\alpha$ in a typical disk.

## 1.2 Stages of Planet Formation

The mechanisms which allow solid particles in a disk to grow from $\mu$m to planet sizes are dependant on their size; in other words, different sized solid objects are subject to different methods of growth. At small sizes, the behaviour of dust grains is dictated by aerodynamic forces and interactions with the gas that allow the grains to be stirred up and stick together. Gravitational interactions become important when the objects grow to $\sim 1-100$ km in size, at which point they are called planetesimals. Subsequent evolution of planetesimals is governed by their gravitational interactions and collisions with each other and with the dust and gas in their orbits. A planetary embryo is only considered a planet once it has grown large enough for its self-gravity to shape it into a spherical object and it has cleared out the majority of dust and gas in its path around the central star. In this section, we will give details of the processes that are

involved in each stage of planet formation.

### 1.2.1 Settling

Planet formation begins from an initial pool of micron-sized rocky or icy dust in the disk. The smallest dust grains grow by colliding and coagulating with other dust grains nearby as they settle toward the disk mid-plane. Turbulent mixing can also help the grains grow at this stage, until they become loose cm-size aggregates.

Collisions between dust particles do not always result in their net growth. The outcome of a collision between two dust grains depends on the impact velocity, the size of the grains, their composition, and other properties (Blum and Wurm 2008; Windmark et al. 2012).

Figure 1.7 shows the parameter space for the following possible outcomes of collisions between two dust grains (Birnstiel et al. 2016):

- **sticking**: particles stick together, resulting in growth without either of the particles fragmenting in the process
- **bouncing**: particles bounce off one another and neither changes its mass; it is possible for either particle to become more compacted
- **erosion**: the smaller particle glances off the larger one, from which it shaves off some material; the smaller particle may also shatter
- **mass transfer**: the smaller particle fragments during collision and deposits some of its mass onto the larger target

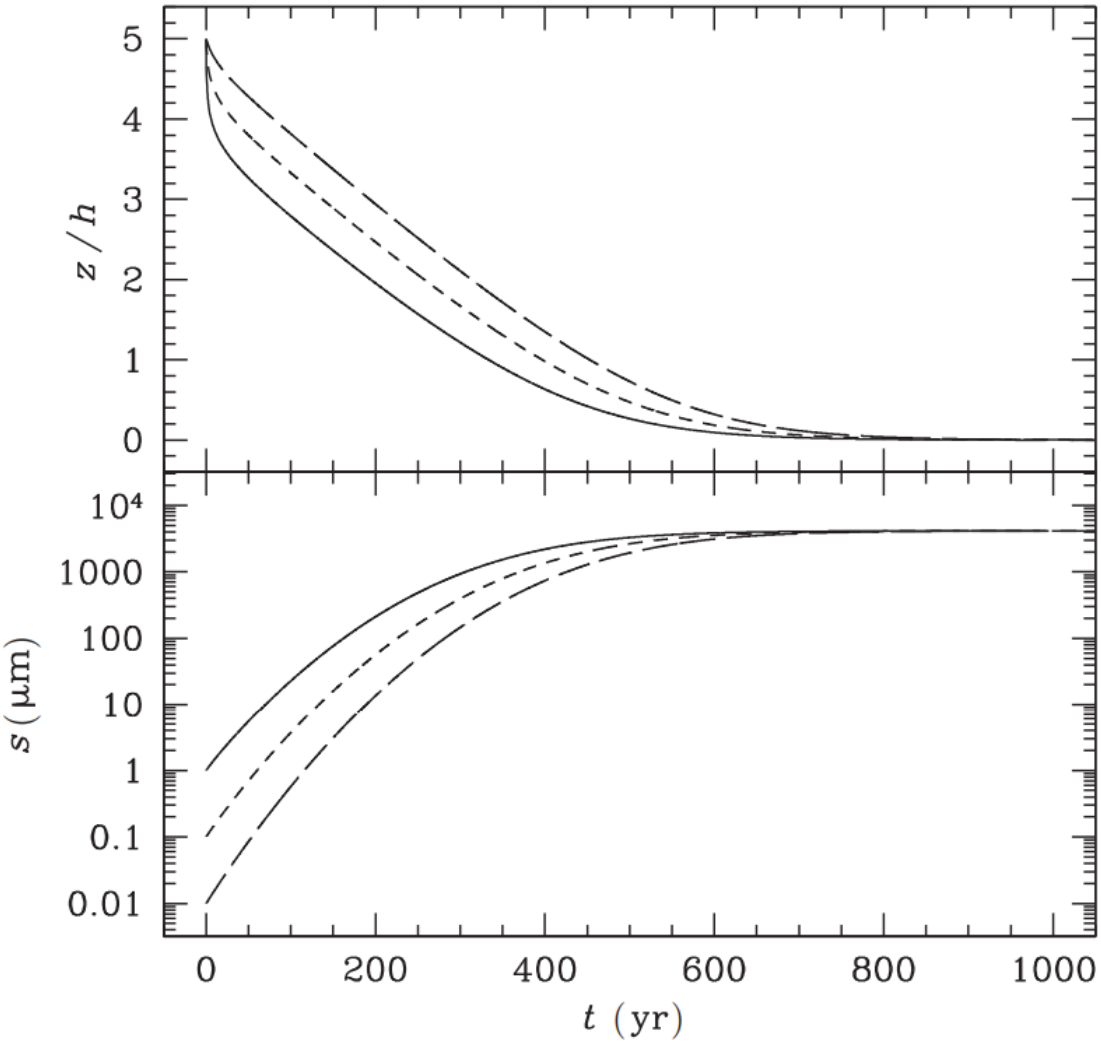


FIGURE 1.6: The bottom panel shows the growth of a single particle at 1 AU during the settling stage for different starting sizes ($s$ is its radius). The upper panel shows the particle's height above the mid-plane. The scale height is $h = 3 \times 10^{11}$ cm in this example (Armitage 2020).

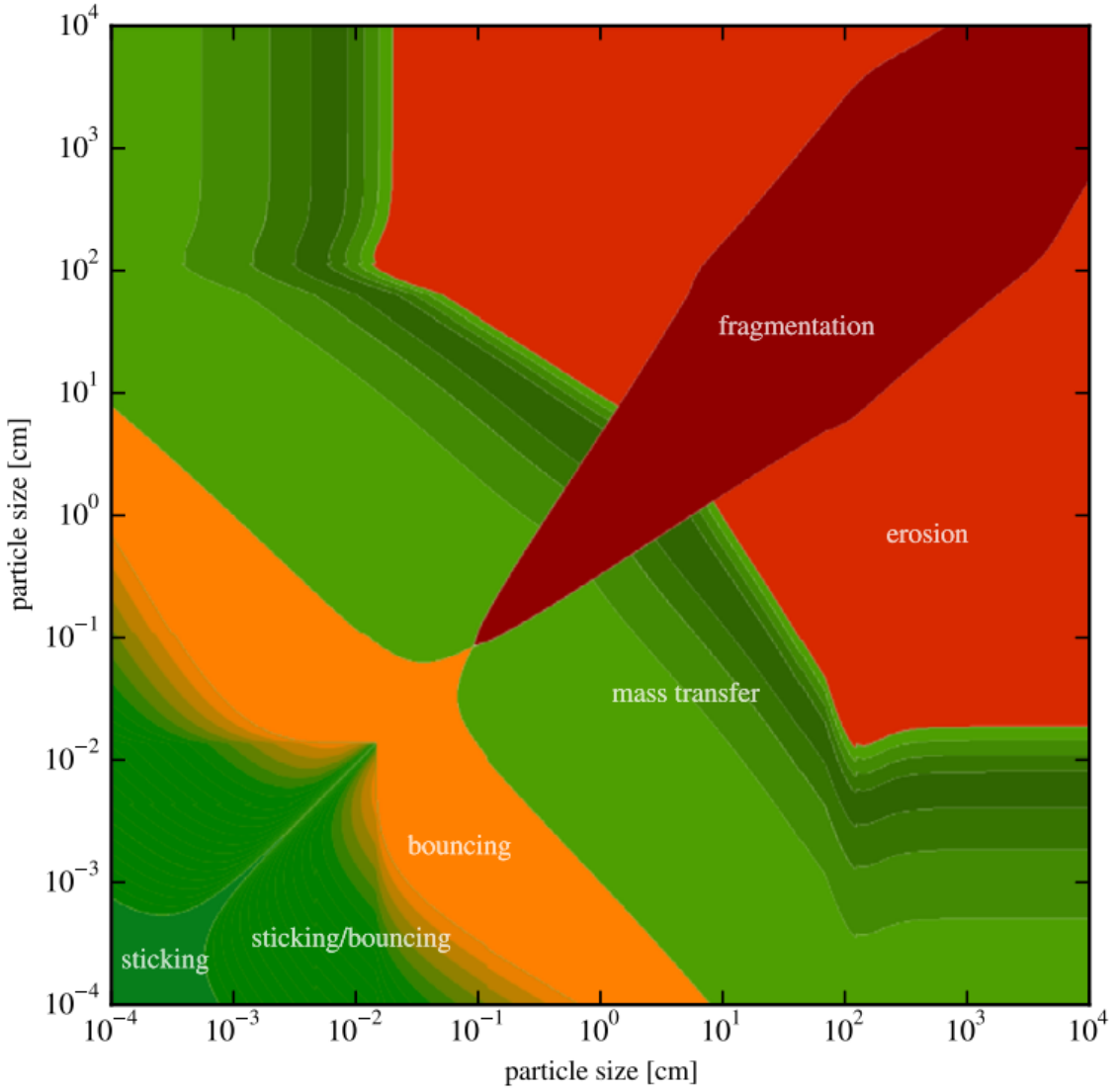


FIGURE 1.7: The mean outcome of collisions between silicate grains. In green regions, there is net-growth of the larger particle. Similarly, red regions indicate a net loss of mass and orange regions denote mass-neutral outcomes. The axes refer to a speherical particle's radius. Reproduced with permission from Birnstiel et al. (2016).

- **fragmentation**: one or more of the particles is completely destroyed and no mass is transferred

### 1.2.2 Growth Barriers

As seen in Figure 1.4, radial drift velocities are greatest for objects with $\tau_s = 1$. This corresponds to meter-sizes at 1 AU. Weidenschilling (1977a) concludes that meter-sized objects located at this radius will fall into the star within 100 years, and those at 10 AU will disappear within 1000 years. This marks a prospective upper limit on the timescale of planetesimal formation called the *radial drift barrier*.

To overcome the radial drift barrier, grains must grow to planetesimal sizes within 100 years at 1 AU. Alternatively, they could avoid drifting if there exists a local pressure maximum caused by strong turbulence (Whipple 1972). The plausibility of such maxima and their potential role in planetesimal formation is an active area of research.

Grains at this size also tend to fragment upon collision with one another (see Figure 1.7). This is called the *fragmentation barrier*. The fragmentation and radial drift barriers together define the "meter-size barrier" in planetesimal formation where growth beyond one meter at 1 AU cannot be achieved through coagulation (sticking) alone.

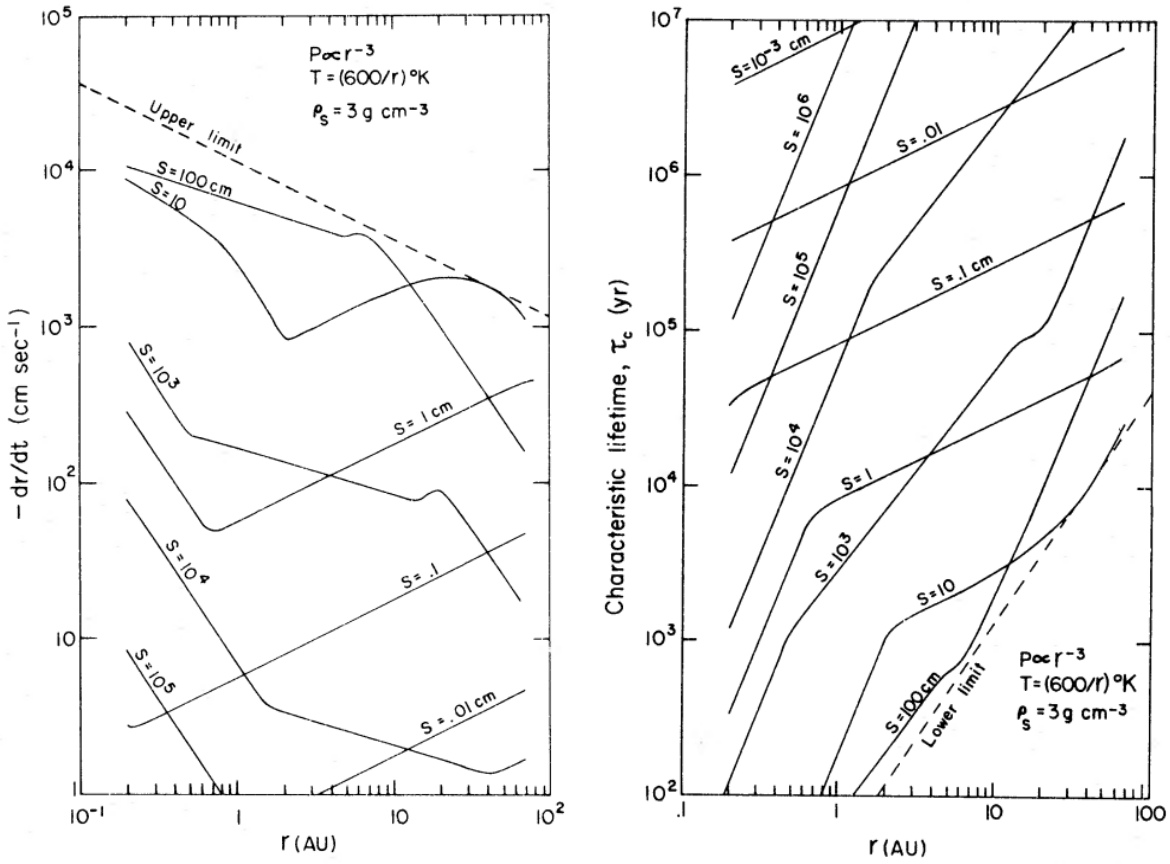


FIGURE 1.8: The plot on the left shows radial drift velocities for particles at different orbital radii. The plot on the right shows the timescales within which particles fall into the star. The horizontal axis indicates the particle's initial orbital radius. In each case, $s$ is the radius of a spherical particle. Figures 5 and 6 in Weidenschilling (1977a). Reprinted by permission of Oxford University Press on behalf of the Royal Astronomical Society.

### 1.2.3 Streaming Instability

If we assume the gas in a disk is incompressible and treat the dust as a pressure-less fluid, we can model the interactions between the dust and gas using coupled continuity and momentum equations. Subsequently solving these equations for a steady state gives the Nakagawa–Sekiya–Hayashi (NSH) equilibrium (Nakagawa et al. 1986). The vertical component of gravity from the central star and any self-gravity within the

gas and dust fluids is neglected in this model.

Youdin and Goodman (2005) were first to study the stability of the NSH equilibrium by introducing small perturbations to the dust velocity in regions of the disk that contained an initial overdensity of cm-sized solids. In these regions, momentum is transferred from the drifting dust to the surrounding gas which causes the gas to be accelerated toward Keplerian speeds. As a result, the dust particles in these regions feel a reduced headwind from the gas, and radial drift of the dust slows. This causes a pile-up of mm/cm-sized dust particles which organize into filaments and collapse into clumps within a few local orbital periods. If these clumps exceed the Roche density (when self-gravity overcomes tidal forces from the star), they will quickly condense into planetesimals $\sim$ 100 km in size. This mechanism of collapse in overdense dust filaments is called the *streaming instability* (SI) and it is the leading proposal for overcoming the meter-size barrier in planet formation.

In the original framework by Youdin and Goodman (2005), the perturbations were linear and two-dimensional. They found that as long as the relative equilibrium velocity between the particles and gas was non-zero, the disk was unstable for a large range of $\tau_s$, dust-to-gas mass volume ratio $\mu = \rho_d/\rho_g$, and perturbation wavelengths. $\tau_s$ closer to 1 sped up the growth rate, as did choosing a $\mu$ near unity. However, only a small subset of parameter choices would allow growth to occur within a hundred orbits. The growth rates for the fastest growing mode in their system is plotted as a function of the perturbation wavenumber $k$ in the top panel of Figure 1.9. The bottom panel shows a similar plot for the fastest growing mode in a system which includes a steady vertical velocity for the dust in order to represent the settling of particles to the mid-plane (Chiang and Youdin 2010; Squire and Hopkins 2018).

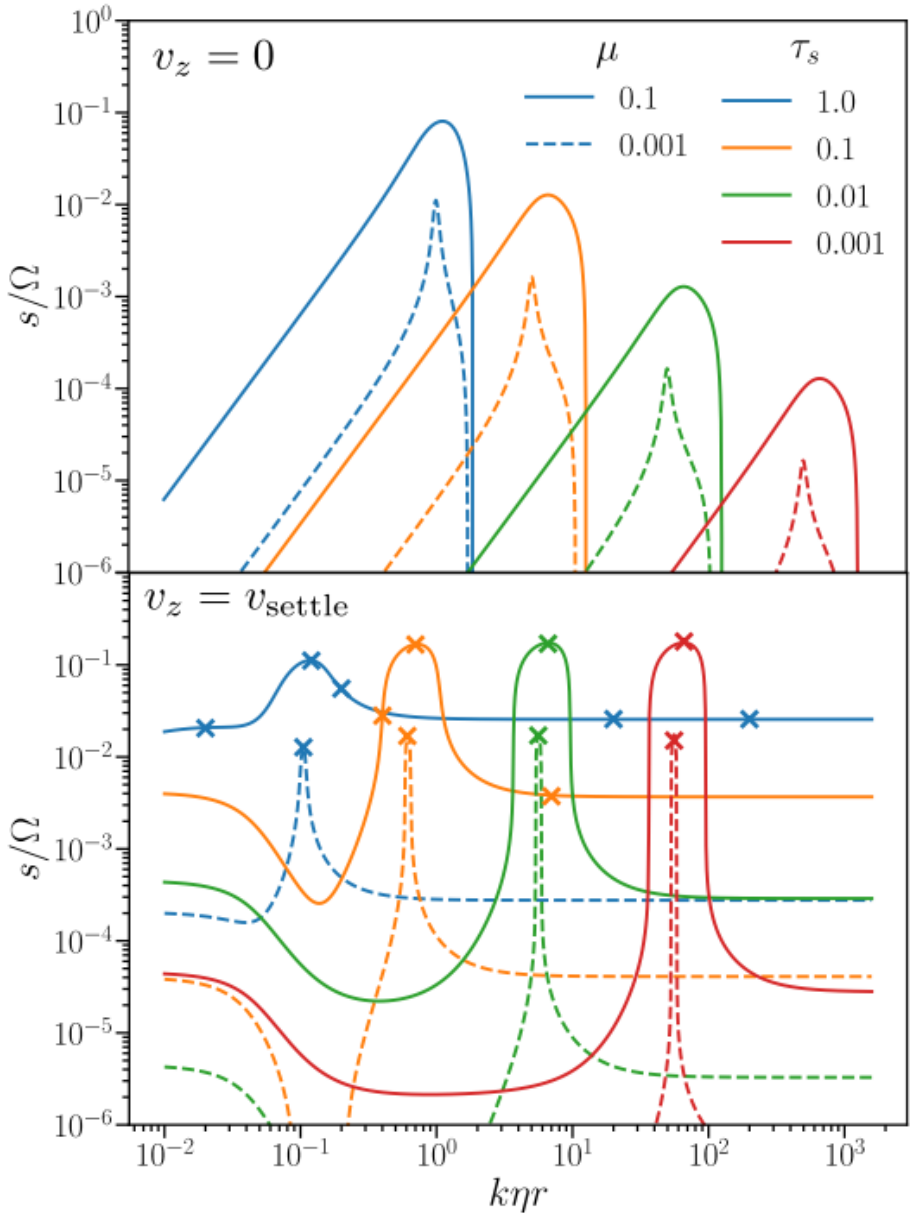


Figure 1.9: *Top:* Growth rates of the fastest growing mode in a linear streaming instability normalized by $\Omega \propto T_{\rm orb}^{-1}$ as a function of $k\eta r$, which characterizes the dynamics of the disk. The strength of the pressure gradient on the gas is described by $\eta$ (see Section 2.3), and $k$ is the wavenumber. *Bottom:* As above, but with the inclusion of a steady vertical settling velocity on the dust. Reproduced with permission from Rucska (2022).

Johansen et al. (2007) were able to expand on previous work by exploring non-linear evolutions of this instability in 3D simulations of a disk with an initial dust-to-gas mass ratio of 1%. Although the distribution of the dust was roughly uniform initially, they found that the SI was capable of concentrating grains into regions where the dust mass densities could be over 50 times larger than the surrounding density of the gas. The disk enters a state of turbulent saturation within a few orbital times and the maximum dust density stops growing. At this point in the disk's evolution, Johansen et al. (2007) introduce particle self-gravity into their simulations which causes the overdense regions of dust to collapse into multiple bound clumps. One of these clumps had a mass similar to that of Ceres.

Later simulations by Bai and Stone (2010a) also studied non-linear evolution of the SI but from a different perspective; instead of exploring the effects of self-gravity, they allowed multiple particle sizes within the range $\tau_s = [10^{-4}, 10^{-1}]$ to coexist in the disk. This contrasts the model in Johansen et al. (2007) where the initial grain sizes are all approximately $\sim \tau_s = 1$. Bai and Stone (2010a) found that only their largest grains ($\tau_s \geq 0.1$) could form significantly dense filaments.

Recent numerical studies have attempted to define the boundary where dust clumping can occur via the streaming instability in a parameter space of particle size and dust-to-gas ratio (Carrera et al. 2015; Yang et al. 2017; Li and Youdin 2021) – hereby (C15), (Y17), and (L21). A result from this last paper is shown in Figure 1.10.

One major limitation of these studies is that they are conducted in 2D, despite 3D simulations showing that dust density evolves differently in three dimensions (Johansen et al. 2007; Bai and Stone 2010a; Carrera et al. 2021).

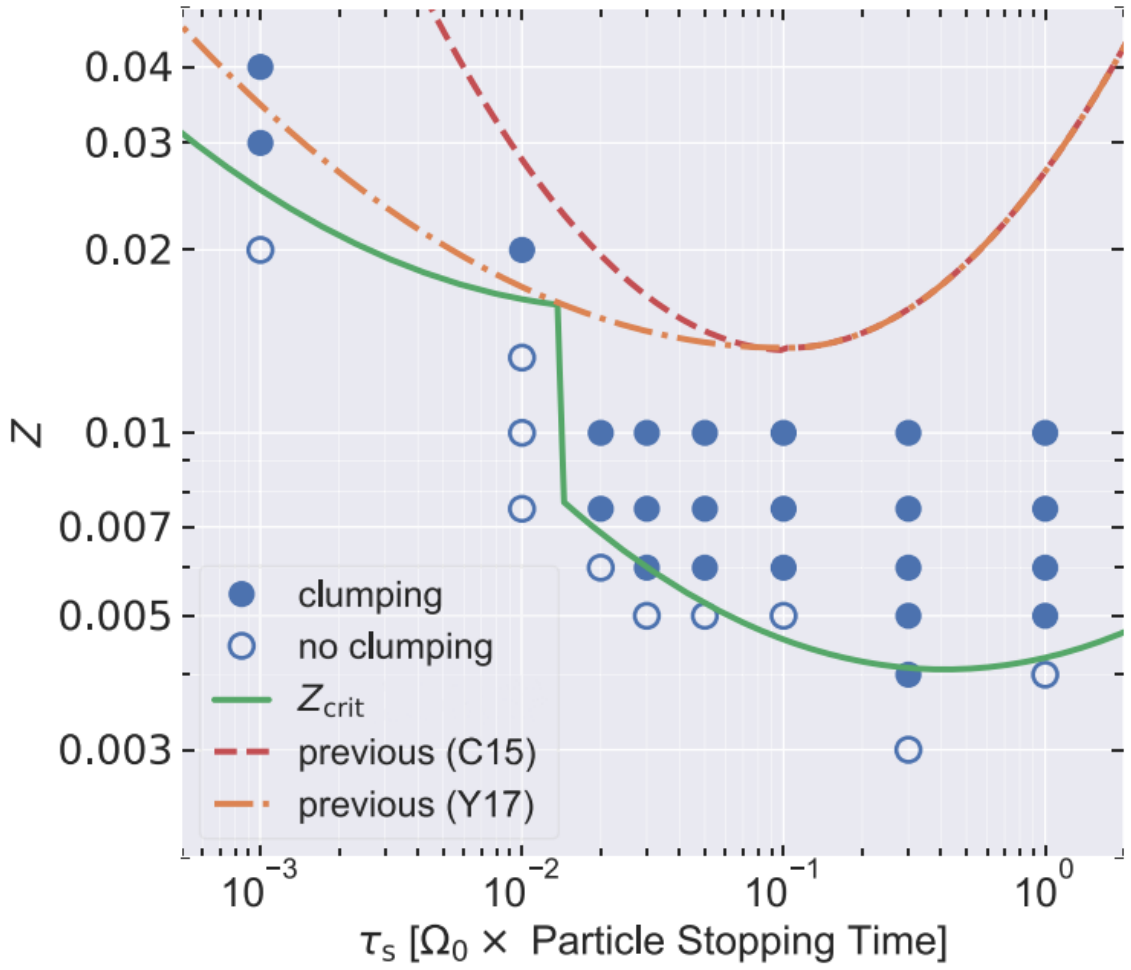


FIGURE 1.10: The green curve shows the threshold for when the SI can activate as a function of dust-to-gas ratio $Z$ and Stokes number $\tau_s$ in 2D simulations. Reproduced with permission from Li and Youdin (2021).

### 1.2.4 Late Stage Growth

In later stages of their growth, planetesimals must either collide or sweep up much smaller grains to continue growing. The latter mechanism is called pebble accretion, and it takes over once planetesimals reach $\sim$ 100 km sizes. In this process, cm- to m-size pebbles drifting in from outer regions of the disk are accreted onto moving planetary cores. Recent numerical studies have examined this process in detail (Drążkowska et al. 2021). During and after the pebble accretion stage, the resulting planetary embryos can continue to grow through giant impacts via processes called runaway and oligarchic growth. Once an embryo is large enough for its mass to condense into a spherical shape and it has cleared a path through the gas and dust in its orbit, it is considered a planet. This is the end-stage for terrestrial planets (Armitage 2020). At larger radii, there is more material in the disk and temperatures are colder. This allows planets to reach critical sizes of 5 to 10 Earth masses, at which point they undergo an additional period of growth by accreting gas onto their rocky cores to become gas giants (Perri and Cameron 1974; Pollack et al. 1996; Ayliffe and Bate 2012).

## 1.3 Thesis Overview

In this thesis, we examine the nature of protoplanetary disk turbulence using numerical simulations and semi-analytic studies of different processes in a dusty disk. We compare the characteristics of a Kelvin-Helmholtz instability (KHI) to the structure of turbulence in our simulations in order examine the KHI as a source of disk turbulence. We use our simulations to estimate $\alpha$ for a disk composed of small dust grains and investigate how different values of $\alpha$ impact planet formation.

In Chapter 2 we define the requirements of our simulation and argue that a shearing box approximation set up with the ATHENA hydrodynamic grid code is a suitable framework for our needs. We then describe how ATHENA's numerical methods work and outline the parameters in our simulations. We also briefly discuss any limitations of our approach and how our simulations compare to real physical systems.

In Chapter 3 we introduce a simulation of a simple KHI that helps us demonstrate and validate our analysis techniques. We apply these techniques to our more complicated shearing box simulations to study the nature of their velocity fields. We compare these velocities to what is expected by the NSH equilibrium and describe how the velocities evolve over time. Finally, we extract turbulent $\alpha$ values directly from our simulations. This is a key result of this thesis and a significant improvement over previous research into disk turbulence which often assumes an $\alpha$ value *a priori*.

In Chapter 4 we consolidate our extracted $\alpha$ values with previous work and some original derivations of growth barrier boundaries to explore the conditions in proto-planetary disks that are necessary to form planets and how the adjustments of key parameters can affect the outcome of the planet formation process. This allows us to understand the requirements for creating a solar system with rocky planets close to the star and gas giants further away.

We conclude with a summary of results in Chapter 5 and provide some suggestions for future work.

# Chapter 2

# Methods

Grain growth happens on small scales relative to the size of the entire disk. We therefore need a simulation framework that can resolve these scales efficiently in numerical studies.

## 2.1 Shearing Box Approximation

One popular framework is based on a local approximation of the disk that was first described by Goldreich and Lynden-Bell (1965). Consider a box that encloses a small region of a protoplanetary disk. The box is centered at a point $(r_0,\ \theta_0,\ 0)$ relative to the star, where the mid-plane of the disk is at the vertical direction's zero-point. The movement of gas and dust inside the box is described using a 3-Dimensional co-rotating Cartesian frame $(x,\ y,\ z)$ with the origin at the center of the box. The equivalent global coordinates with the star at the origin are then $(r_0 + x,\ \theta_0 + y,\ z)$.

We can describe the evolution of the gas and dust in this non-inertial reference frame:

$$\frac{\partial \rho_g}{\partial t} + \boldsymbol{\nabla} \cdot (\rho_g \mathbf{u}) = 0 \tag{2.1}$$

$$\frac{\partial (\rho_g \mathbf{u})}{\partial t} + \boldsymbol{\nabla} \cdot (\rho_g \mathbf{u}\mathbf{u}) = -\boldsymbol{\nabla} P_g + \rho_g \left[ -2\boldsymbol{\Omega} \times \mathbf{u} + 2q\Omega^2 x \hat{\mathbf{x}} - \Omega^2 z \hat{\mathbf{z}} + \mu \frac{\bar{\mathbf{v}} - \mathbf{u}}{t_{\text{stop}}} \right] \tag{2.2}$$

$$\frac{\mathrm{d}\mathbf{v}_i}{\mathrm{d}t} = 2\mathbf{v}_i \times \boldsymbol{\Omega} + 2q\Omega^2 x \hat{\mathbf{x}} - \Omega^2 z \hat{\mathbf{z}} - \frac{\mathbf{v}_i - \mathbf{u}}{t_{\text{stop}}} + \mathbf{F}_g \tag{2.3}$$

If we assume an isothermal equation of state, then the gas pressure can be written $P_g = \rho_g c_s^2$. The ratio of local volumetric dust and gas mass densities is $\mu = \rho_d / \rho_g$, $\mathbf{u}$ is the local gas velocity, and the velocity of the $i$-th dust particle is $\mathbf{v}_i$. The mass-weighted average velocity of all dust particles in a single gas cell is $\bar{\mathbf{v}}$, and the gravitational force is $\mathbf{F}_g$.

The box rotates together with the disk, and its rotation axis points along the $z$-axis: $\boldsymbol{\Omega} = \Omega \hat{\mathbf{z}}$, where $\Omega \propto r^{-q}$. The rotation is Keplerian, so $q = 3/2$ as in equation (1.3). As a result of this uniform orbital motion, there is a background velocity given by $v_k = q\Omega x$ in the $-\hat{\mathbf{y}}$ direction (Stone and Gardiner 2010). Any orbital effects from the azimuthal curvature of the disk are neglected in this local approximation, which is valid as long as the dimensions of the domain are small compared to $r_0$.

This method is called the shearing box approximation, and it is used heavily in the study of local dynamics in accretion disks (Stone and Gardiner 2010; Johansen and Youdin 2007; Bai and Stone 2010a) because it provides the required advantage of having higher resolution at the scales of interest. The trade-off is that it can't be used to calculate global disk properties or effects that arise globally, such as large scale dust migration leading to local enhancements of the dust-to-gas ratio.

## 2.2 Resolution Requirements

The next step in preparing a simulation is to identify the resolution that is required to simulate the physics of the problem. We need to consider a few important scales including that of the disk thickness $H_g$, the scales at which streaming occurs, the assumptions for KHI ($H_g \to 0$), and the length scale for viscous dissipation of turbulence (equation 1.10).

Figure 1.9 shows us the growth rates of the fastest growing grains in a linear SI, and particles of size $\tau_s = 0.01$ can meet these rates when $k\eta r \sim 100$ after settling (top panel). Many disks can be characterized by $\eta v_k = 0.05 c_s$ (Bai and Stone 2010a). Working in units of the isothermal sound speed $c_s$ and Keplerian angular velocity $\Omega = v_k/r$, we can solve for the wavenumber $k$ to calculate the scales we need to resolve if we want to simulate the linear SI.

$$\eta v_k = \eta\,(\Omega r) = \; 0.05 c_s \longrightarrow \eta = \frac{0.05}{r} \tag{2.4}$$

$$k\eta r \longrightarrow k\left(\frac{0.05}{r}\right) r \sim 100 \tag{2.5}$$

$$\implies k \sim 2000 \tag{2.6}$$

Similarily, for $\tau_s = 0.001$ we have $k\eta r \sim 1000$ and $k \sim 20\,000$. This tells us that the linear SI is weak and on extremely small scales of order $2\pi/k = 3 \times 10^{-3}$ to $3 \times 10^{-4}$ the gas scale height $H_g$. Additionally, small grains are not expected to undergo non-linear streaming (Li and Youdin 2021). The SI is of almost no importance to the small grains we want to study so we will disregard it from our resolution considerations.

The KHI does not have a minimum length scale; there will always be a large enough $k$ (small enough length) that is unstable. However, our shearing boxes will not experience an idealized KHI with a sharp discontinuity in density and velocity at the boundary of the two fluids because the gas and dust disks have finite thickness $H_g$ and $H_d$ respectively. The finite thickness suppresses large $k \gg H_g^{-1}$ (small lengths), such that it is possible to have no unstable effects at these scales (Chandrasekhar 1961). At the end of Section 1.1.4 we define the Richardson number Ri $\propto g(z)$, which describes the stability of a fluid with a finite thickness. Stable systems have large Richardson number. This indicates that gravity can stabilize a disk at small $k \ll H_g^{-1}$ (large lengths) where $H_g$ is the driving length scale of turbulence, which corresponds to the size of the largest eddies. Therefore, there is a range of instability around the preferred scale length $H_g$. Since $H_d \ll H_g$ it is key to resolve the dust scale height $H_d$ in our shearing box simulations. The cell-size will act as a dissipation length scale. We will examine how well $H_d$ is resolved in Section 3.2.1.

## 2.3 Simulation Code

The hydrodynamic grid-code ATHENA has been used extensively in the past to generate high-resolution 3D simulations of the instabilities in protoplanetary disks (e.g., Stone and Gardiner 2010; Simon et al. 2016), so it is both well-tested and capable of resolving the scales of interest in our problem. For these reasons, we use it to simulate our shearing boxes.

Our copy of ATHENA is the public C-version of the code with a modification made by Rucska (2022) to its gravity solver which allows us to include dust self-gravity in our simulation. The rest of our code is standard to ATHENA's 3D problem generator for

non-linear streaming instability in stratified disks called `par_strat3d.c` (Stone et al. 2008; Stone and Gardiner 2010).

ATHENA is based on a finite volume Godunov scheme that obeys mass, momentum, and energy conservation to machine accuracy. Numerical fluxes are calculated using the HLLC Reimann solver, and the system is evolved in time by integrating the equations of motion with the dimensionally-unsplit cornered transport upwind (CTU) integrator (Colella 1990; Toro et al. 1994; Stone et al. 2008). Both spatial and temporal integrations are accurate to second-order.

Additionally, ATHENA models dust as Lagrangian particles where the $i$-th particle with mass $m$ experiences a radially inward aerodynamic drag force given by:

$$\mathbf{F}_{\mathrm{drag,i}} = \frac{m\left(\mathbf{u} - \mathbf{v_i}\right)}{t_{\mathrm{stop}}} \tag{2.7}$$

The background velocity $v_k$ is treated separately by the orbital advection scheme, so it is subtracted from the dust momentum equations to give:

$$\frac{\mathrm{d}\mathbf{v}^{'}{}_{i}}{\mathrm{d}t} = 2\left(v^{'}_{iy} - \eta v_k\right)\Omega\hat{\mathbf{x}} - (2-q)v^{'}_{ix}\Omega\hat{\mathbf{y}} - \Omega^2 z\hat{\mathbf{z}} - \frac{\mathbf{v}^{'}{}_{i} - \mathbf{u}^{'}}{t_{\mathrm{stop}}} + \mathbf{F}_g \tag{2.8}$$

where $\mathbf{v^{'}_i} = \mathbf{v} - (q\Omega x)\,\hat{\mathbf{y}}$ and $\mathbf{u^{'}_i} = \mathbf{u} - (q\Omega x)\,\hat{\mathbf{y}}$. This improves both the accuracy and efficiency of the code (Masset 2000; Johnson et al. 2008). To maintain shear flow at the edges of the radial domain, boundary conditions in the $x$-direction are shear-periodic, whereas conditions in the $y$ and $z$ directions are pure periodic (Hawley et al. 1995; Stone and Gardiner 2010).

Following Bai and Stone (2010b), the momentum of the dust is evolved using a semi-implicit integrator, and particle properties are interpolated to and from the gas grid using the triangular-shaped cloud (TSC) scheme. If the dust grains are small and well coupled to the gas, the integrator is instead fully implicit.

The radially outward pressure gradient with profile $P_g \propto r^{-n}$ acting on the gas is equivalent in effect to a constant radial force $\mathbf{F}_{\text{grad}} = 2\eta v_k \Omega \hat{\mathbf{x}}$. The value $\eta = n\,(c_s^2/v_k^2)$ is related to the strengths of both the radial gas pressure gradient and the drag force on the dust. To approximate the radial pressure gradient without creating discontinuities at the edges of the domain, a constant and radially inward force $-\mathbf{F}_{\text{grad}}$ is added to the particles.

Rucska (2018) describes the benefit of using a hydrodynamic grid-code like ATHENA over alternatives like Smoothed-Particle Hydrodynamics (SPH). Particularly, SPH is bad at simulating small perturbations in a subsonic fluid. This is important when studying the SI or KHI.

Dust self-gravity is required for the SI to collapse dust filaments into bound clumps (see Section 1.2.3). Our code includes a modification to ATHENA developed by Rucska (2022) which incorporates dust self-gravity; it makes use of the Poisson solver implemented in ATHENA by Kim and Ostriker (2017). Boundary conditions for this gravity solver are shear-periodic in the $x$ and $y$ directions and open in the $z$ direction (Gammie 2001; Koyama and Ostriker 2009).

The gas is initialized with a vertical Gaussian profile:

$$\rho_g(z) = \rho_{g,0} \exp\left\{-\frac{z^2}{2H_g^2}\right\} \tag{2.9}$$

where $\rho_{g,0}$ is the volumetric gas mass density at the disk mid-plane.

The number of dust particles in a simulation is constant and equivalent to the number of grid cells in the box. The mass of a particle is proportional to $ZH_g s^w$ where the radius of the spherical particle is $s$, the power-law index is $w$, and the dust-to-gas ratio is $Z$. Particle positions are initialized uniformly across the $x$-$y$ plane by a random number generator. Initial distribution of dust across the $z$ direction follows the Gaussian profile described by equation (2.9) with $\rho_g \mapsto \rho_d$ and $H_g \mapsto H_d$ which is the dust scale height. The stopping time $t_{\text{stop}}$ is fixed.

Gas and dust velocities are initialized to NSH equilibrium values with a correction added to their $y$-components to account for shear flow.

## 2.4 Parameters

Five simulations were run, encompassing two different values of the Stokes number $\tau_s$ at varying resolutions. This leaves the exact radius $r$ unspecified, which allows us to rescale the box as needed. The purpose of simulating the same problem at different resolutions is to help distinguish real effects from numerical ones.

In our simulations, we set $\Omega = c_s = H_g = \rho_{g,0} = w = 1$ for these models. Since all dust particles within a simulation are the same size, they will also have the same mass. The stopping time of a particle is always equivalent to its Stokes number $\tau_s$, and all of these simulations involve well coupled small particles so the integrator is fully implicit. The radius of a spherical particle $s$ can be determined from its Stokes number (equations 1.7 and 1.8).

TABLE 2.1: Details of shearing box simulations

| Name | Particle Size | Box Size | Grid Resolution |
|---|---|---|---|
| | $\tau_s$ | $(L_x \times L_y \times L_z)$ | $(N_x \times N_y \times N_z)$ |
| `tau-3N60` | 0.001 | $0.1 \times 0.1 \times 0.4$ | $60 \times 60 \times 240$ |
| `tau-3N120` | 0.001 | $0.1 \times 0.1 \times 0.4$ | $120 \times 120 \times 480$ |
| `tau-2N60` | 0.01 | $0.1 \times 0.1 \times 0.4$ | $60 \times 60 \times 240$ |
| `tau-2N120` | 0.01 | $0.1 \times 0.1 \times 0.4$ | $120 \times 120 \times 480$ |
| `tau-2N240` | 0.01 | $0.1 \times 0.1 \times 0.4$ | $240 \times 240 \times 960$ |
| | $Z$ | $\tilde{G}$ | $\Pi$ |
| | 0.02 | 0.05 | 0.05 |

The total number of grid cells is $N_{\text{cells}} = N_x \times N_y \times N_z$
The box size is listed here in units of the gas scale height $H_g$

$\Pi$ is a parameterization of $\eta$ and $\tilde{G}$ describes the relative strengths of gas self-gravity and tidal shear.

$$\Pi \equiv \frac{\eta v_k}{c_s} \qquad \tilde{G} \equiv \frac{4\pi G \rho_{g,0}}{\Omega^2} \tag{2.10}$$

Following Bai and Stone (2010a), we set $\Pi = 0.05$ which is applicable to a wide range of disk models. We set $\tilde{G} = 0.05$ following Simon et al. (2016): this value of $\tilde{G}$ is equivalent to a Toomre $Q = 32$, which indicates that the gas disk is very gravitationally stable. Thus, we can ignore the self-gravity of the gas since there are negligible perturbations in its local density.

The shear flow correction to the NSH equilibrium velocities is $+\eta v_k \hat{\mathbf{y}} = 0.05\hat{\mathbf{y}}$ for both gas and dust in these units; there are no higher order shifts to velocity and no

non-unity factors that could further modify $\rho_s$ or the drag force. The initial dust scale height is set to $H_d = 0.05 H_g$.

The dust-to-gas ratio in our shearing box simulations is $Z = 0.02$. This is slightly larger than the fiducial value of solar metallicity $Z_\odot = 0.014$, and it also differs from the $Z = 0.01$ value commonly used in simulations of protoplanetary disks. The reason for this change is that the streaming instability (Section 1.2.3) generally requires an initial dust-to-gas ratio greater than $Z_\odot$ in order to trigger (Rucska 2022). As with most previous work, the $Z$ in our model is constant. However, it is well known that the dust-to-gas ratio in disks evolves with time (Weidenschilling 1977a).

In a simple linear convection problem for a flow speed $u$ and velocity magnitude $M$:

$$\frac{\partial u}{\partial t} + M \frac{\partial u}{\partial x} = 0 \tag{2.11}$$

The Courant–Friedrichs–Lewy (CFL) number $C$ is defined in terms of the timestep $\Delta t$ and length between cells $\Delta x$. It must generally be $\leq 1$ for convergence:

$$C = M \frac{\Delta t}{\Delta x} \leq 1 \tag{2.12}$$

Changing the CFL number will modify the timestep. The CFL number is $C = 0.4$ in all of our simulations.

We aim to run our simulations until the dust has settled and steady turbulence has been generated in the disk. Smaller grains take longer to settle, with $t_{\text{settle}} \propto \tau_s^{-1}$ for $\tau_s \ll 1$ so simulations with $\tau_s = 0.001$ are more expensive. Higher resolution runs are also expensive, so we did not run a $240 \times 240 \times 960$ simulation with $\tau_s = 0.001$.

# Chapter 3

# Turbulence Characterization

The origin, nature, and strength of turbulence in protoplanetary disks is an open question in modern astrophysics. As discussed in Section 1.1.4, turbulent mixing can facilitate coagulation between dust grains as they settle toward the mid-plane, but too much turbulence can also slow growth rates (Gole et al. 2020). It is therefore clear that a careful examination of turbulence in protoplanetary disks is necessary for a complete understanding of planet formation at every stage. We will begin with an examination of the KHI and apply our results to the shearing boxes.

## 3.1 Kelvin–Helmholtz Instability Simulation

Until recently, the MRI was thought to be very important in the generation of protoplanetary disk turbulence. It may still play a role in some regions of the disk, but evidence suggests that the MRI is not the source of turbulence in the areas of the disk where planet formation happens (see Section 1.1.4). One hypothesis for the source of turbulence in these regions is that it is generated by a Kelvin-Helmholtz instability, and previous work has explored its role in planet formation (Johansen et al. 2006).

We present a simulation of a simple Kelvin-Helmholtz instability (KHI) in this section as a proof of concept for our analysis codes. The purpose of this exercise is to ensure that our analysis produces coherent results before we apply it to the more complicated shearing box simulations. The nature of the instability in this section will not be exactly the same as in the shearing box, but it will help us understand the behaviour of Kelvin-Helmholtz instabilities more generally.

### 3.1.1 Setup and Assumptions

We extend ATHENA's 2D `kh.c` problem to three dimensions by duplicating the physics of the dimension perpendicular to flow and initializing the momentum in all three dimensions with different random seeds. We then use this framework to simulate a Kelvin-Helmholtz instability in a $480 \times 480 \times 480$ box with the following domain in code units:

$$x = [-0.5, 0.5]$$

$$y = [-0.5, 0.5]$$

$$z = [-0.5, 0.5]$$

Flow is initialized in the $x$-direction with velocities $u_{\pm}$:

$$u_- = -0.1 \text{ in the region } |y| < 0.25$$

$$u_+ = +0.1 \text{ in the region } |y| \geq 0.25$$

Both streams are initially uniform, and the initial density of the fluid is $\rho_0 = 1$ throughout the box. The pressure is $P = \frac{1}{\gamma}\rho c_s^2$ where the adiabatic index $\gamma = C_P/C_V$ is the ratio of specific heats at constant pressure and constant volume, respectively. We set $\gamma = 5/3$ for an ideal monatomic gas, and the pressure is initially $P_0 = 2.5$ everywhere. There is no magnetic field in our example. The instability is seeded by

adding random numbers with uniform distribution to all components of the velocity. These perturbations are random to mimic the behaviour of the instability in the shearing boxes, and initial perturbation velocities have a peak-to-peak amplitude $A_0 = 0.001$ centered around $u_+$. The boundary conditions are periodic everywhere, and the CFL number is $C = 0.4$.

### 3.1.2 Velocity Field and Turbulence

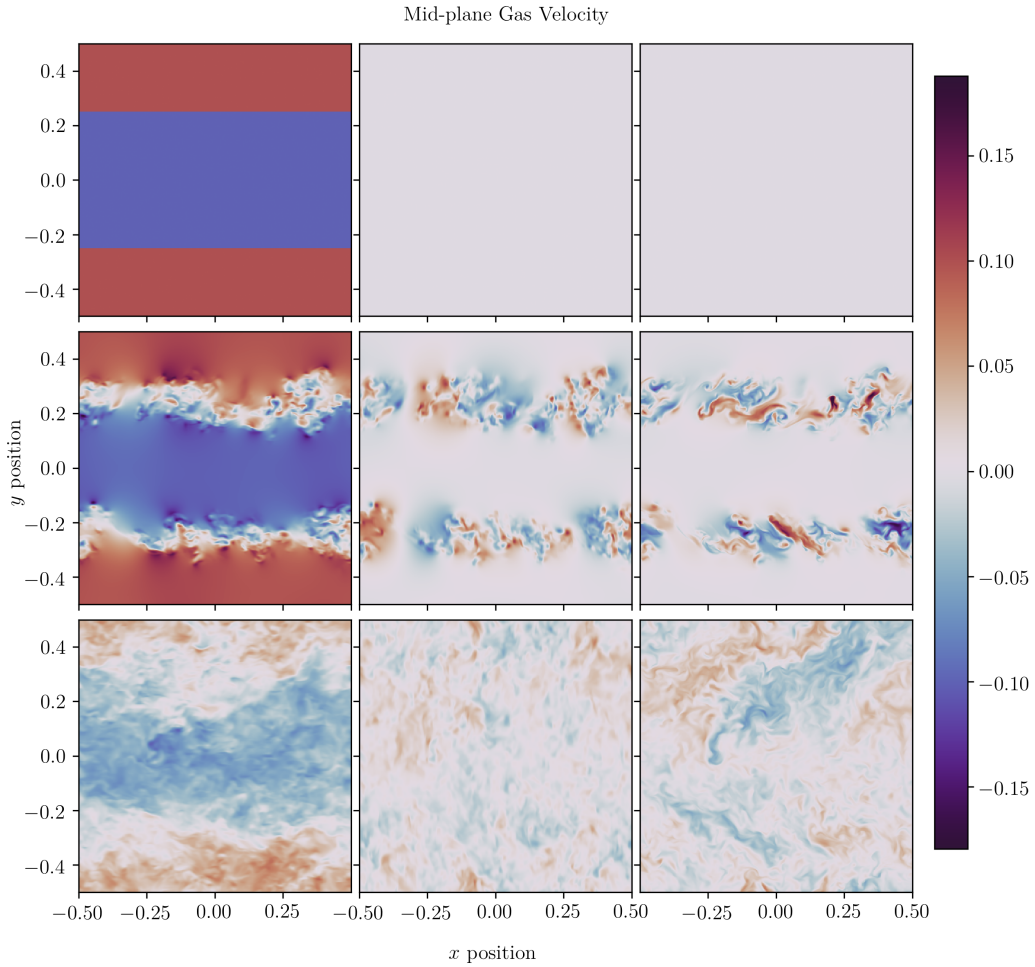


FIGURE 3.1: A visualization of the velocity fields in the KHI simulation at three different times for $z = 0$. From left to right, the columns show $v_x, v_y$, and $v_z$. *Top:* initial conditions at $t = 0$. *Middle:* the instability forms by $t = 10$. *Bottom:* at late time $t = 50$.

We expect to see the instability once perturbation amplitudes $A = A_0 \exp\{i\omega t\}$ are appreciable, around $A = 0.1$ to $A = 1$. In code units, this occurs at times $t = 5$ to $t = 7$. Figure 3.1 visualizes the velocity field at the beginning of the simulation, at some time after the non-linear instability forms, and at a late time to show how the instability spreads in all three dimensions.

We can study the structure of the turbulence in this system by subtracting the mean velocity from the field and plotting a power spectrum of what is left over. Figure 3.2 shows the total and component-wise power spectra for this KHI; all of the curves follow a Kolmogorov-like profile $k^{-5/3}$ in the inertial range (see Section 1.1.4) and a $k^{-6}$ profile in the dissipative range, which matches findings by San and Maulik (2018). The curves in the separate directional component spectra all lie on top of each other, which means that the turbulence is isotropic as expected. Comparing the shape of this power spectrum to the ones from the shearing boxes will help us characterize the turbulence in our disks. Also, note that we cannot measure past the Nyquist frequency at $k = N/2$, so this region of each plot is greyed out in Figure 3.2.

It is important to note that in this test, the density is uniform throughout the simulation domain, there is no vertical gravity or dust, and flow is only in one direction. In the presence of dust, there is a stabilizing effect as a result of the density contrast with the heavier fluid (consisting of both gas and dust) underneath the gas. This configuration leads to a static stability that can be destabilized by flow (Scott 2022). Therefore, this test does not exactly replicate the instability in the shearing boxes, but the general behaviour is correct.

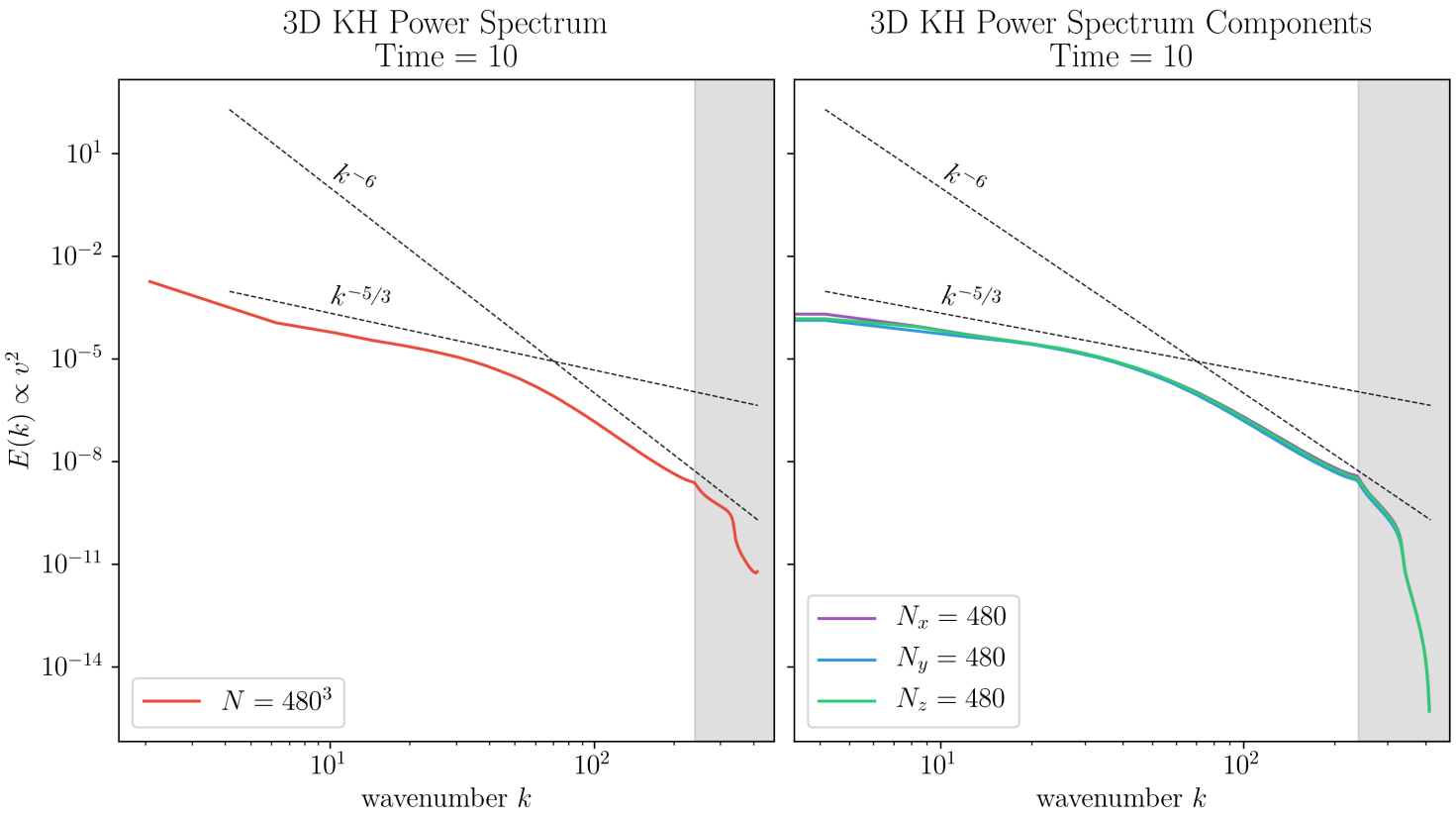


Figure 3.2: Energy spectra of the simple KHI at time = 10
*Left:* total power spectrum. *Right:* component power spectra

## 3.2 Turbulence in a Protoplanetary Disk

In this section we will take a closer look at our shearing boxes. Each simulation was run for as long as possible, with the minimum stopping condition being that the system had settled. A visualization of the dust surface density in the boxes at the end of each run is given in Figure 3.3. We focus on `tau-2N120` as the standard case for analysis. We will examine how the velocity field in the shearing boxes is structured and how it changes over time. We pay attention to how closely the velocities follow the NSH equilibrium (Section 1.2.3) because any deviation is a result of turbulence in the box. We will then apply the analysis from the previous section to our shearing boxes in order to characterize this turbulence. Finally, we measure $\alpha$ directly from simulation data.

### 3.2.1 Dust Scale Height

Over time, the dust in the shearing boxes settles to the mid-plane. The top panel of Figure 3.4 shows how the dust scale height $H_d$ evolves for the simulations with $\tau_s = 0.01$ and the bottom panel does the same for the simulations with $\tau_s = 0.001$. Since the lower resolution runs were able to reach later times, Figure 3.4 also includes a zoomed-in view to make the curve for the highest resolution run clearer.

The settling time $t_{\text{settle}}$ is proportional to $\tau_s^{-1}$ and this is what we see in Figure 3.4, where $t_{\text{settle}}$ is approximately 200 $\Omega^{-1}$ for $\tau_s = 0.01$, and 1000 $\Omega^{-1}$ for $\tau_s = 0.001$. After this point, disk turbulence grows (see Figure 3.8) and kicks up the particles enough to thicken the dust scale height to a final value. The simulation is considered to have "settled" once $H_d$ levels out.

All of the boxes have vertical length $L_z = 0.4H_g$; this corresponds to $N_z = 240$ grid-cells for the low resolution runs and 960 grid-cells for the highest resolution run (see Section 2.4). The size of a single grid-cell is the numerical dissipation scale in our shearing boxes. Better resolution therefore corresponds to a smaller dissipation length, so smaller modes can contribute to turbulence in the box. See Gerbig et al. (2020) for a similar discussion of resolution effects when simulating the SI. In summary, a greater amount of turbulence is able to be generated in the $N_x = 120$ and $N_x = 240$ runs, which thickens the dust scale height. The dust settles at a larger $H_d$ compared to their low resolution $N_x = 60$ counterparts. However, the final $H_d$ is converging: we can see that the distance between the $N_x = 240$ and $N_x = 120$ curves in the top panel of Figure 3.4 is smaller than the distance between the $N_x = 120$ and $N_x = 60$ curves.

We can examine how well $H_d$ was resolved in the shearing box simulations. Figure 3.4 shows that the $N_x = 60$ run for $\tau_s = 0.01$ reaches a final dust scale height of $H_d \simeq 0.008H_g$ which corresponds to $(0.008/0.4) \times 240 \simeq 5$ grid cells. Similarly, the $N_x = 120$ run resolves $H_d$ to 13 grid-cells and the $N_x = 240$ run resolves it to 38 grid-cells. From this information and by noting how much shorter the highest resolution simulation was able to run, we can conclude that resolutions with $N_x > 240$ would be very computationally expensive while not offering much benefit due to the convergence of final $H_d$ with resolution.

The dust surface density at the end point of each run is shown in Figure 3.3. Dust is more concentrated toward the mid-plane at lower resolutions, due to a smaller amount of turbulence generating. In Figure 3.4 we can see that this difference in $H_d$ is always present between different resolutions, even when they are compared at the same time. As predicted in Section 2.2, there is no clumping in any of the simulations so the SI

is not part of our considerations with these small grains. We will therefore focus our efforts on characterizing the KHI in these runs.

### 3.2.2 Velocity Structure and Evolution

The $y$-velocity of the gas is plotted in Figure 3.5 for run `tau-2N120` at three different times: the beginning of the simulation, the settling time $t_{\text{settle}}$, and at the end of the run. In each shearing box, the initial velocitites are set to the NSH equilibrium values with $\eta v_k$ added to the $y$-components to account for the background flow. This is shown in the top right panel of Figure 3.5, where the velocity curves line up exactly with the NSH values given by the solid black curve.

During the settling stage, the width of the dust layer shrinks and the velocities start to spread about the NSH values (Figure 3.5 lower left panel). The dashed lines mark the minimum and maximum velocities at each height. By the end of the run, turbulence kicks in and increases the width of the dust layer again to intermediate thickness (Figure 3.5 lower right panel). The shaded area indicates the region $\langle v_y \rangle \pm \sigma_y$ where $\sigma_y$ is the standard deviation of the $y$-velocity. This spread around the NSH velocity tells us that there is turbulence present in the box, and that it appears gradually over the course of the run.

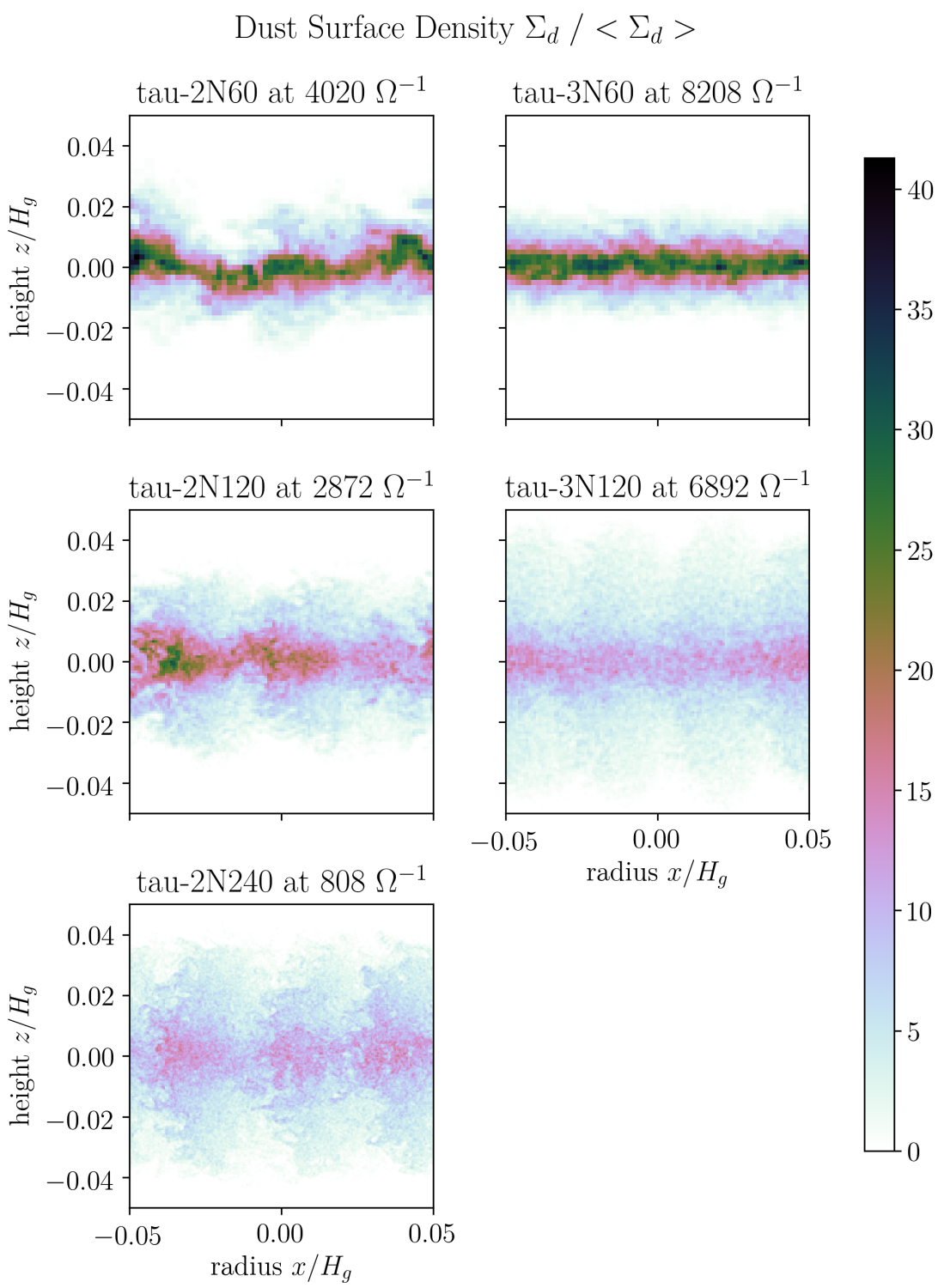


FIGURE 3.3: The dust surface density of the shearing box simulations at the end of each run for $y = 0$. Each plot is zoomed into the mid-plane.

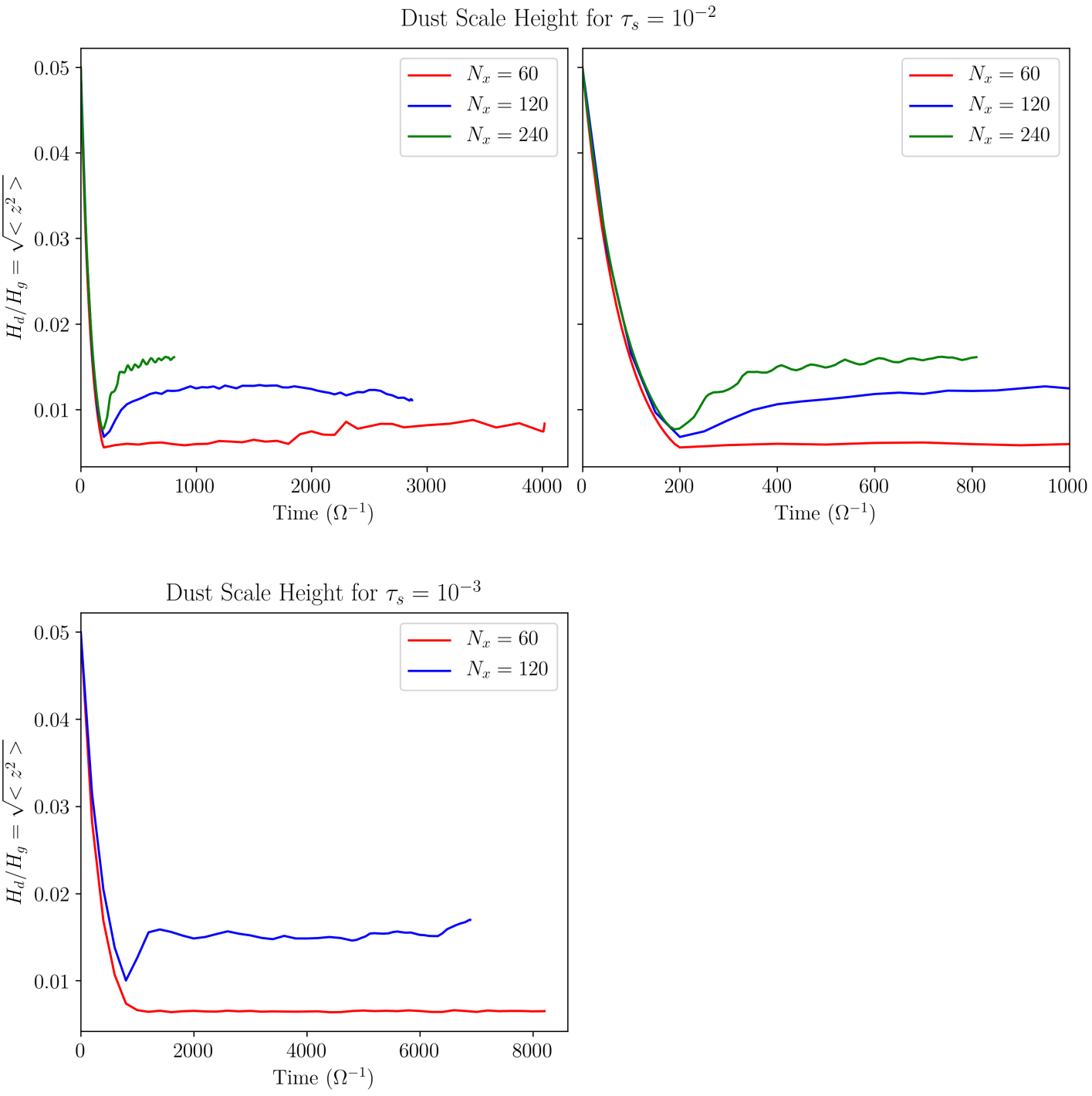


FIGURE 3.4: *Top:* evolution of the dust scale height $H_d$ for $\tau_s = 0.01$. On the right is a zoomed-in view. *Bottom:* evolution of the dust scale height $H_d$ for $\tau_s = 0.001$.

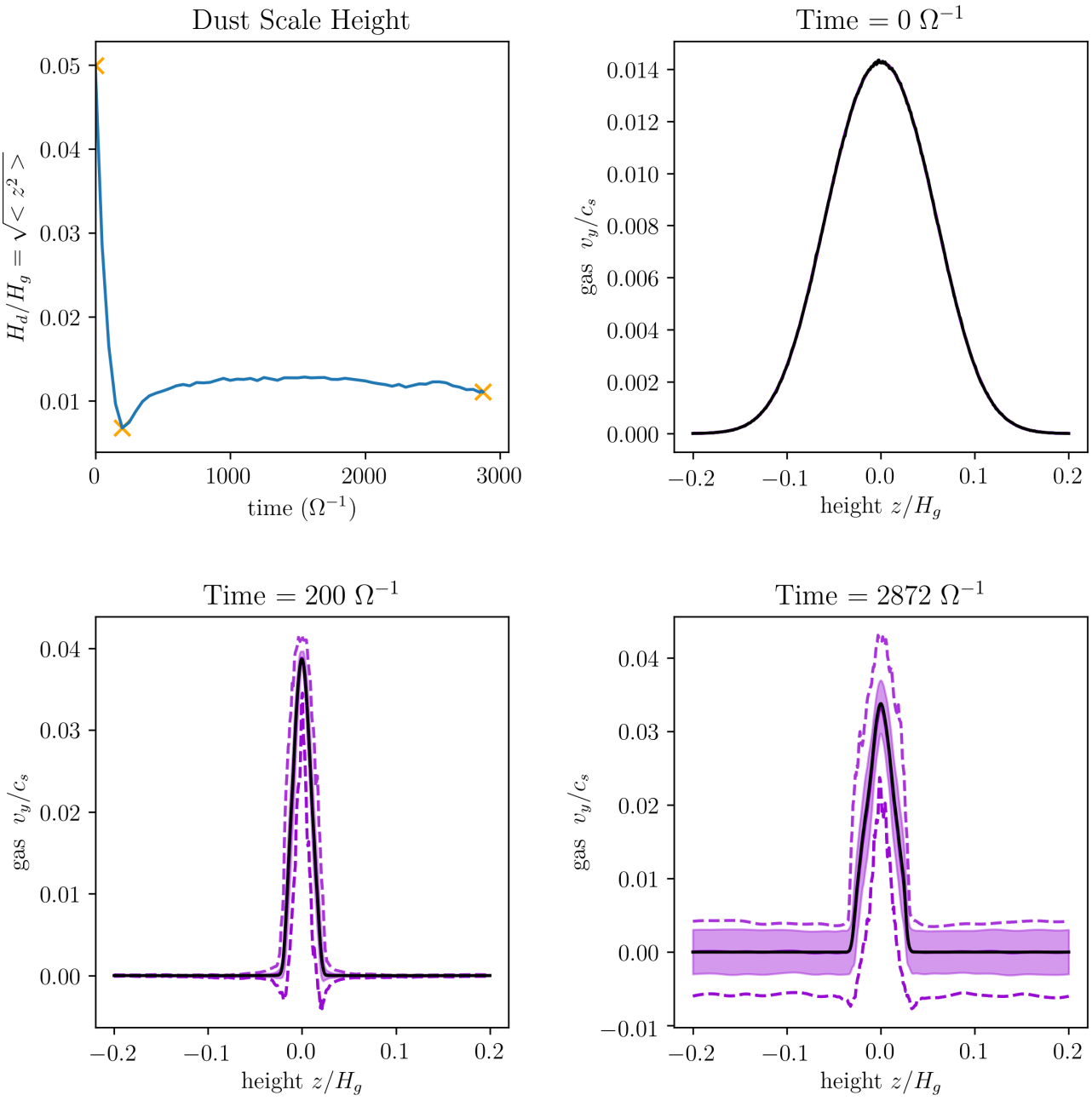


FIGURE 3.5: The $v_y$ gas velocities in tau-2N120 are shown at the three different times marked in the top left panel. The solid black curve shows the NSH equilibrium predictions, the dashed curves show the minimum and maximum velocities, and the shaded region indicates the area $\langle v_y \rangle \pm \sigma_y$ where $\sigma_y$ is the standard deviation of $v_y$

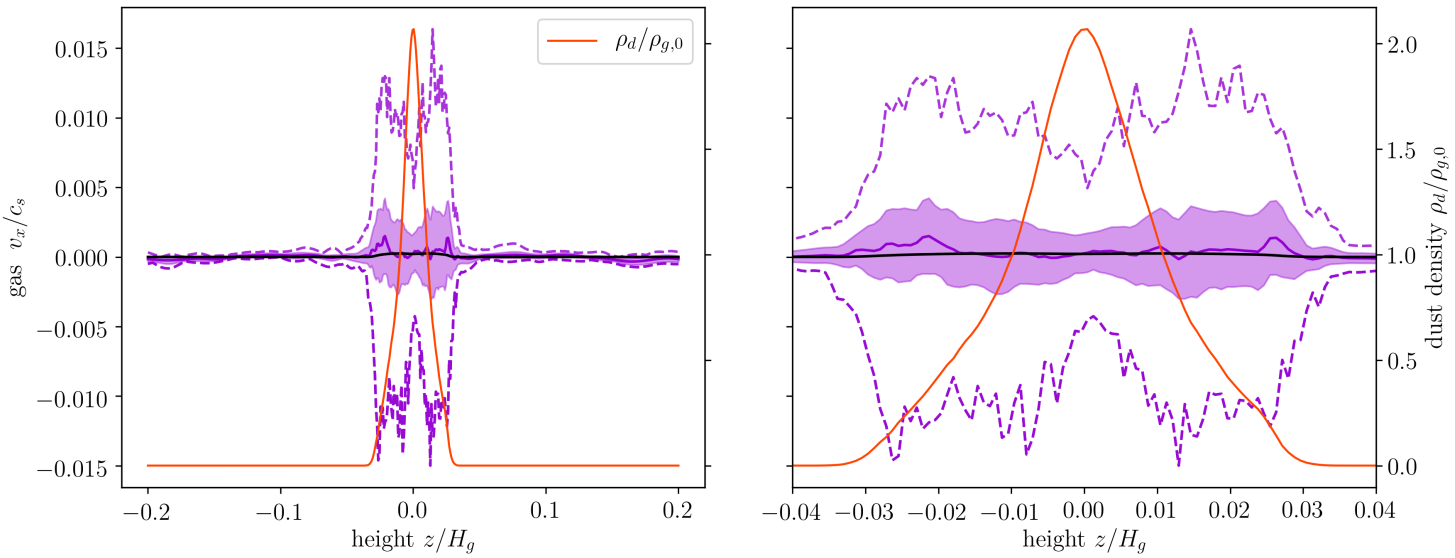


FIGURE 3.6: Gas velocity in tau-2N120 at 2872 $\Omega^{-1}$ with the dust density superimposed. On the right is a close-up of the same image at the disk mid-plane; the range of $z$ on the right coincides with the maximum vertical extent of dust grains at this simulation time.

In Figure 3.6 we see that there is very little activity in the velocity of the gas outside of the dusty mid-plane. This is consistent with a KHI, which is driven by a velocity gradient between the dust and gas layers. The solid purple curve is the mean velocity $\langle v_x \rangle$.

In Figure 3.7 we see that turbulence is present in both the dust and gas at approximately equal strengths by the end of run `tau-2N120`. Another way to check the relative strengths of the dust and gas turbulence is to plot the velocity dispersions for dust and gas: $\sqrt{\langle \rho_d (v_i - \overline{v_i})^2 \rangle / \langle \rho_d \rangle}$ with $i = d$, $g$ for dust and gas respectively. We've weighted the dispersions by the dust density $\rho_d$ in order to focus on the turbulence as experienced by the dust, since this is what impacts growth rates. The result is Figure 3.8, which shows us that the dust and gas turbulence is in fact of similar magnitude. The dust moves slightly slower because the grains are so small that the drag force slows them down considerably.

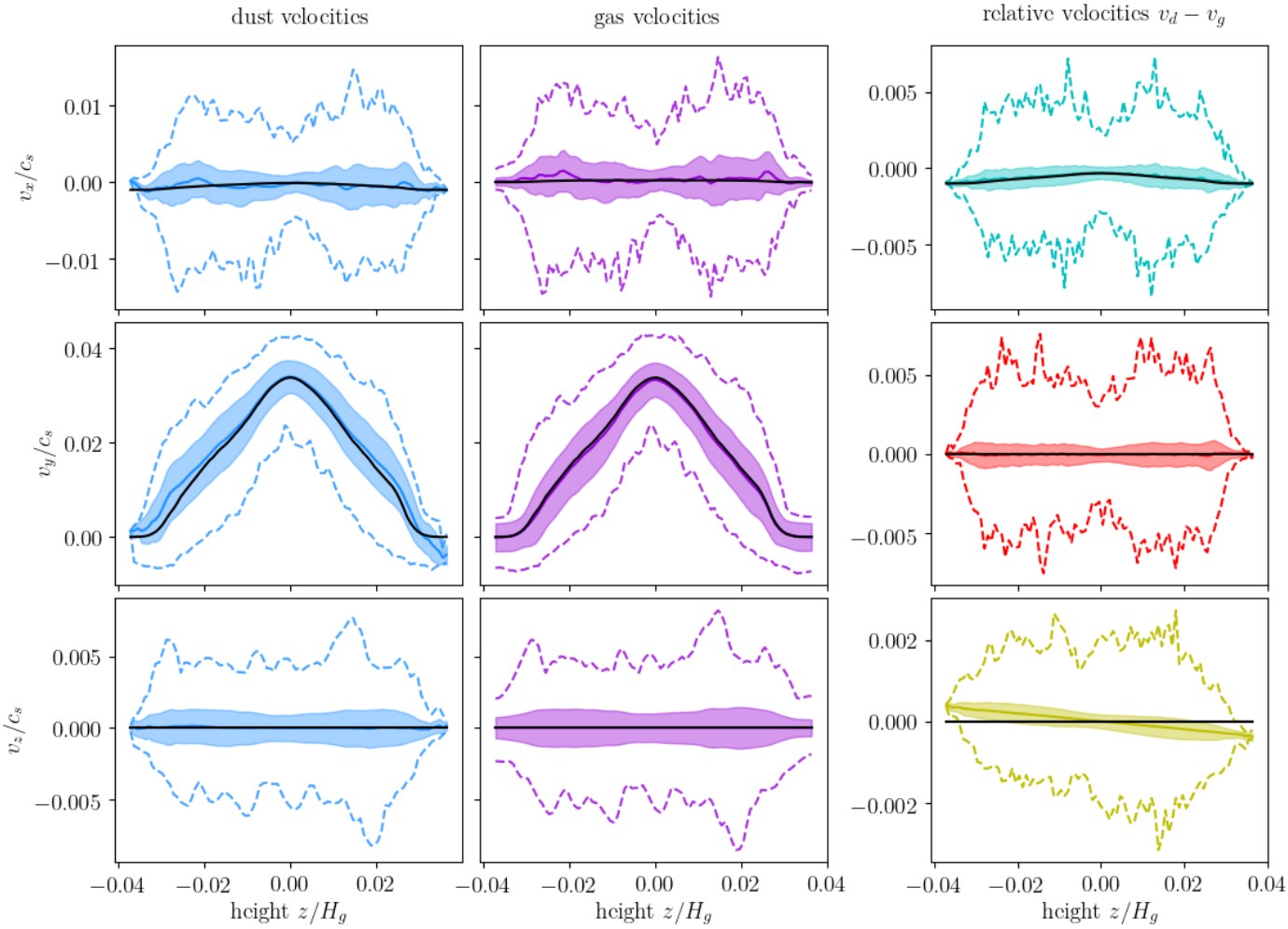


Figure 3.7: Gas and dust velocities in tau-2N120 at 2872 $\Omega^{-1}$ with relative dust−gas velocities at the same time.

At the end of Section 1.1.4, we give the definition of the Richardson number Ri which describes the stability of a finitely thin fluid. Classically, a value of $\mathrm{Ri} > 0.25$ indicates stability, while $\mathrm{Ri} < 0.25$ is a necessary (but not sufficient) condition for instability (Chandrasekhar 1961; Sekiya 1998). The classical results are idealized and assume completely uniform density and velocity gradients. Numerical simulations have shown that this critical Richardson number is closer to $\mathrm{Ri}_{\mathrm{crit}} = 1$ when the Coriolis force is taken into account (Gómez and Ostriker 2005; Johansen et al. 2006). Therefore, $\mathrm{Ri} \gtrsim 1$ is stable, and $\mathrm{Ri} \lesssim 1$ is necessary for instability.

Figure 3.9 shows the Richardson number for `tau-2N120` at three different times during the settling stage $t < t_{\mathrm{settle}}$. The horizontal axes in the right column are limited to where dust can be found. This figure shows that the vertical region of the box that is potentially unstable slowly narrows over time as the dust settles to the mid-plane. At the same time, there is now more material in this region which can promote collisions between particles. A similar plot is given in Figure 3.10 at the end of the run, which shows that the vertical region of instability does not change much after $t_{\mathrm{settle}}$.

Figures 3.9 and 3.10 also include plots of $\mathrm{d}\rho/\mathrm{d}z$ where the total density is $\rho = \rho_g + \rho_d$. Regions with $\mathrm{d}\rho/\mathrm{d}z < 0.1\%$ of its peak value indicate noise due to very few dust grains being present, and they are shaded in these plots. The Richardson number estimates in these regions are not valid.

It is important to note again that the standard Richardson number applies to a fluid with uniform density and velocity gradients. In our case, $u$ and $\rho$ in equation (1.11) are composed of both gas and dust values. Additionally, $g = g(z)$ in our case is not constant. This could introduce uncertainties into our calculation of Ri.

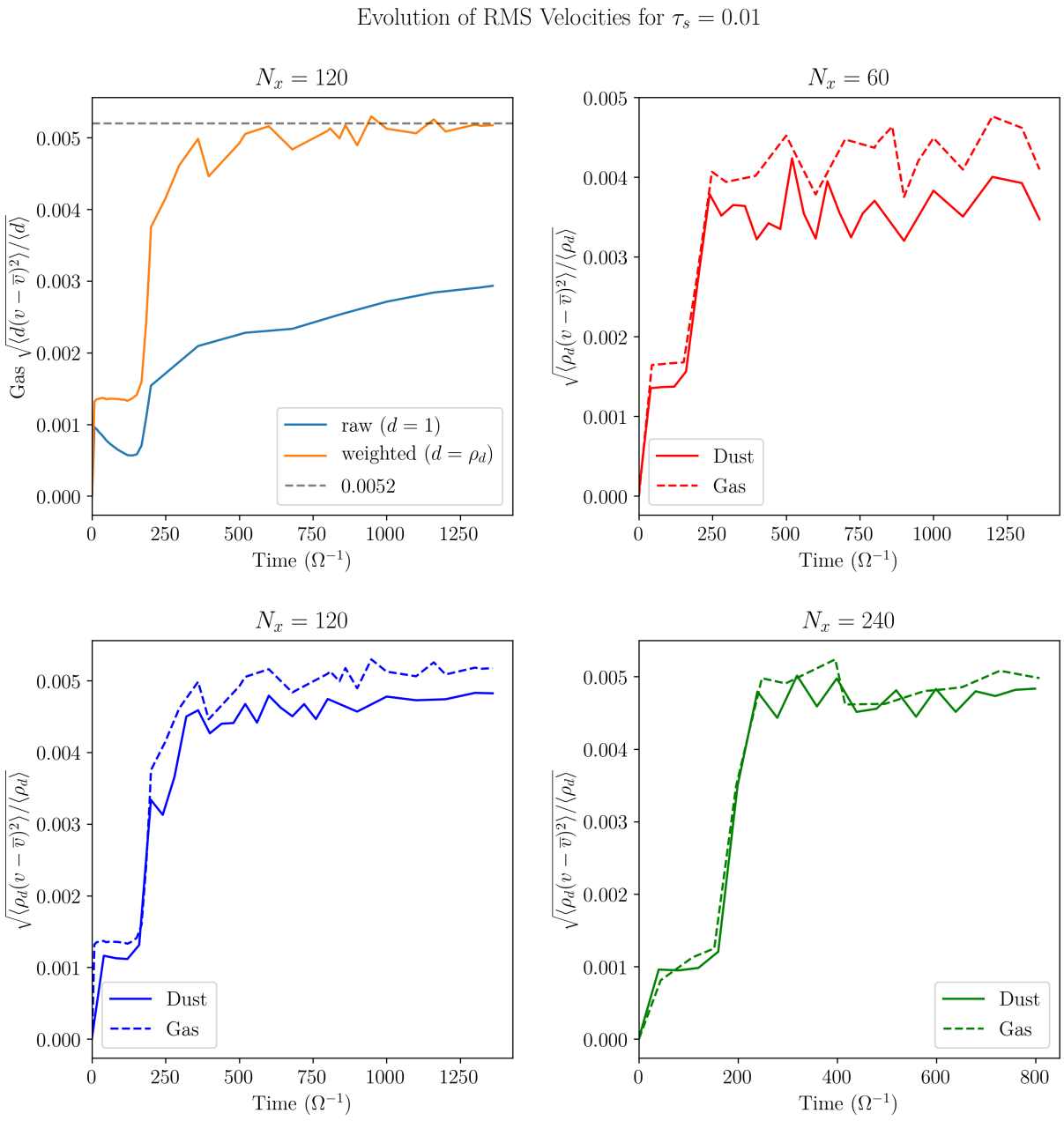


FIGURE 3.8: *Top Left:* evolution of gaseous velocity dispersion in tau-2N120. The orange curve is the raw value and the blue is weighted by the dust density. *Top Right and Bottom Row:* evolution of gas and dust velocity dispersions for $\tau_s = 0.01$ at three different resolutions.

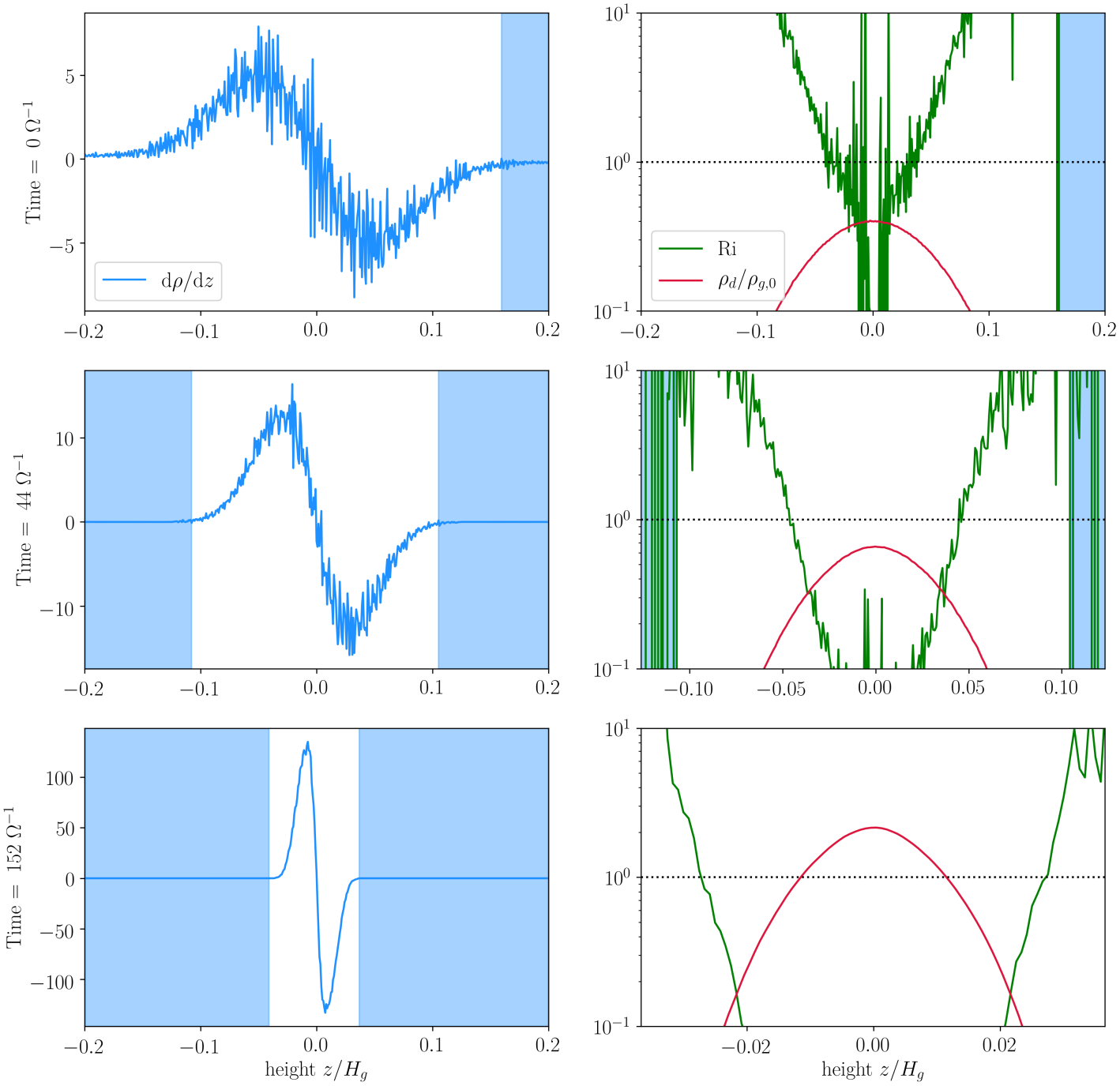


FIGURE 3.9: *Left*: $\mathrm{d}\rho/\mathrm{d}z$ where $\rho$ is the total dust and gas density. Regions with significant noise are shaded. *Right*: the Richardson number of the disk superimposed with the dust density. These plots are from tau-2N120.

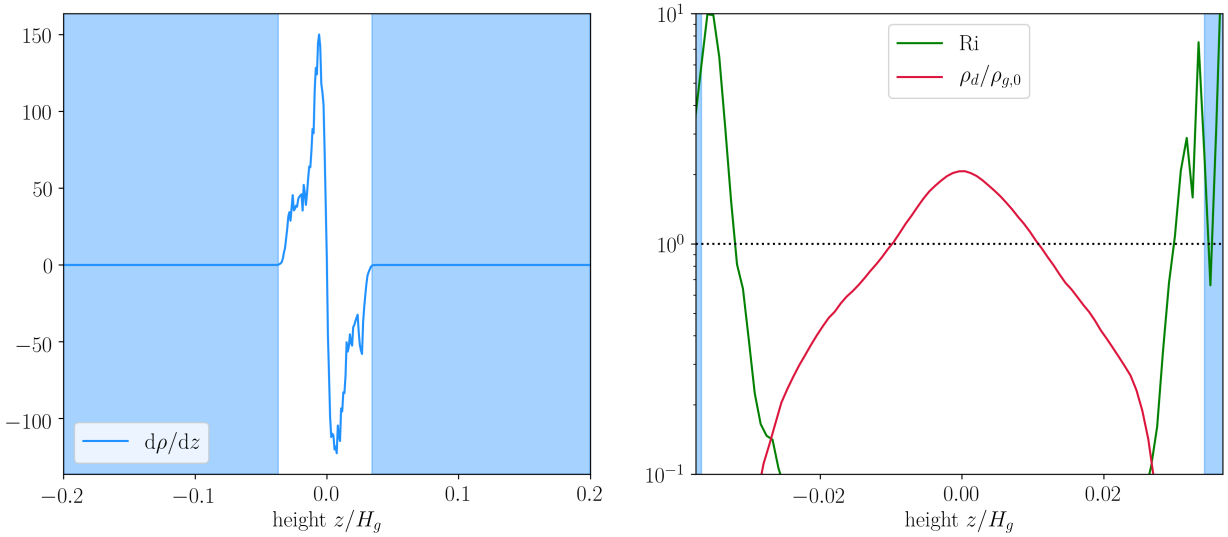


FIGURE 3.10: *Left:* $\mathrm{d}\rho/\mathrm{d}z$ and *Right:* Richardson number with dust density superimposed for tau-2N120 at 2872 $\Omega^{-1}$

### 3.2.3 Energy Spectra

Figures 3.11 and 3.12 show the total power spectrum of all the shearing box simulations. All profiles follow a Kolmogorov power law in the inertial range and have the expected slope in the dissipative range (see Sections 1.1.4 and 3.1.2). Spectra beyond the Nyquist frequency at $k = N_x/2$ are not physically meaningful and omitted in subsequent plots.

The component spectra for run `tau-2N120` in Figure 3.13 shows that energy in the system is distributed approximately isotropically, with slightly less energy stored in the radial direction. Figure 3.14 shows the total power spectrum of this simulation at 80%, 90%, and 100% of its run. All these curves lie on top of each other, further indicating that the system has settled and that the turbulent state is steady. We demonstrate that sharp peaks for small $k$ in any of the power spectra can be attributed to binning effects (see Figure 3.15). When this error is minimized, like in Figure 3.14, it becomes clear that there are no preferred wavenumbers in the shearing box.

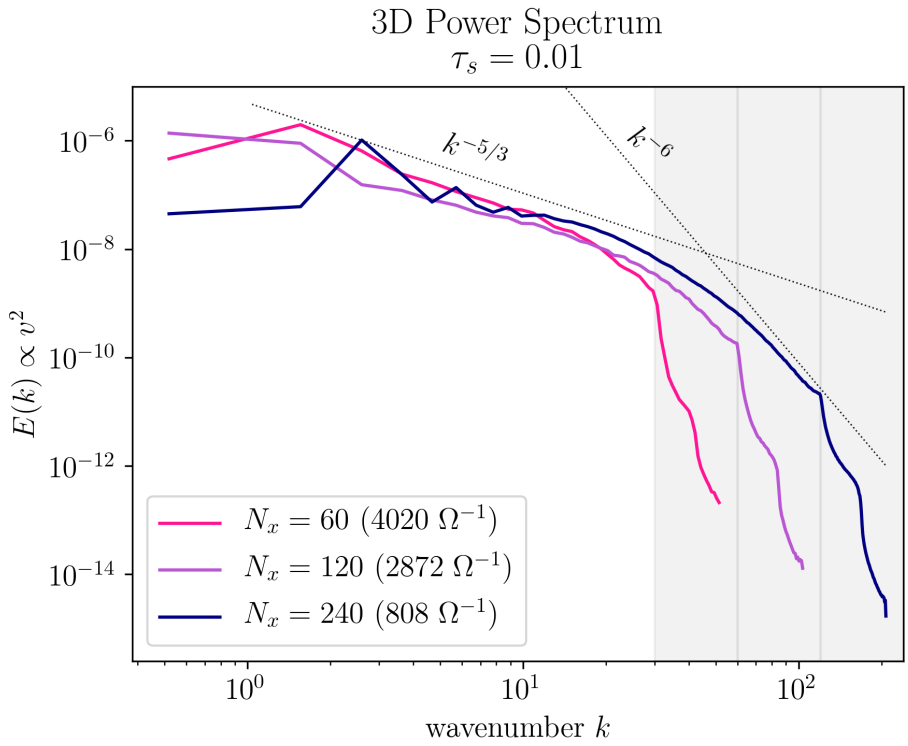


FIGURE 3.11: Total power spectrum in shearing boxes for $\tau_s = 0.01$

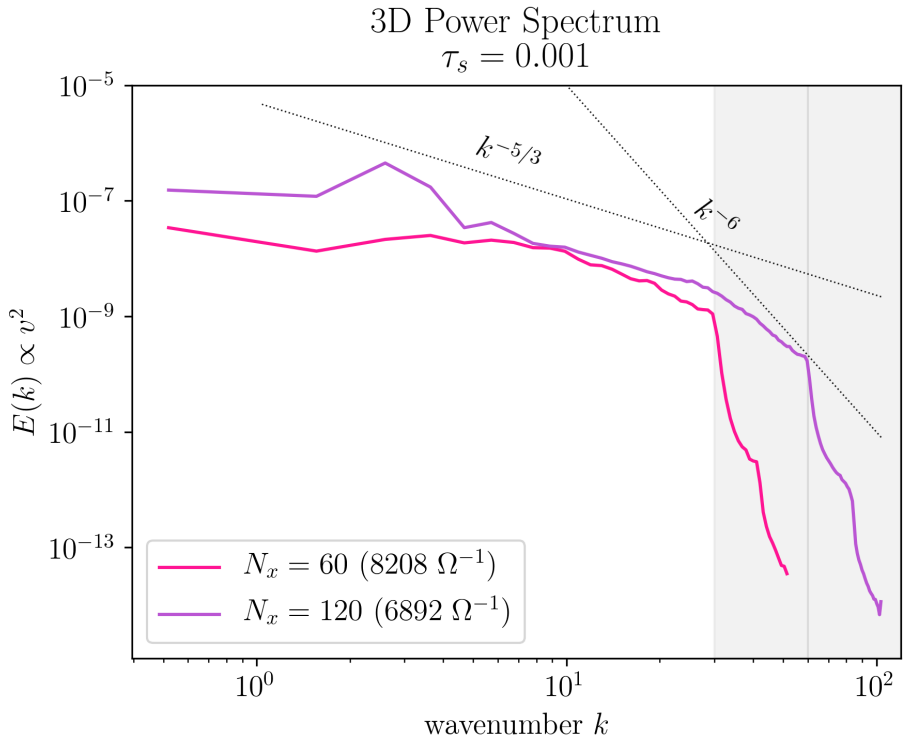


FIGURE 3.12: Total power spectrum in shearing boxes for $\tau_s = 0.001$

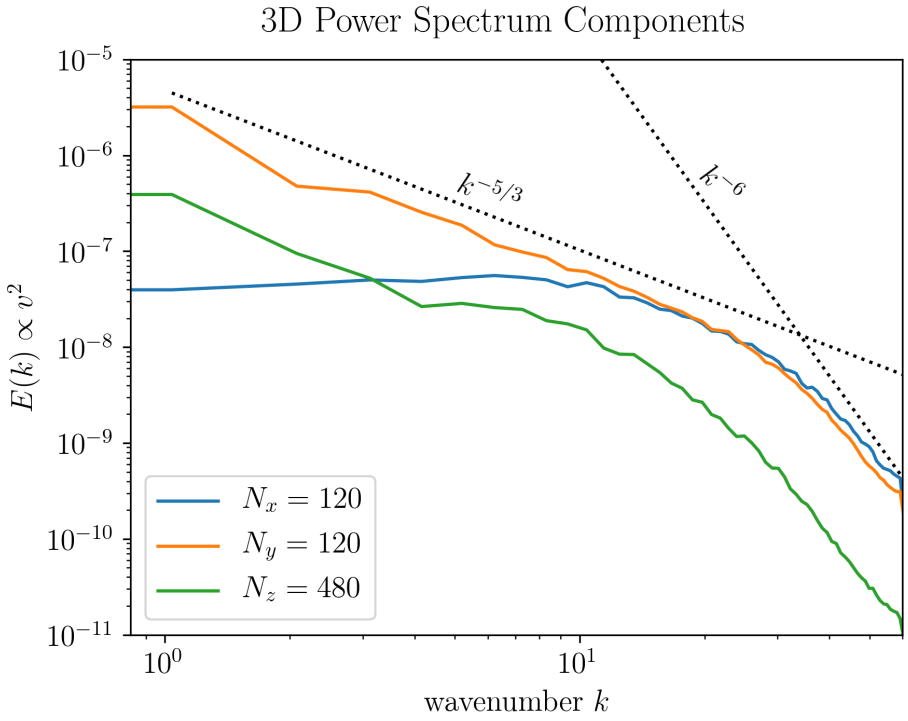


Figure 3.13: The components of the 3D power spectrum in tau-2N120

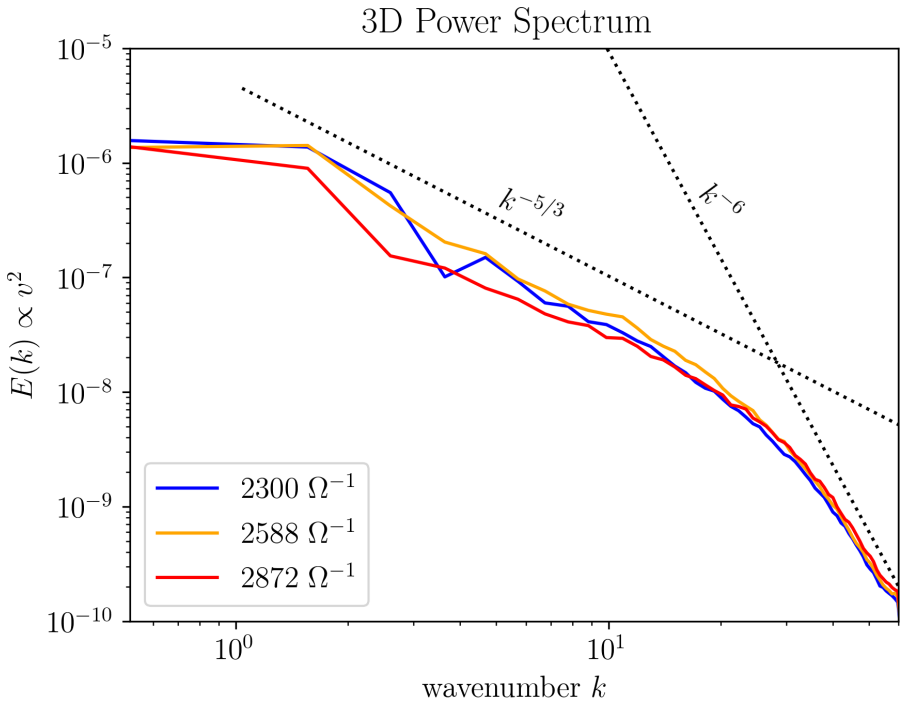


Figure 3.14: Evolution of the total power spectrum in tau-2N120. This shows that the turbulent state is steady.

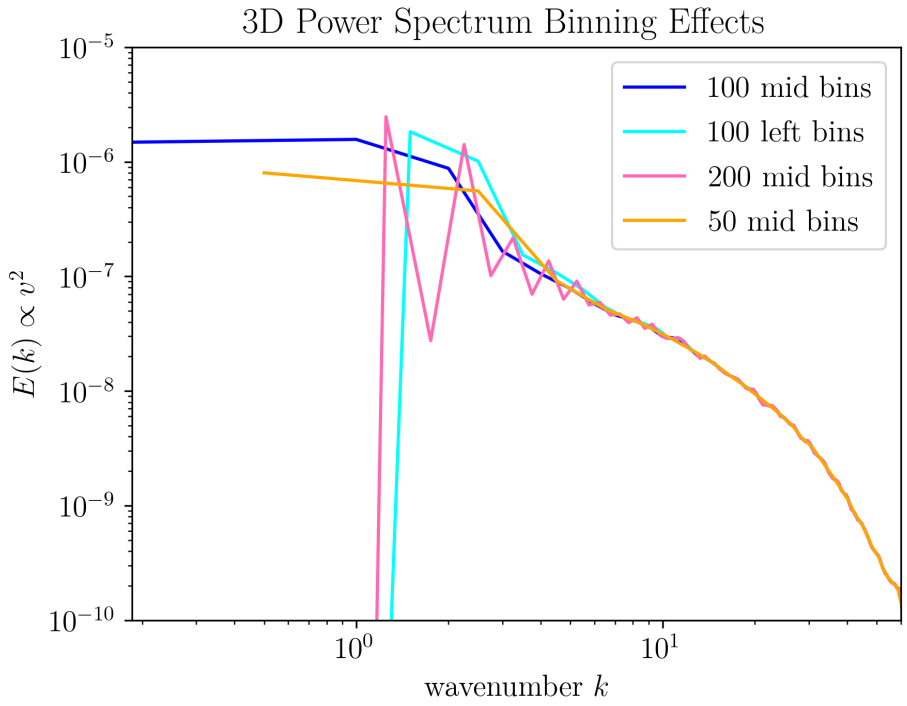


FIGURE 3.15: The effects of different binning in the total power spectrum of tau-2N120 at 2872 $\Omega^{-1}$. The number of bins and the alignment of their centers (mid = middle, or left) is shown. This figure demonstrates that the spectrum is noisy (due to small numbers of modes) for $k \leq 5$ but robust for larger $k$.

### 3.2.4 Extraction of $\alpha$

We can write the velocity of the largest gaseous eddies in a turbulent disk as $v_L = c_s\sqrt{\alpha}$ (Cuzzi et al. 2001). By measuring $v_L$ in our simulations, we can extract an $\alpha$ from the shearing box. In our case, $v_L$ is equivalent to the gaseous velocity dispersion plotted in Figure 3.8. It is important to note, however, that the exact relationship between velocity dispersion and $\alpha$ relies on specific assumptions on the nature of the turbulence. The errors introduced by these assumptions is on the order of $\sim 2$. There exist other methods of estimating $\alpha$ from velocities, such as in Simon and Hawley (2009), in which $\alpha = \langle \rho v_x \delta v_y \rangle / \langle \rho c_s^2 \rangle$. Here, $v_x$ and $v_y$ have the mean velocity in $x$ and $y$ subtracted from them (respectively), and $\rho$ is the total density of dust and gas. $\delta v_y$ is a small change in $v_y$.

The Cuzzi et al. (2001) approach characterizes the turbulence itself, and thus their equation for $\alpha$ is directly relevant for grain growth and fragmentation. The Simon and Hawley (2009) approach originates in the MRI/MHD community and uses $\alpha$ to measure the effective turbulent viscosity. It is concerned with the implications for the torque and angular momentum flux. The value for $\alpha$ from these two approaches do not have to be the same for a complex turbulent disk structure, and are only similar for idealized 3D turbulence. The values for $\alpha$ obtained using the Simon and Hawley (2009) approach are numerically smaller, which suggests that implications for slow processes like accretion onto the star are different to the implications for eddies and relative motions between dust grains. There may only be academic interest in small values of $\alpha$ that characterize torque and effective viscosity if disk winds play a larger role than turbulence in the accretion rate of disks. Finally, the $\alpha$ from Cuzzi et al. (2001) corresponds better to the $\alpha$ estimated from line widths. It is difficult to translate the torque-characterizing $\alpha$ into an expected line width.

The raw gaseous velocity dispersion in the box increases with time (top left panel in Figure 3.8), but we cannot use the entire box to examine turbulent properties. The gas extends to regions much higher than the dust layer, including beyond the limits of the simulation box. Therefore any measurement of the velocity dispersion based on the gas alone will not converge with height. Additionally, the KHI driving the turbulence is responding to the velocity gradient that is created by the presence of the dust, and so the instability is absent far from the dust. We make the assumption that the best place to characterize the turbulence in terms of its amplitude and the characteristic vertical length scale is around the dust layer. We are only interested in the turbulence as experienced by the dust grains because it is what affects the growth rate of the dust via turbulent mixing: turbulent eddies cause collisions that can lead to coagulation or fragmentation.

Figure 3.8 shows the evolution of the gas and dust velocity dispersions in three simulations with $\tau_s = 0.01$. The $N_x = 120$ and $N_x = 240$ runs seem to approach the same weighted velocity, but the lower resolution $N_x = 60$ run was not able to develop enough turbulence.

We provide a summary of results in Table 3.1. All velocity dispersions for $\tau_s = 0.01$ are taken at 800 $\Omega^{-1}$, and the velocity dispersions for $\tau_s = 0.001$ are taken at 5000 $\Omega^{-1}$ to ensure that the dust has settled and for ease of comparison between runs. When calculated with the Cuzzi et al. (2001) method, $\alpha$ increases with resolution and grain size and approaches a single value in the high resolution limit.

Estimates on the upper limit of $\alpha \sim 10^{-3}$ in protoplanetary disks have been given by measurements of molecular line widths (Flaherty et al. 2015; Teague et al. 2016). The turbulence extracted from our shearing boxes is two orders of magnitude smaller

TABLE 3.1: Turbulent $\alpha$ extracted from the shearing boxes

| Simulation | Cuzzi et al. (2001) | Simon and Hawley (2009) |
|---|---|---|
| `tau-3N60` | $6.3 \times 10^{-6}$ | $9.2 \times 10^{-7}$ |
| `tau-3N120` | $1.1 \times 10^{-5}$ | $2.1 \times 10^{-7}$ |
| `tau-2N60` | $1.9 \times 10^{-5}$ | $3.1 \times 10^{-6}$ |
| `tau-2N120` | $2.7 \times 10^{-5}$ | $1.3 \times 10^{-6}$ |
| `tau-2N240` | $2.5 \times 10^{-5}$ | $5.4 \times 10^{-7}$ |

than this limit; such a weak turbulence may slow the growth of dust grains during the coagulation stage but, if growth is able to reach sufficient sizes despite this, a small $\alpha$ might allow growth at larger scales because fragmentation can be avoided (Gole et al. 2020). In the next section, we will provide a detailed examination of the effects of this $\alpha$ value on the growth of grains in various kinds of protoplanetary disks.

Note again that the conversion between velocity dispersion and turbulence is difficult and has an error of order unity. Possible sources of error include whether or not the system being studied has fully settled and the nature of the turbulence. For example, is the turbulence isotropic? Are there any effects from magnetic fields? What is driving it? Since the exact relationship between velocity dispersion and $\alpha$ is an area of current research (Teague et al. 2016; Flaherty et al. 2018; Ormel and Cuzzi 2007), it is likely that corrections may be required to our extracted values of $\alpha$ at some point in the future when this relationship is better understood. The values in Table 3.1 could also be improved by averaging over many snapshots to get a smoothed velocity dispersion.

# Chapter 4

# Implications for Planet Formation

In this section, we explore the implications of our results for planet formation. We will follow the growth of micron-sized dust grains through every stage of planetesimal formation in various kinds of disks via semi-analytic considerations. Along the way, we will apply results from the previous sections of this thesis to develop a big-picture understanding of what is required to form planetary systems.

## 4.1 Semi-Analytical Setup

Consider a flared protoplanetary disk with radial extent $r_c$ around a star of mass $M_*$ and luminosity $L_*$. The temperature of a disk $T$ heated by the star can be described by equation (1.4). A single dust grain that is settling toward the mid-plane at early times will grow as a result of coagulation (Section 1.2.1). We can describe this particle's vertical position in the disk $z$ and its mass $m$ as a set of coupled ordinary differential

equations (Dullemond and Dominik 2005):

$$\frac{\mathrm{d}z}{\mathrm{d}t} = -\frac{3\Omega^2 z m}{4\rho_g c_s \sigma_g} \tag{4.1}$$

$$\frac{\mathrm{d}m}{\mathrm{d}t} = Z \times \rho_g \left|\frac{\mathrm{d}z}{\mathrm{d}t}\right| \sigma_g \tag{4.2}$$

where $Z$ is the dust-to-gas ratio (Section 1.1.2). If we assume that the disk is vertically isothermal and that the gas density obeys hydrostatic equilibrium, the volume density of the gas is an exponentially decreasing function of $z$:

$$\rho_g(r,z) = \frac{\Sigma_g(r)}{\sqrt{2\pi} H_g(r)} \exp\left\{\frac{-z^2}{2H_g^2(r)}\right\} \tag{4.3}$$

If $s$ is the radius of a spherical dust particle, then the collisional cross-section for grain-gas interactions is:

$$\sigma_g = \pi s^2 \tag{4.4}$$

We solve equations (4.1) and (4.2) numerically, substitute equation (4.4), and solve for $s$ to get the final size of the particle after settling as a function of its location in the disk $s_{\mathrm{settle}}(r)$. The grain may continue to grow after settling via turbulent mixing and the streaming instability if necessary conditions are met (Section 1.2), but its growth might also be halted by radial drift or the fragmentation barrier (Section 1.2.2). In order to understand the sizes that grains can reach, it is therefore also necessary to quantify any possible growth barriers.

We follow Birnstiel et al. (2012) and Birnstiel et al. (2016) to model the radial drift barrier as a function of the particle's radial position:

$$s_{\text{drift}}(r) \simeq 0.35 \frac{\Sigma_d(r)}{\rho_m q} \left( \frac{H_g(r)}{r} \right)^{-2} \tag{4.5}$$

The gas volume density is given by $\rho_g \propto \Sigma_g/(2H_g)$. We have $\Sigma_g \propto r^{-1}$, $T \propto r^{-1/2}$, and $\Omega \propto r^{-3/2}$. This gives us $c_s \propto r^{-1/4}$ and $H_g \propto r^{5/4}$ for a flared disk (see Section 1.1.2). All together, this results in a fixed power law for the gas pressure profile $P \propto \rho_g T \implies P \propto r^{-q}$, with $q = 11/4$.

For particles of equal size, the relative turbulent velocities between particles is given in Birnstiel et al. (2016):

$$\Delta v_{\text{turb}} = \sqrt{\frac{3\alpha}{\tau_s + \tau_s^{-1}}} c_s \tag{4.6}$$

If we set $\Delta v_{\text{turb}}$ to the fragmentation threshold velocity $v_{\text{frag}}$ and rearrange equation (4.6) for the Stokes number $\tau_s$ defined by equation (1.8), we will get a function that describes the size at which the fragmentation barrier prevents growth:

$$s_{\text{frag}}(r) = \frac{\Sigma_g}{\rho_m \pi} \left[ 3\alpha \left( \frac{c_s}{v_{\text{frag}}} \right)^2 \pm \sqrt{9\alpha^2 \left( \frac{c_s}{v_{\text{frag}}} \right)^4 - 4} \right] \tag{4.7}$$

A particle of size $s$ at radius $r'$ will fragment upon collision with another grain of similar size if $s_f^-(r') < s < s_f^+(r')$, where $s_f^-$ is the smaller root of equation (4.7) and $s_f^+$ is the larger root. See Figure A1 in Gonzalez et al. (2017) for more information. Note that it is possible to have no solution, in which case dust grains should never

exceed the fragmentation velocity for any size. Equation (4.7) is an original derivation in this thesis, and it is different from the fragmentation limit derived in Birnstiel et al. (2016) which makes the assumption that grains are small. Our derivation does not make this assumption.

A particle's fragmentation threshold velocity $v_{\rm frag}$ is determined by several properties of the grain, including its size and composition (Section 1.2.1). According to experiments, silicates fragment at $\sim$ 1 m/s, but icy rocks can withstand speeds of up to $\sim$ 10 m/s (Blum and Wurm 2008; Gundlach and Blum 2014).

We incorporate a water ice-line $r_{\rm ice}$ into our model disks by calculating the point where the temperature drops to $T_{\rm disk} < 150$ K (Armitage 2020). We set the fragmentation threshold velocity for particles at $r \geq r_{\rm ice}$ to 10 m/s, because the dust in this region is primarily composed of water ice. Particles at $r < r_{\rm ice}$ will have a fragmentation threshold velocity of 1 m/s as they are mostly silicates. The initial dust-to-gas ratio $Z_0(r)$ is four times larger for $r \geq r_{\rm ice}$ compared to the inner disk (see Section 1.1.2).

We can also loosely model the threshold at which there is a possibility for the SI to kick in and further increase the size of the particle. From Birnstiel et al. (2016), we can write the size of a particle as a function of its Stokes number. Note that $\rho_m$ could in principle change with composition.

$$s(r) = 2\left(\frac{\Sigma_g(r)}{\pi\rho_m}\right)\tau_s \tag{4.8}$$

Looking up the dust-to-gas ratio $Z(r)$ on Figure 1.10 will give us the corresponding $\tau_{\rm SI}$ value on the green curve. This curve separates the simulations in which there was clumping from those that did not form any clumps. If we substitute $\tau_s = \tau_{\rm SI}$

into equation (4.8), we get a function that might describe the minimum size required $s_{SI}(r)$ for the streaming instability to complete the transition to large planetesimals at a given radius.

It is important to note that this "streaming threshold" is *very* approximate: the original paper by Li and Youdin (2021) is based on 2D numerical simulations and similar studies with 3D simulations are inconclusive (Rucska 2022). The applicability of Figure 1.10 to real disks is not clear. Additionally, the authors of Li and Youdin (2021) fit the green threshold curve in Figure 1.10 by eye because it represents a theoretical boundary that follows a discrete number of simulations. Finally, Figure 1.10 only covers a narrow range of values, so I fit a function to the green curve in order to model disks that were not represented on the domain of the plot. However, any extrapolation based on this figure is quite uncertain.

Next, we will allow the disk to age by toggling between a `YOUNG/EVOLVED` parameter. The total initial mass of any disk $M_{\rm disk}$ defaults to 3% the stellar mass. In young disks, the maximum radius is $r_c$ and the gas surface density is given by Andrews et al. (2009) with a surface density gradient of unity. At early times, the dust and gas surface densities are related by $Z_0$ (Drążkowska et al. 2021):

$$\Sigma_{g,0} = \frac{M_{\rm disk}}{(2\pi r_c^2)} \left(\frac{r}{r_c}\right)^{-1} \exp\left\{-\frac{r}{r_c}\right\} \tag{4.9}$$

$$\Sigma_{d,0} = Z_0 \times \Sigma_{g,0} \tag{4.10}$$

The surface density profiles follow a power law in the inner disk and taper off exponentially at large radii (Lynden-Bell and Pringle 1974).

For evolved systems, we assume that disk winds prevent the disk from expanding such

that the maximum size of the gas disk is still $r_c$. The maximum radius of the dust disk $r_{\rm dust}$ is set to half the size of the gas disk as a result of radial drift. The mass of the dust disk (excluding water-ice) $M_{\rm dust}$ is initially equal to the $Z_0$ value inside the ice-line multiplied by $M_{\rm disk}$. We will account for any increase or decrease in local dust mass due to radial drift, particle pile-up, or the presence of an ice-line by modifying $\Sigma_d$ directly.

The mass of the gas disk is $M_{\rm gas} = M_{\rm disk} - M_{\rm dust}$ and the surface densities become:

$$\Sigma_g = \frac{M_{\rm gas}}{(2\pi r_c^2)} \left(\frac{r}{r_c}\right)^{-1} \exp\left\{-\frac{r}{r_c}\right\} \tag{4.11}$$

$$\Sigma_d = \frac{M_{\rm dust}}{(2\pi r_c^2)} \left(\frac{r}{r_{\rm dust}}\right)^{-1} \exp\left\{-\frac{r}{r_{\rm dust}}\right\} \tag{4.12}$$

For $r \geq r_{\rm ice}$ the dust density $\Sigma_d$ is multiplied by 4.

We mimic the effect of particle loss through radial drift by forcing $\Sigma_d/\Sigma_g$ to remain at or below the initial dust-to-gas ratios $Z_0(r)$ everywhere in the disk. However, we need to add back some of this dust according to Birnstiel et al. (2010): they predict a pile up of particles at the ice-line that can cause the dust-to-gas ratio within $r < r_{\rm ice}$ to increase by up to 160× its initial value. We multiply the dust surface density $\Sigma_d$ at $r < r_{\rm ice}$ by a constant $e$ to represent this pile-up, with $1 < e < 160$.

To ensure that we do not end up with more dust than we started with, we check that the final ratio of the mass $M_{f,d}$ of all non water-ice particles to the total gas mass $M_{f,g}$ is less than or equal to the initial dust-to-gas ratio within the ice-line: we require $M_{f,d}/M_{f,g} < Z_0(r < r_{\rm ice})$. Birnstiel et al. (2010) also note that in their model, they need the gas surface density $\Sigma_g \sim 1000$ gcm$^{-2}$ at $r = 0.1$ AU so we make this check as well. If $\Sigma_g$ is too large, the initial mass of the disk $M_{\rm disk}$ is reduced.

## 4.2 Model Disks

We will now present a collection of plots showing the growth lines and barriers discussed in the previous section. A table summarizing the different parameters in each disk is below.

TABLE 4.1: Parameter variation in model disks

| Disk | $M_*$ [2] | $L_*$ [3] | $M_{\rm disk}$ [2] | $r_c$ [4] | $\alpha$ | $Z_0$ [5] | $e$ [6] | $r_{\rm ice}$? |
|---|---|---|---|---|---|---|---|---|
| A | 1 | 1 | 0.03 | 100 | $2.7 \times 10^{-5}$ | 0.01 | – | No |
| B | 1 | 1 | 0.03 | 100 | $2.7 \times 10^{-5}$ | 0.01 | – | Yes |
| C | 1 | 1 | 0.03 | 100 | $1 \times 10^{-3}$ | 0.01 | – | Yes |
| D | 1 | 1 | 0.03 | 100 | $2.7 \times 10^{-5}$ | 0.01 | 1.64 | Yes |
| E | 1 | 1 | 0.03 | 100 | $2.7 \times 10^{-5}$ | 0.01 | 2.5 | Yes |
| F | 1 | 1 | 0.03 | 100 | $2.7 \times 10^{-5}$ | 0.01 | 16 | Yes |
| G | 1 | 1 | 0.80 | 100 | $2.7 \times 10^{-5}$ | 0.01 | 2.5 | Yes |
| H | 2 | 11 | 0.03 | 100 | $2.7 \times 10^{-5}$ | 0.01 | 2.5 | Yes |
| I | 1 | 1 | 0.03 | 150 | $2.7 \times 10^{-5}$ | 0.01 | 2.5 | Yes |
| J | 1 | 1 | 0.03 | 100 | $2.7 \times 10^{-5}$ | 0.01 | 5 | Yes |
| K | 1 | 1 | 0.03 | 100 | $2.7 \times 10^{-5}$ | 0.02 | 5 | Yes |
| L | 1 | 1 | 0.03 | 100 | $1 \times 10^{-3}$ | 0.01 | 5 | Yes |
| M | 1 | 1 | 0.03 | 100 | $1 \times 10^{-3}$ | 0.02 | 5 | Yes |

[2] units of $M_\odot$
[3] units of $L_\odot$
[4] in AU
[5] initial dust-to-gas ratio at $r > r_{\rm ice}$ in disks with an ice-line ($Z_0$ inside the ice-line is a quarter of this number); in disks without an ice-line, the listed value is the initial dust-to-gas ratio everywhere
[6] only applicable to evolved disks

For all disks, we will follow a spherical dust particle with internal density $\rho_m = 1.6$ g/cc (Birnstiel et al. 2012) and initial radius $s_0 = 1$ $\mu$m that starts at a height $z_0 = 4H_g$ above the mid-plane.

First, consider a solar mass, solar luminosity star with a gas disk that extends to $r_c = 100$ AU. With disks containing a solar-type star in its center, it is important to note that this would not be the mass and luminosity of our own Sun during its pre-main-sequence lifetime. We set $\alpha = 2.7 \times 10^{-5}$, which is the value extracted from our `tau-2N120` run (Section 3.2.4).

**(A)** Disk A (Figure 4.1) shows a young disk with no ice-line. We set $Z = 0.01$ and $v_{\rm frag} = 1$ m/s everywhere. The dust particle starts at some $r$ on the horizontal axis and travels toward the upper left of the plot. On its way, it can hit any of the solid curves. Once it reaches the solid green curve, it has reached the maximum size possible from settling alone $s_{\rm settle}(r)$. If disk turbulence is strong enough, the particle can continue to grow toward the solid red streaming threshold $s_{\rm SI}(r)$. In the inner part of the disk $r < 0.6$ AU, the particle hits the solid blue fragmentation limit $s_{\rm frag}(r)$ (equation 4.7) before it can undergo streaming: any grain in the blue region will fragment following collision. In the outer region, streaming can occur before the fragmentation curve limits further growth. The solid grey line is the drift limit $s_{\rm drift}(r)$ (equation 4.5), which does not set an upper bound on the grain size in this particular disk. Planetesimal formation is not possible in any region where the dust grain meets the solid blue or solid grey lines from below before it meets the solid red line. An evolved disk with no ice-line is identical to Disk A because we have forced $\Sigma_d/\Sigma_g$ to be less than or equal to $Z_0$ everywhere in the disk to mimic radial drift. Enhancements in dust surface density due to a pile up of dust or the freezing of water in an evolved disk will only occur at an ice-line. The choice of $\tau_s = 0.01$ or 0.001 in our shearing box

simulations falls along parallel curves between the green and red curves; these sizes were chosen to see if the particles would undergo streaming. Since they did not, we can surmise that turbulence was not strong enough in our simulations to bridge the gap between the green and red curves for particles of this size. The distance between the red and green curves is determined by Figure 1.10.

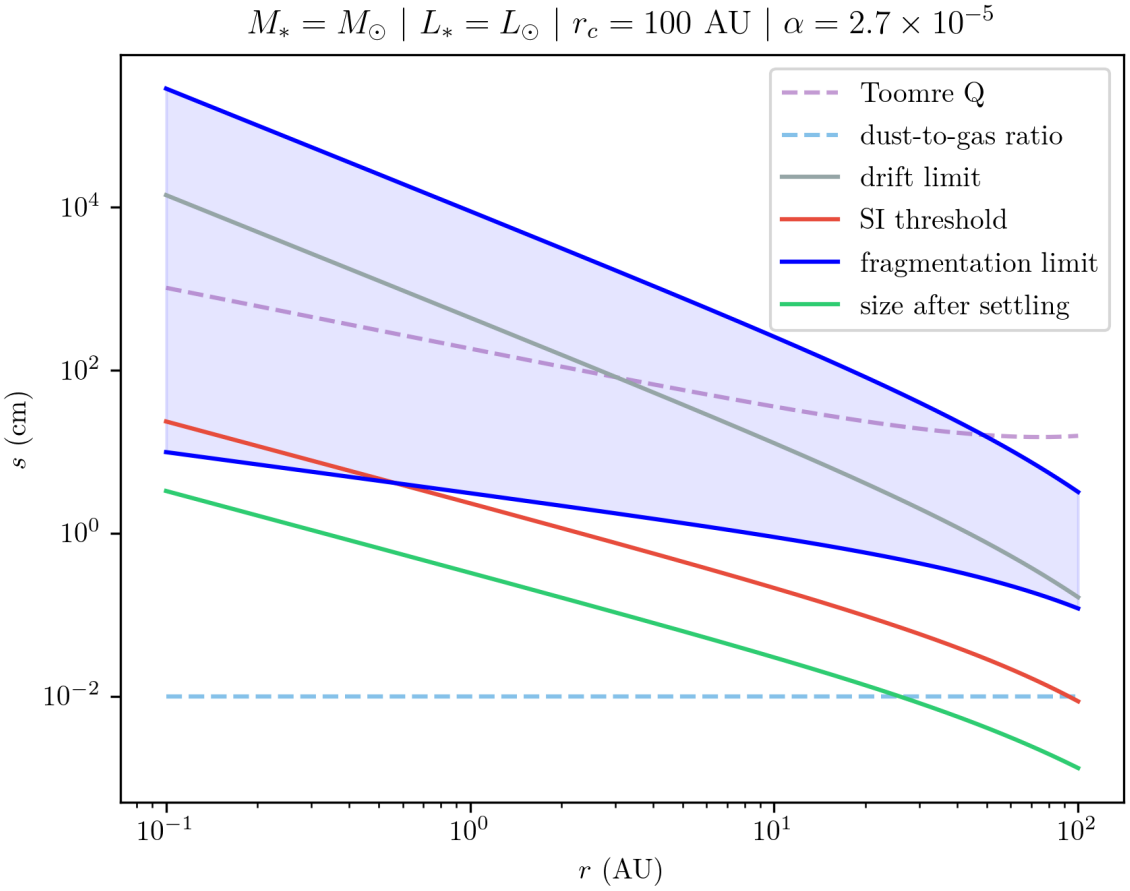


FIGURE 4.1: *Disk A*: a young disk without an ice-line and $\alpha = 2.7 \times 10^{-5}$

**(B)** We can introduce an ice-line into Disk A. Its location is $r_{\text{ice}} = 1.7$ AU, which is the expected naïve value for a solar-type star if factors like disk optical depth effects on temperature and adjustments to the disk surface density profile associated with accretion are not considered (Lecar et al. 2006). $Z = 0.01$ for $r \geq r_{\text{ice}}$ and 0.0025 for $r < r_{\text{ice}}$. The fragmentation threshold velocity increases to 10 m/s beyond $r_{\text{ice}}$ which

results in a discontinuity in the fragmentation limit. The chosen $\alpha$ is not strong enough to fragment icy solids (see Figure 4.14), so there is no fragmentation limit beyond the ice-line in this disk. Additionally, the dust-to-gas ratio inside the ice-line $(0.01/4) = 0.0025$ is not high enough to initiate streaming at any particle size (see Figure 1.10).

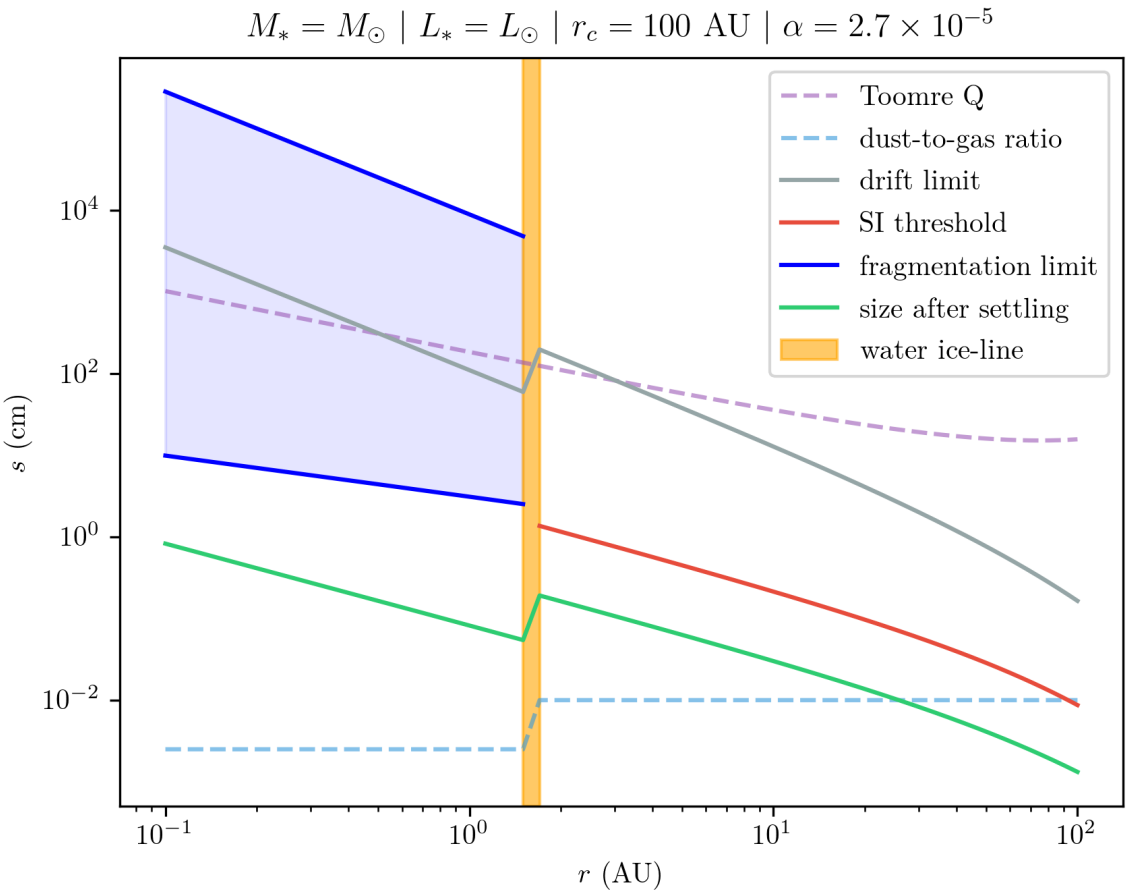


FIGURE 4.2: *Disk B*: a young disk with an ice-line and $\alpha = 2.7 \times 10^{-5}$. The ice-line is indicated with a shaded orange region, inside which the transition between pre- and post-ice-line values occurs.

If there is sufficient turbulence in this disk, a dust particle at $r < r_{\text{ice}}$ can grow beyond the settling size, but it will not undergo streaming and its size will be limited by the fragmentation barrier inside $r_{\text{ice}}$. At $r > r_{\text{ice}}$, the particle can undergo streaming if turbulence is strong enough to bridge the gap between the maximum settling size and

the streaming threshold. Streaming is absent for $r < r_{\rm ice}$ because the dust-to-gas ratio is too low to initiate clumping (Figure 1.10). The size of a dust grain in the outer disk has a maximum value dictated by the drift limit. Disk B is plotted in Figure 4.2.

**(C)** If we take Disk B and set $\alpha = 10^{-3}$ instead, the fragmentation limit reappears in the outer disk. If the dust grain is meeting the fragmentation curve from underneath, it will notice that the limit increases sharply at the ice-line because the ice-rich solids at $r > r_{\rm ice}$ have a higher fragmentation threshold velocity compared to the silicates inside the ice-line.

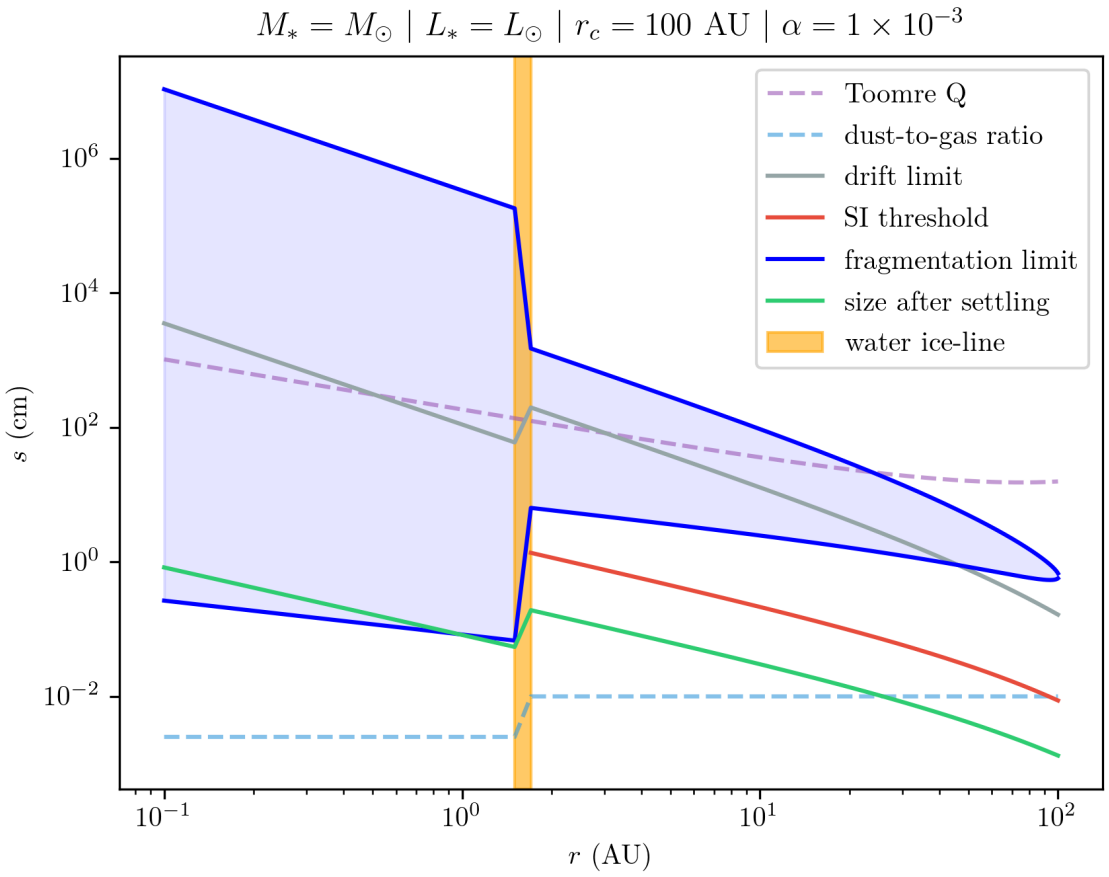


FIGURE 4.3: *Disk C*: a young disk with an ice-line and $\alpha = 1 \times 10^{-3}$. This turbulence is strong enough to fragment icy solids beyond the ice-line.

Planetesimal formation is not possible in the inner disk for the high $\alpha$ used here; grains at $r < r_{\rm ice}$ will not even reach the final size from settling because they will fragment first. In the outer disk, streaming is possible. The size of the dust grains is limited by the fragmentation barrier for $r_{\rm ice} < r < 45$ AU. For 45 AU $< r < r_c$, the maximum size of the grain is set by the drift limit. Disk C is plotted in Figure 4.3.

**(D)** Next, consider a more evolved disk, in which the dust has drifted inwards slightly. We revert the turbulence to $\alpha = 2.7 \times 10^{-5}$ and include a dust surface density enhancement of $e = 1.64$ interior to the ice-line. We note that Birnstiel et al. (2012) find enhancements of at least 40 around and inside the ice-line so this a relatively modest choice. Additionally, $e = 1.64$ is the minimum enhancement that allows the streaming threshold to extend into $r < r_{\rm ice}$. However, fragmentation prevents the SI from starting inside the ice-line and limits the size of the dust grains in the inner disk. In the outer regions of the disk, streaming is possible but once again the maximum dust size is set by the drift limit. Disk D is plotted in Figure 4.4.

**(E)** If we increase the enhancement factor to $e = 2.5$, we can finally get streaming at the ice-line. Any enhancement $e > 2.5$ will lower the radius at which streaming is limited by fragmentation. Disk E is plotted in Figure 4.5.

**(F)** For example, consider an enhancement of $e = 16$. In this case, streaming can occur anywhere in the disk, even for grains that have not yet reached the maximum potential size after settling alone. We will not set $e > 16$ in our model because it sets the dust-to-gas ratio too far outside the domain of Figure 1.10 and therefore extrapolation of $\tau_{SI}$ becomes significantly more unreliable.
Disk F is plotted in Figure 4.6.

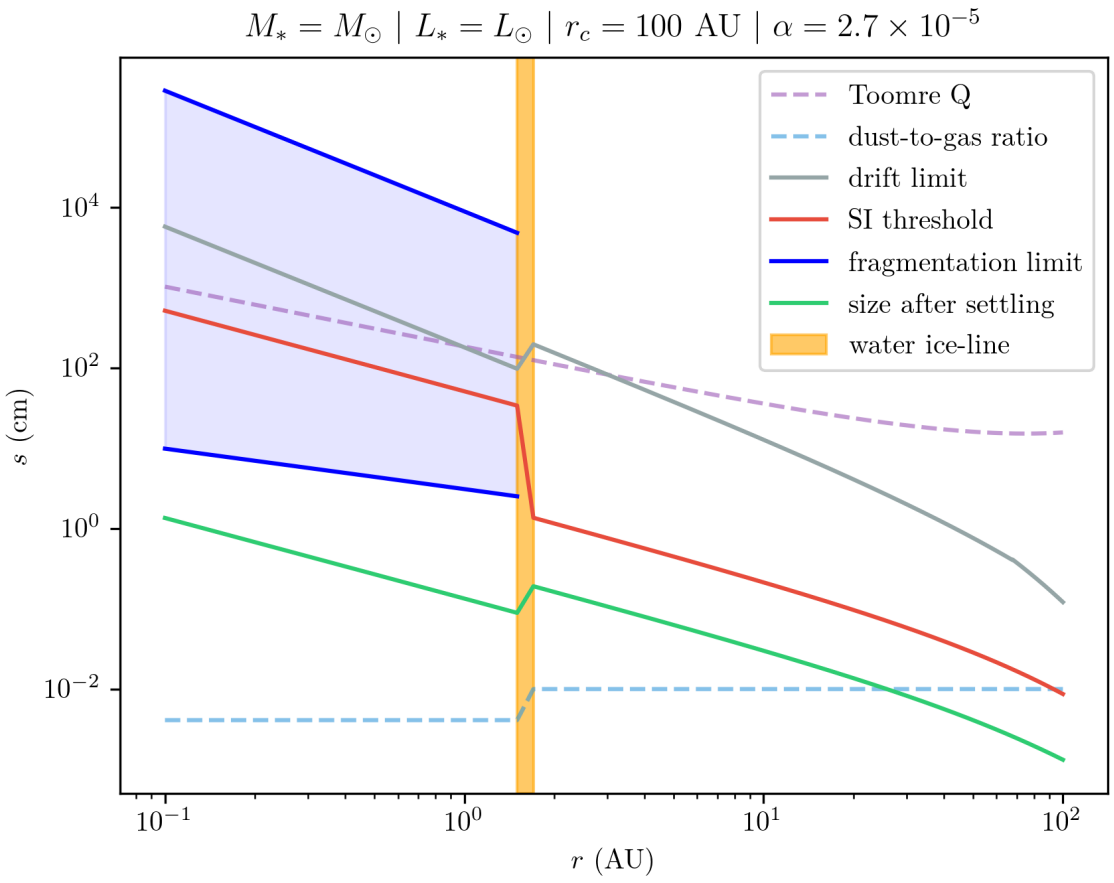


FIGURE 4.4: *Disk D*: an evolved disk with an ice-line and $\alpha = 2.7 \times 10^{-5}$. The dust surface density is enhanced by a factor of 1.64 inside the ice-line

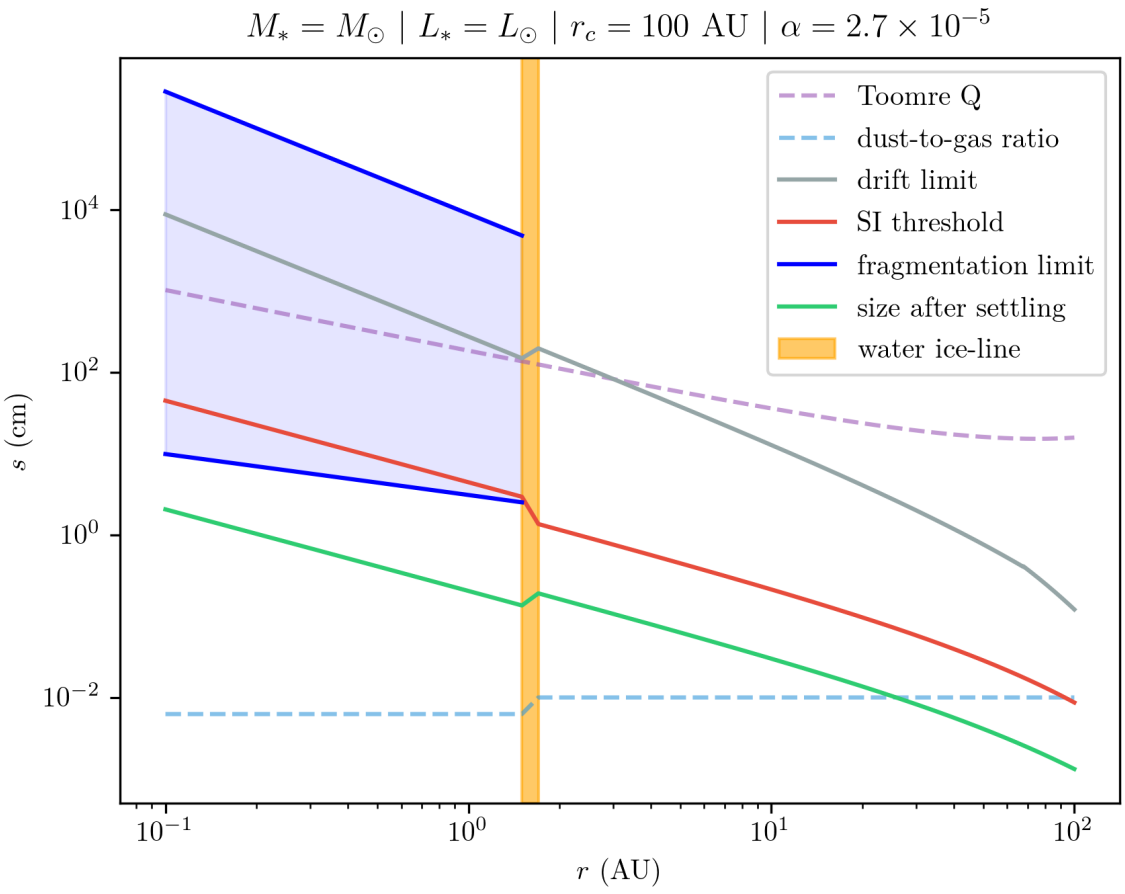


FIGURE 4.5: *Disk E*: an evolved disk with an ice-line and $\alpha = 2.7 \times 10^{-5}$. The dust surface density is enhanced by a factor of 2.5 inside the ice-line

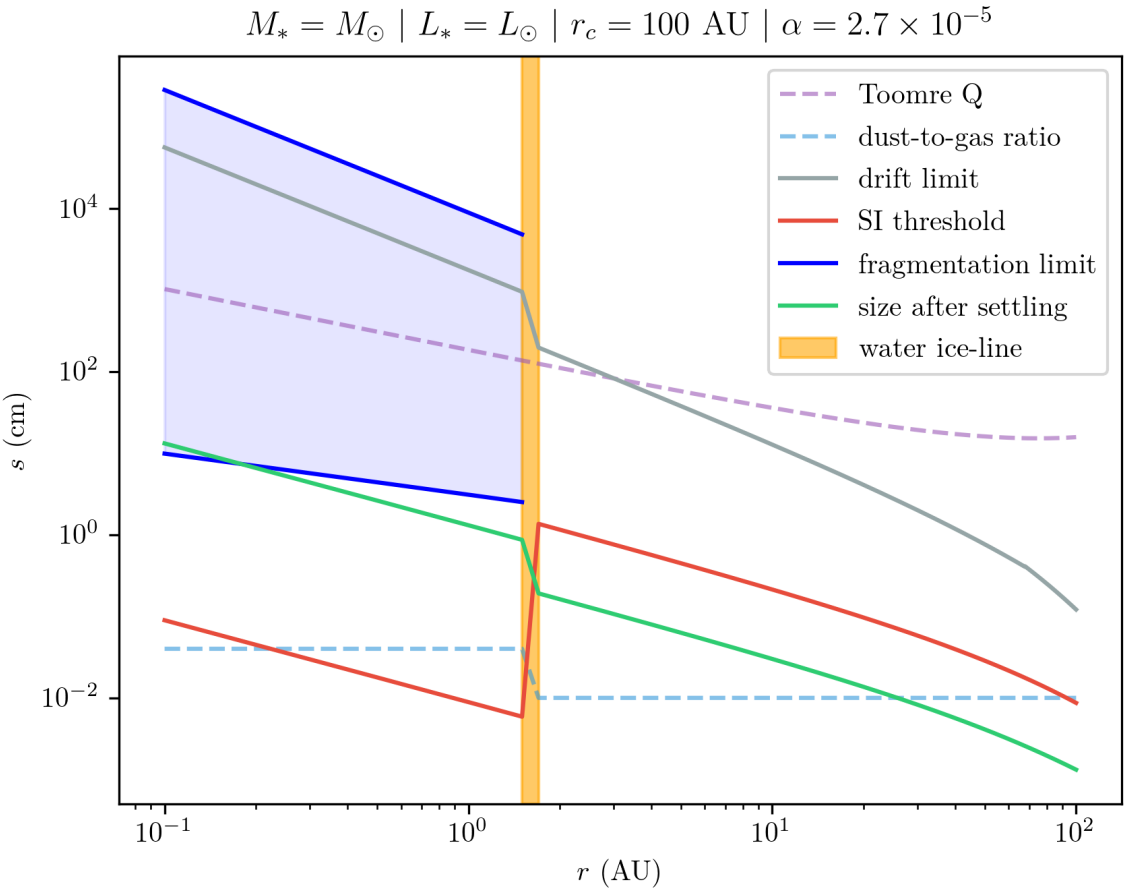


FIGURE 4.6: *Disk F*: an evolved disk with an ice-line and $\alpha = 2.7 \times 10^{-5}$. The dust surface density is enhanced by a factor of 16 inside the ice-line

**(G)** We return to the parameters of Disk E but set the mass of the disk to $M_{\rm disk} = 0.8M_*$. This pushes $Q < 1$ at large radii and $\Sigma_g(0.1\ \text{AU}) \simeq 37\ 000\ \text{gcm}^{-2}$. Although this disk is unstable at large radii, the general shape and locations of the streaming, fragmentation, drift, and settling curves remains the same as in Disk E. 1 is shown as a dotted black line. Disk G is plotted in Figure 4.7.

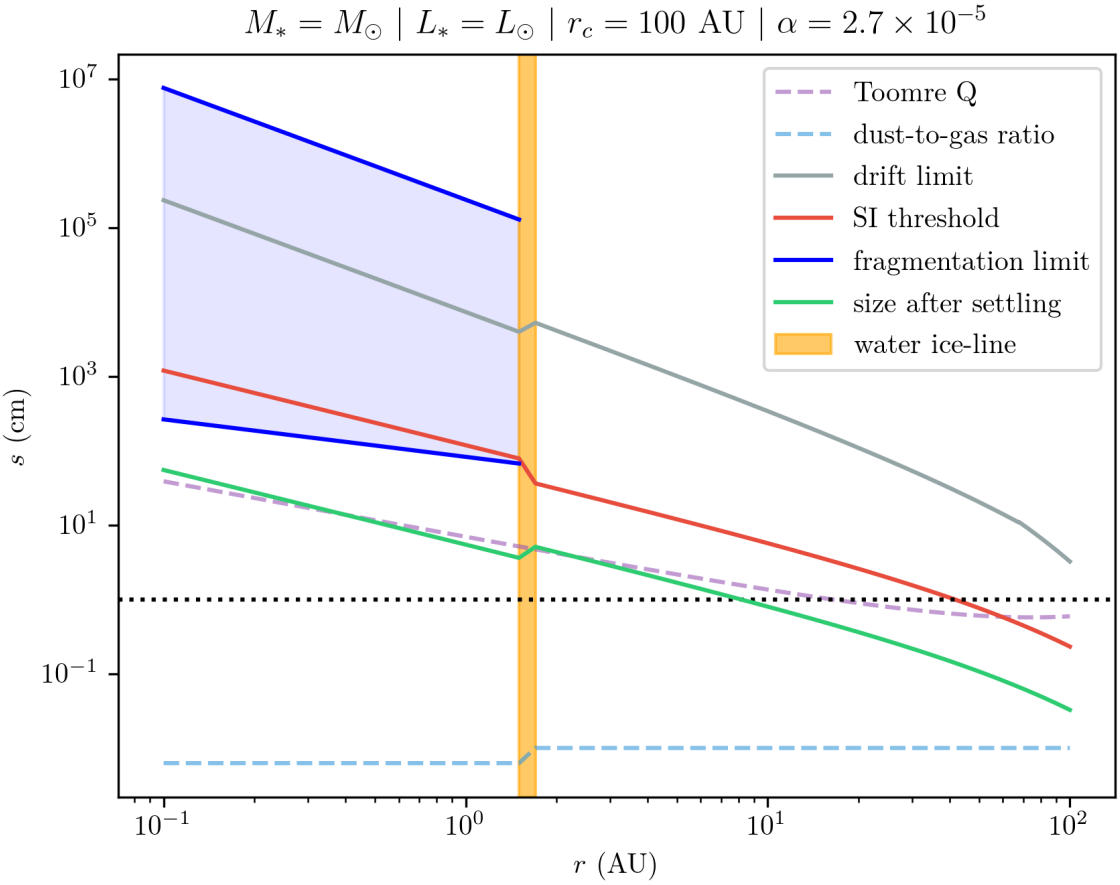


FIGURE 4.7: *Disk G*: an evolved disk with an ice-line and $\alpha = 2.7 \times 10^{-5}$ that is unstable at large radii. Dust enhancement inside the ice-line is a factor of 2.5

**(H)** Consider a star with mass $M_* = 2M_\odot$. The mass-luminosity relationship for main-sequence stars $M_* \propto L_*^{3.5}$ tells us that the luminosity of this star is approximately $L_* = 11L_\odot$. It is important to note that this relation is not completely accurate, especially for pre-main-sequence stars. We will keep all other parameters the same as in Disk E.

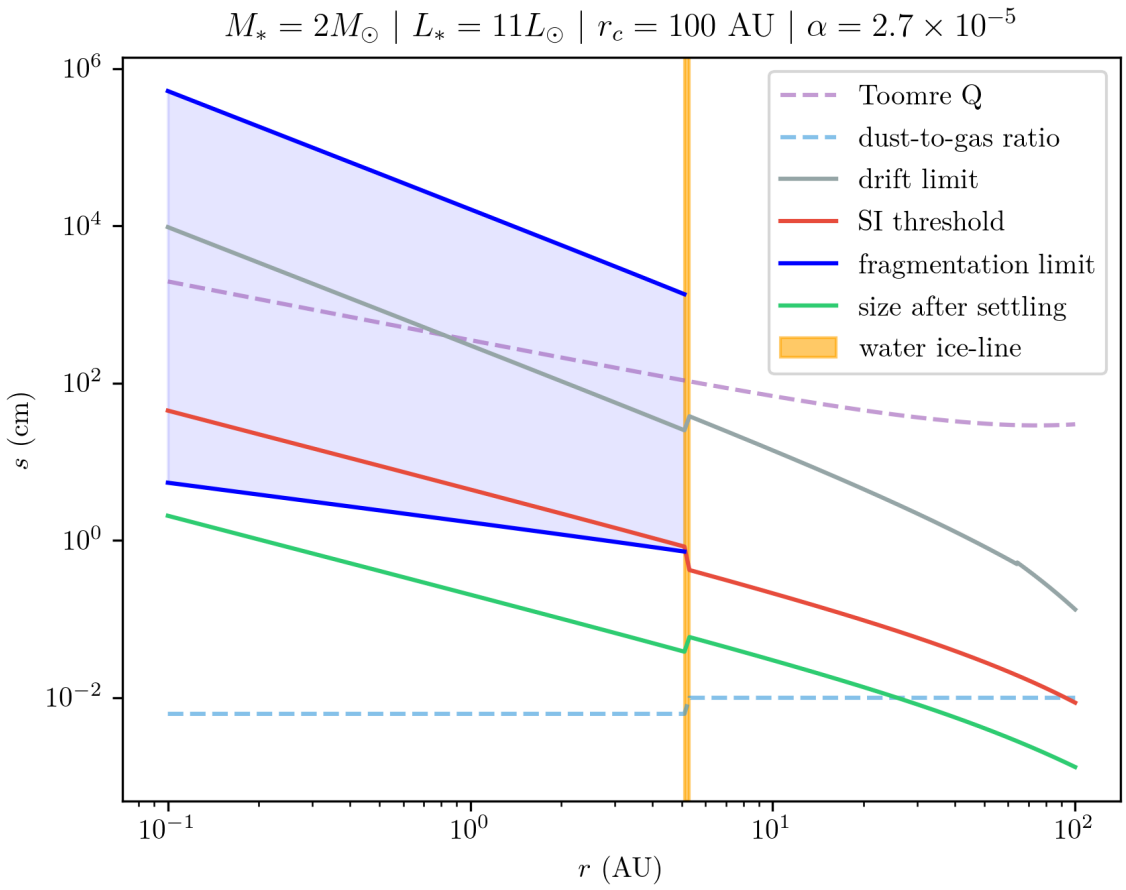


FIGURE 4.8: *Disk H*: an evolved disk with an ice-line and $\alpha = 2.7 \times 10^{-5}$ around a $2M_\odot$ star. The dust surface density is enhanced by a factor of 2.5 inside the ice-line

The location of the ice-line and all of the solid curves shift to the right, but the behaviour of the disk is the same as in Disk E; for example, the radius at which streaming is limited by fragmentation is still at the ice-line. Once again, objects inside this radius are growth limited by the fragmentation barrier without undergoing streaming, and objects outside the ice-line will undergo streaming but their maximum size will be set by the drift limit. Conversely, the ice-line and all the solid curves would move to the left for a smaller star with the same $r_c$. Disk H is plotted in Figure 4.8.

**(I)** Let's return to a solar-type star but increase the maximum size of the gas disk to $r_c = 150$ AU. All other parameters are the same as in Disk E. We get $\Sigma_g(0.1 \text{ AU}) \sim 700$ gcm$^{-2}$ so we do not need to increase $M_{\text{disk}}$. The location of the ice-line is the same as in Disk E, but a smaller percentage of the disk is inside the ice-line. Therefore, more of the disk can participate in streaming. Disk I is plotted in Figure 4.9.

**(J, K, L, M):** Consider now an evolved disk with an ice-line and $e = 5$. We present four disks. Disk J has $\alpha = 2.7 \times 10^{-5}$, and $Z = 0.01$ beyond the ice-line. Disk K has $\alpha = 2.7 \times 10^{-5}$, $Z = 0.02$. Disk L has $\alpha = 1 \times 10^{-3}$, $Z = 0.01$ and Disk M has $\alpha = 1 \times 10^{-3}$, $Z = 0.02$. There is a range of $Z$ for which the fragmentation barrier does not limit streaming at a specific radius $r'$. This range of $Z$ is smaller for high turbulence. On the other hand, if $Z$ is large enough, even high $\alpha$ allows streaming in the inner disk. If $Z$ is very low, weak $\alpha$ will also prohibit streaming in the inner disk.

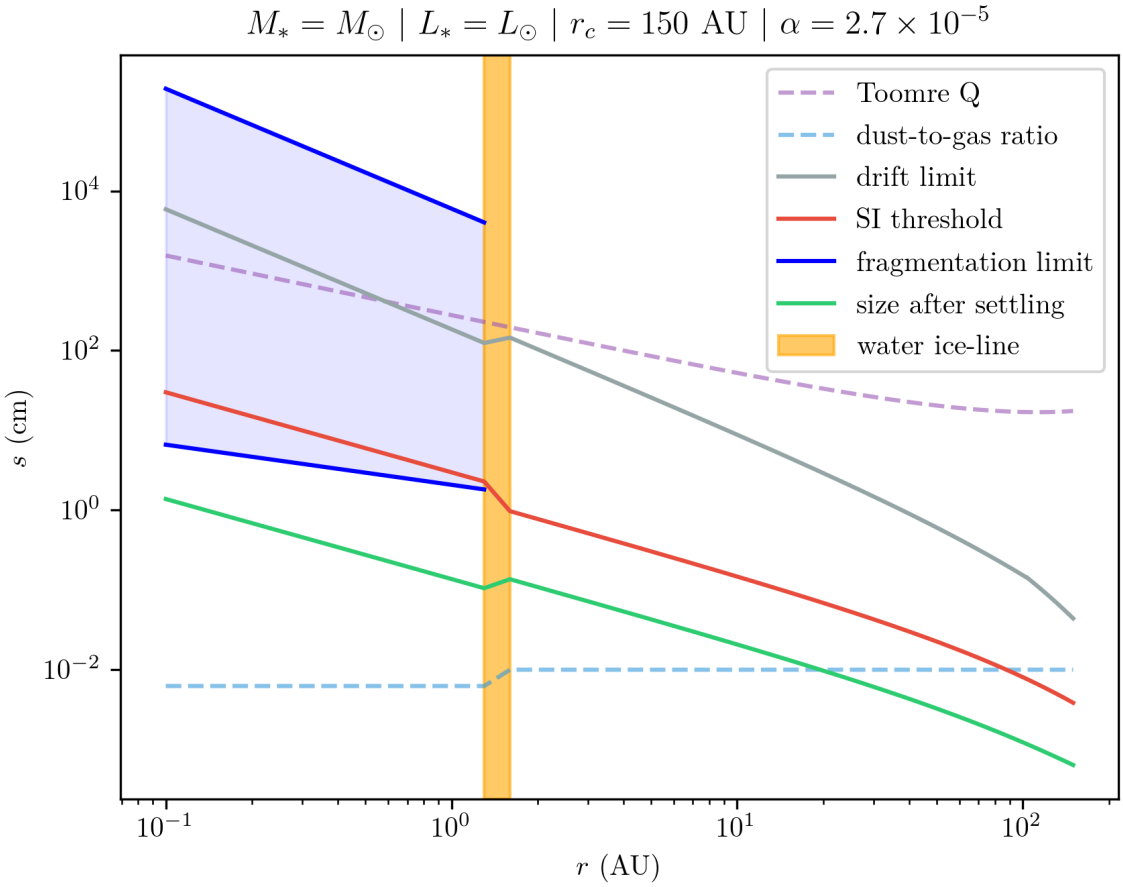


FIGURE 4.9: *Disk I*: an evolved disk with an ice-line and $\alpha = 2.7 \times 10^{-5}$. The dust surface density is enhanced by a factor of 2.5 inside the ice-line, and the maximum disk radius is $r_c = 150$

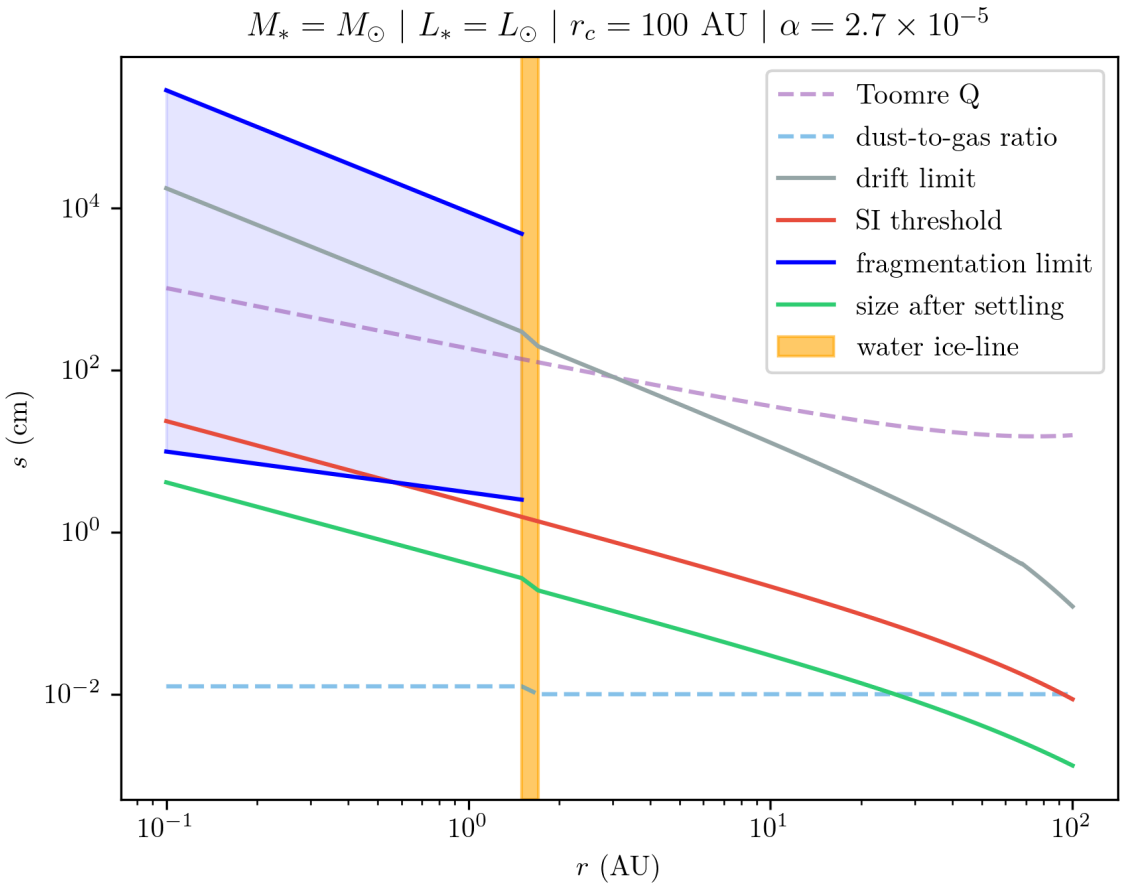


Figure 4.10: *Disk J*: an evolved disk with an ice-line and $\alpha = 2.7 \times 10^{-5}$. The dust surface density is enhanced by a factor of 5 inside the ice-line, and $Z = 0.01$ outside the ice-line

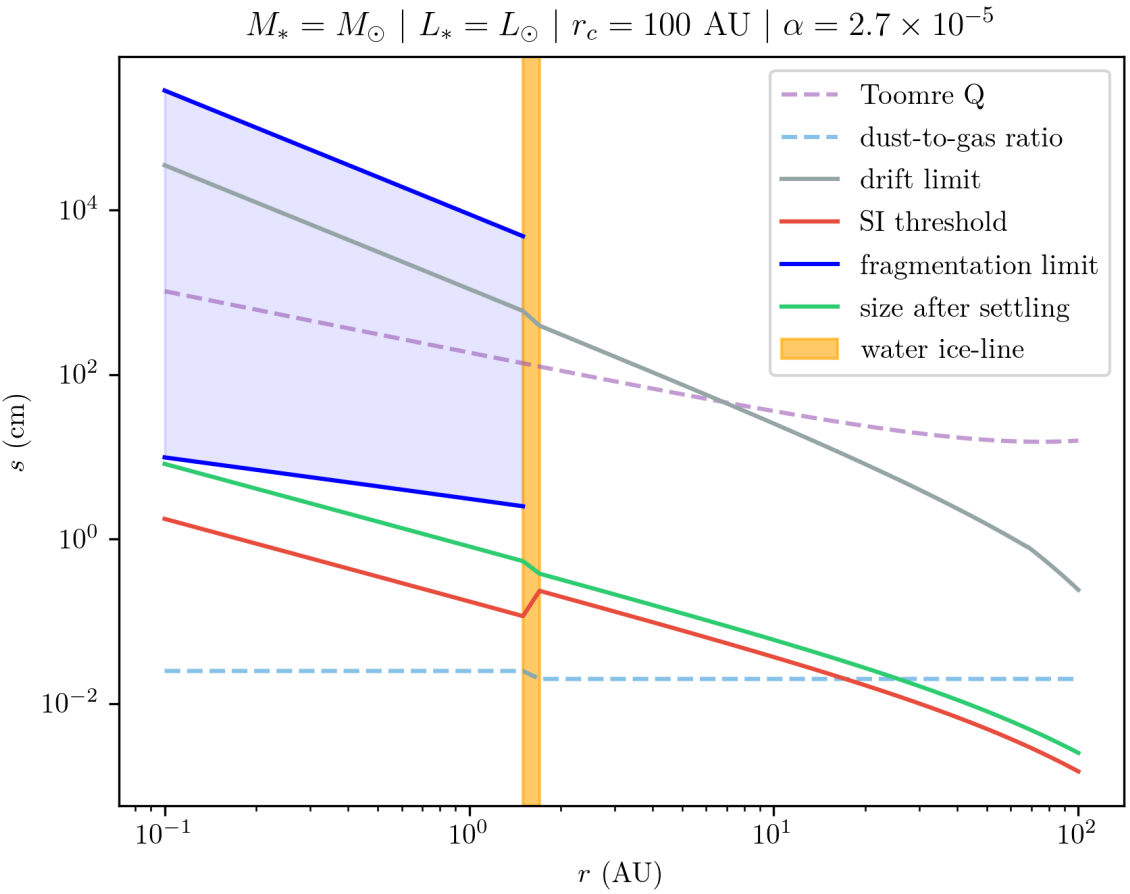


FIGURE 4.11: *Disk K*: an evolved disk with an ice-line and $\alpha = 2.7 \times 10^{-5}$. The dust surface density is enhanced by a factor of 5 inside the ice-line, and $Z = 0.02$ outside the ice-line

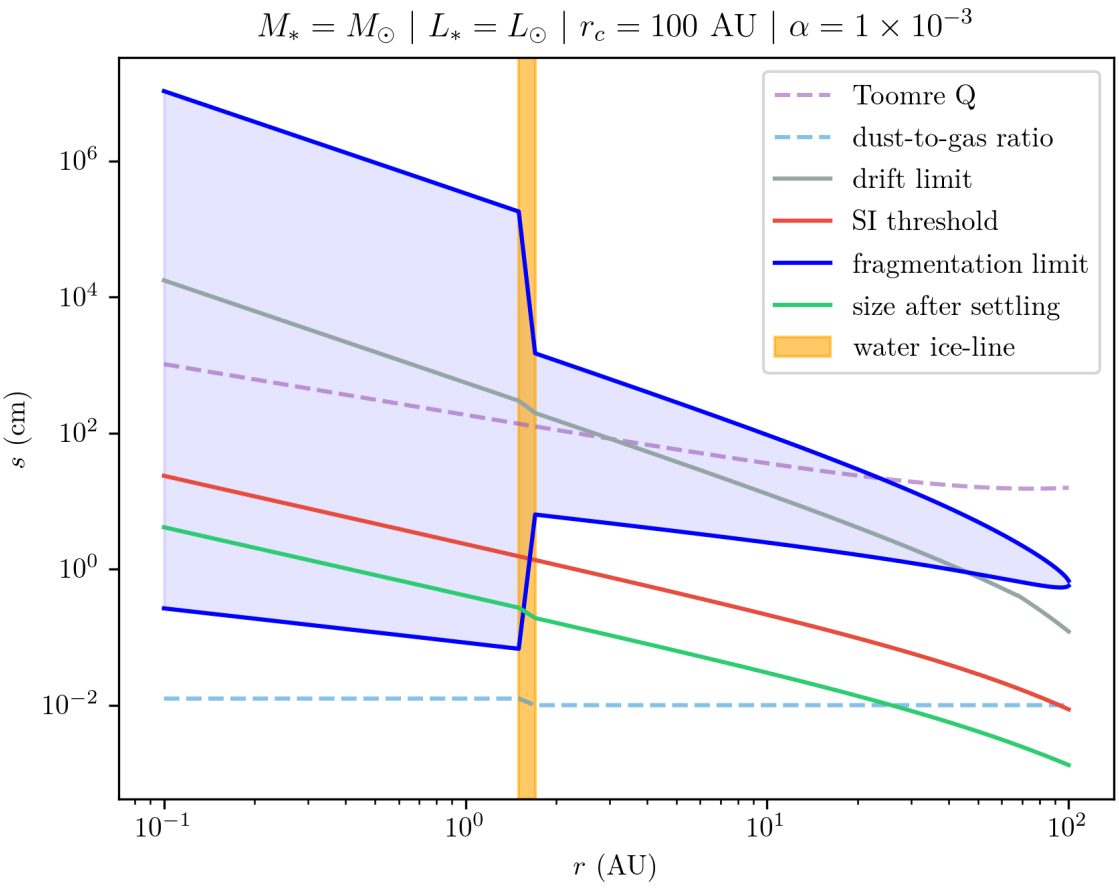


FIGURE 4.12: *Disk L*: an evolved disk with an ice-line and $\alpha = 1 \times 10^{-3}$. The dust surface density is enhanced by a factor of 5 inside the ice-line, and $Z = 0.01$ outside the ice-line

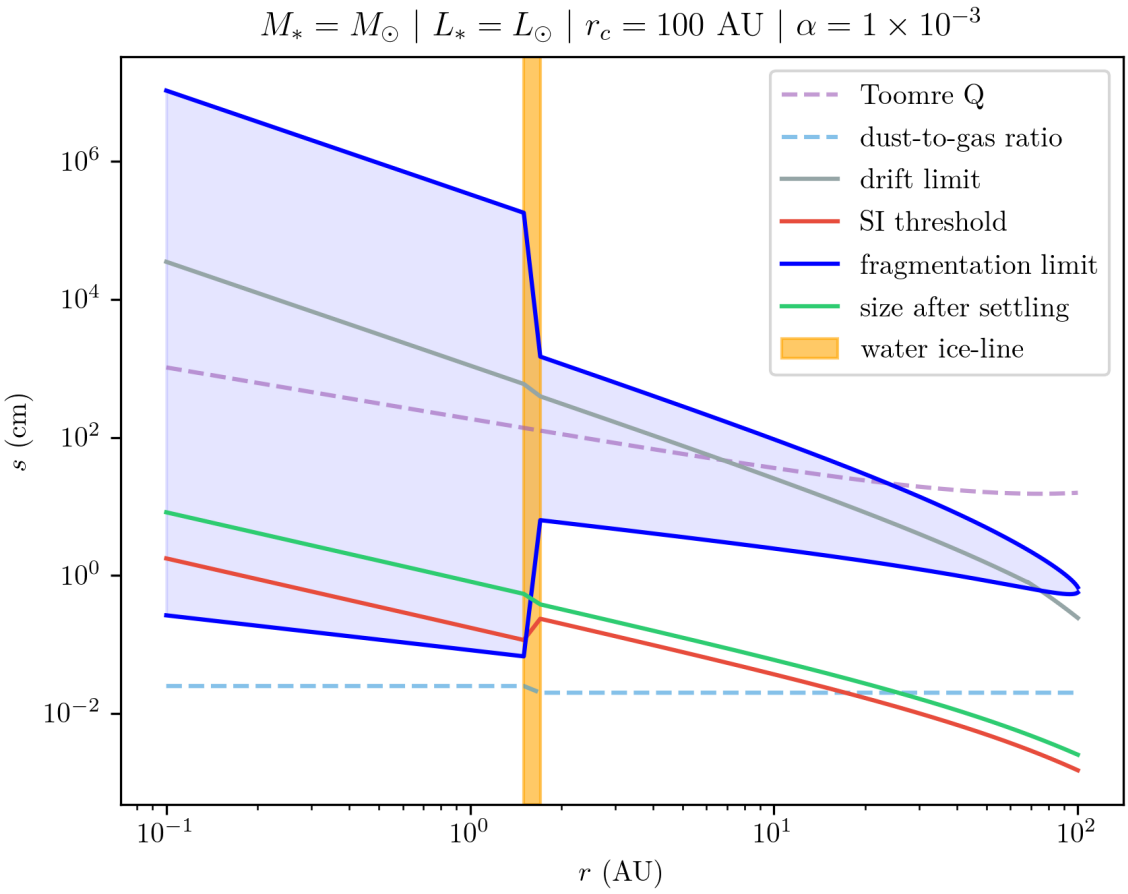


FIGURE 4.13: *Disk M*: an evolved disk with an ice-line and $\alpha = 1 \times 10^{-3}$. The dust surface density is enhanced by a factor of 5 inside the ice-line, and $Z = 0.02$ outside the ice-line

## 4.3 Effects of Parameter Variation

On many of the plots in the previous section, there is a gap between the final size a dust grain reaches after settling and the minimum size required to trigger the SI. In theory, this gap can be closed in the presence of Kelvin-Helmholtz driven turbulence (characterized by $\alpha$) which encourages particles to continue growth via collisions after they have settled to the mid-plane. In principle, drift could also prevent a dust grain from bridging this gap, but in practice the drift time is too long to cut off growth. The value of $\alpha$ is also important to the placement of the fragmentation size barrier (equation 4.5). A high value of $\alpha$ can facilitate growth through turbulent mixing.

The turbulence also has a more unexpected consequence on growth. Figure 4.14 compares the value of $\alpha$ extracted from our `tau-2N120` shearing box to the observational upper limit $10^{-3}$. The simulation value of $2.7 \times 10^{-5}$ is just under two orders of magnitude smaller than this limit, which significantly lowers the rate of collision and slows down the growth rate. The weaker turbulence is never strong enough to fragment icy solids, which are commonly assumed to have $v_{\text{frag}} = 10$ m/s so there is essentially no fragmentation limit beyond the ice-line (for example, see Figure 4.8. Both values of $\alpha$ are strong enough to fragment silicates in the inner solar system ($v_{\text{frag}} = 1$ m/s).

There are many ice-lines for different compounds (ie $CO/CO_2$, methane, ammonia, nitrogen...). As the disk gets colder, more materials can solidify and become available to participate in particle collisions. More material allows planets to grow their cores more rapidly and to a larger final size. Eventually, they can become large enough to hold on to a significant gaseous atmosphere (gas giants). Since the composition of a solid object also affects its fragmentation threshold velocity, the inner solar system – which contains mostly silicates, refractories, and iron-like metals – is a much harsher

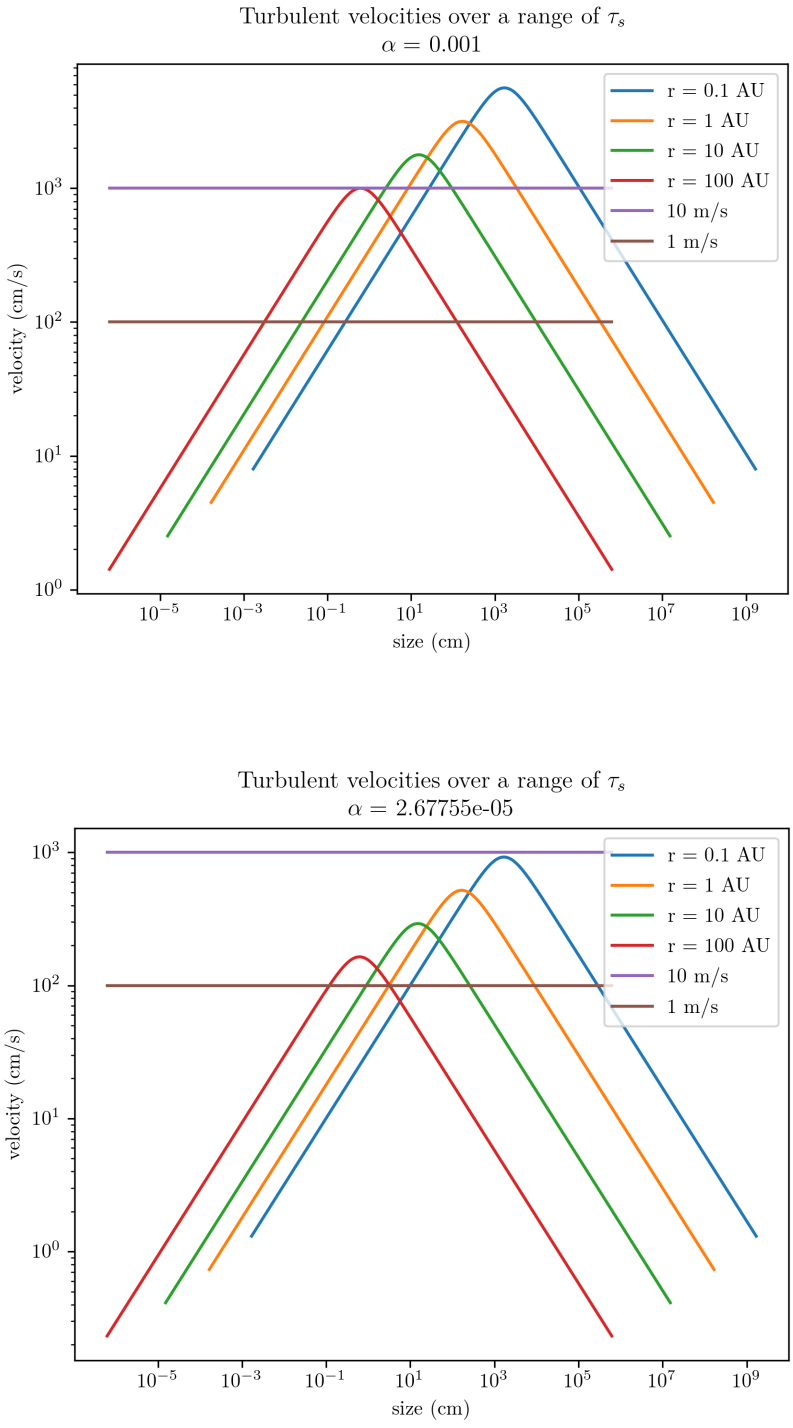


FIGURE 4.14: In disks characterized by a weak $\alpha$ like the one extracted from our 3D shearing box simulation (bottom panel), turbulent velocity can not collide icy solids fast enough to destroy them; this can greatly reduce or eliminate the fragmentation barrier past the ice-line.

environment for particle growth when compared to the outer solar system which also has water ice. Since water is such a large component of our solar system, it is the primary ice-forming compound to consider when studying how ice-lines affect planet formation.

A low value of the fragmentation threshold velocity $v_{\text{frag}}$ makes it more likely for particles to break apart during fragmentation, which can be destructive to collisional growth. A discontinuity in $v_{\text{frag}}$ at the ice-line will result in a discontinuity in the fragmentation size limit $a_{\text{frag}}$ (equation 4.7).

The local dust-to-gas ratio is very important. Slightly super-solar $Z$ is required to kick start SI (see last page of Section 2.4). Additionally, $Z$ sets the streaming instability threshold size $\tau_{SI}$ according to Figure 1.10. Finally, the drift size limit is linearly proportional to $Z$ (equation 4.5). Similarly, the same arguments apply to $e$, which is just a modification to $Z$ in evolved disks at radii interior to the ice-line. Increasing the intrinsic density of individual dust grains $\rho_m$ will lower $a_{\text{frag}}$, $a_{\text{drift}}$, $a_{\text{settle}}$, and $a_{\text{SI}}$ by the same amount. However, the minimum disk radius for streaming will not change.

Changing the mass of the star, luminosity of the star, or maximum size of the disk moves the ice-line, modifies the proportion of the disk inside the ice-line, the minimum radius where streaming can occur, and the extent of the disk limited by the fragmentation barrier as opposed to the drift limit. These changes do not, however, modify the relationship between these curves as they all move together. The general behaviour of the disk will therefore not change if we modify these quantities.

If we want to build a solar system with rocky planets close to the star and gas giants further away, we need to start with a young disk containing a water ice-line like Disk B in Figure 4.2. A disk with too much turbulence can prevent grains in the inner

disk from even reaching the settling size – see Disk C in Figure 4.3. Therefore, nature seems to require $\alpha \ll 10^{-3}$.

Streaming is not possible in the inner regions of Disk B, so for now only planets beyond the ice-line will experience significant growth. This suggests that planets beyond the ice-line (or their rocky cores) are first to develop. At later times, the size of the dust disk shrinks due to radial drift. Some dust is lost into the star, but other particles pile up at the ice-line and inside it (Birnstiel et al. 2010). A minimum enhancement of $\sim 2.5\times$ the initial dust-to-gas ratio is required interior to the ice-line in order for streaming to be possible everywhere in this region. If we meet these conditions, we can form rocky planets in the inner solar system. The growth time of a dust grain is $t_{\rm grow} = (Z_0\Omega)^{-1}$, which is much shorter than a million years (Birnstiel et al. 2016). Planetesimal formation will not be limited by the lifetime of the disk.

# Chapter 5

# Conclusions

In this thesis we have explored a new regime of planetesimal formation in the low turbulence, small grain limit. Recent observational studies have suggested that the turbulence in protoplanetary disks is characterized by $\alpha < 10^{-3}$ so this is an important limit to consider (Flaherty et al. 2020).

The previously leading hypothesis concerning the origins of disk turbulence was that it is a result of the magnetorotational instability (MRI). However, evidence shows that only the inner most region of the disk mid-plane $r < 0.1$ AU is ionized enough for the MRI to be strong. In a "dead zone" that can extend from 0.1 AU up to 65 AU, magnetic interactions can only occur via non-ideal magnetohydrodynamics (MHD). Some numerical simulations suggest that the MRI effectively does not operate in the dead zone, and this is supported by observational evidence (Bai and Stone 2013; Cleeves et al. 2015). Since grain growth (and thus planet formation) will stall without turbulence, this suggests that there must be another source of turbulence in this section of the disk that coincides with the location of planet formation. Importantly, the MRI may become significant again for $r > 65$ AU and large scale heights (Turner and Drake 2009). In this work, we present simulations that are located in the dead

zone between these regions of MRI-type turbulence. We assumed no external sources of turbulence, including MRI active upper layers. However, turbulence from the upper layers may penetrate into the inner disk slightly, creating larger values of $\alpha$.

Other possible sources of turbulence in protoplanetary disks are hydrodynamic instabilities like the vertical shear instability (VSI), convective overstability, and the zombie vortex instability. These have been suggested as alternatives in the MRI dead zone (Lyra and Umurhan 2019). In this work, we explored the Kelvin-Helmholtz instability (KHI), which is a type of VSI arising from a difference in speed between the gas in a disk and the dusty mid-plane. We simulated the KHI in the ATHENA hydrodynamic grid-code using a shearing box approximation with shear-periodic boundary conditions that allowed us to zoom into a small section of the disk. This local approximation helps us better resolve the dynamics at small scales. The grain sizes in our simulations $\tau_s = 0.01 - 0.001$ were too small to undergo streaming, so we focused on resolving the scale height $H_g$ which is a characteristic length in a turbulent, finite width fluid.

The value for $\alpha$ was extracted directly from each shearing box and we found that all of the runs had $\alpha \ll 10^{-3}$. Additionally, the magnitude of $\alpha$ increased with resolution and approached $\alpha \sim 2.7 \sim 10^{-5}$ in the high resolution limit. So higher resolution runs resulted in greater turbulence. This is because the increase in resolution corresponds to a smaller numerical dissipation length, which allows more turbulence to be generated. However, the changes became small as the dust layer became well resolved and we anticipate that $\alpha$ is unlikely to increase much beyond $3 \times 10^{-5}$. Similarly, we converge at a final $H_d \sim 0.017 H_g$ at infinite resolution after settling in disks with grains characterized by either $\tau_s = 0.01$ or $\tau_s = 0.001$. The increased turbulence in high resolution simulations was able to thicken the dust scale height more than their

low resolution counterparts.

We applied an extracted $\alpha = 2.7 \times 10^{-5}$ to a semi-analytic disk model. In order to account for MRI turbulence in the upper layers or other possible sources of turbulence affecting the mid-plane, we compared our extracted value against the observational upper limit of $\alpha = 10^{-3}$. We found that turbulence corresponding to $\alpha > 10^{-3}$ is not necessary for planet formation. In fact, low turbulence is more conducive to planet formation in the inner solar system (interior to the water ice-line) because the size at which a dust grain fragments upon collision is higher for lower $\alpha$. Lower $\alpha$ can remove the fragmentation barrier in the outer disk entirely if it cannot move grains fast enough to reach the higher fragmentation threshold velocities beyond the ice-line.

Even for high $\alpha$, the increase in fragmentation threshold velocity at the ice-line raises the fragmentation size limit in the outer disk compared to its value in the inner solar system. The implications of this is that planets in the outer solar system (gas giants) are formed first. The formation of gas giants may create ring structures in the disk that result in local pressure maxima which can relieve issues of radial drift in the inner solar system. Once the disk is allowed to evolve, a pile up of dust at $r \leq r_{\rm ice}$ can raise the dust-to-gas ratio in this region enough that inner solar system planets can begin to form.

## 5.1 Future Work

A major limitation of shearing box simulations like the ones presented in this thesis is that they cannot resolve length scales that are comparable to the size of planetesimals, nor do they include global disk properties. Furthermore, they would be improved by incorporation of a grain growth model to simulate the growth rates of dust in real

disks. The addition of disk winds to these simulations would also help us understand how winds mitigate the effects of turbulence and how this might impact planetesimal formation. An ideal simulation would incorporate all of these effects at high resolution, but would be computationally impossible with current codes. Some form of adaptivity (like adaptive mesh refinement) may allow such work, but current methods rely on the fluid limit and would not work for larger grains where $\tau_s \sim 1$.

Next steps could include an examination of how turbulence originating from a KHI can be conducive to the growth of dust. Particularly, it would be good to quantify how large $\alpha$ needs to be to bridge the gap between the settling and streaming curves in Chapter 4. A weak $\alpha$ will not be able to drive this post-settling growth via turbulent mixing. If $\alpha$ is very small, it may mean that growth takes over a million years, in which case we begin to reach the time constraint set by the removal of disk gas by solar wind. It would also be good to examine how $\alpha$ depends on the set-up of the disk, particularly the pressure gradient profile. If the pressure gradient changes over time, so will the value of $\alpha$ in the disk. If this is the case, we may be able to form planets at different times.

We need to further study the thresholds for streaming in 3D simulations, such as in recent work by Rucska (2022). This will help us better understand where and when planets can form in the disk. Including a model for grain growth in these simulations might move the threshold to lower dust-to-gas ratios $Z$, since grains that are allowed to evolve will reach cm sizes quicker for a given $Z$. The threshold may also be lowered if multiple grain sizes are included, as collisions between particles of different size are less likely to result in fragmentation. Once again, this allows grains to reach cm sizes more quickly.

We also need to better understand the impact of large scale radial drift. A high resolution box that incorporates global disk properties will help us do this, in contrast to the local shearing box approximations used in this thesis. Recent work by Carrera and Simon (2022) is a first step in learning about possible global disk effects that we may be missing. A hybrid approach would be to conduct a low resolution global simulation and identify snapshots of interest for further investigation with a shearing box: the low resolution run can be periodically checked for SI, perhaps by examining the critical conditions for streaming discussed in Rucska (2022). If streaming is expected to occur, it would be possible to zoom into the global simulation with a high resolution shearing box that is capable of simulating streaming. Since the duration of the SI is short, only a small number of snapshots would need to be resolved in the local approximation. However, grain growth, radial drift, and turbulence continue in the background even when streaming is not present and will complicate any methods used to anticipate or detect the SI. Research like this thesis can help characterize these small scale processes and contribute to the development of a subgrid model for background dynamics in a low resolution global disk simulation.

# Bibliography

Akeson, R., Chen, X., Ciardi, D., Crane, M., Good, J., Harbut, M., Jackson, E., Kane, S., Laity, A., Leifer, S., et al. (2013). The NASA exoplanet archive: data and tools for exoplanet research. *Publications of the Astronomical Society of the Pacific* 125(930), 989.

Almgren, A. S., Bell, J. B., Rendleman, C. A., and Zingale, M. (2006). Low Mach number modeling of type Ia supernovae. I. Hydrodynamics. *The Astrophysical Journal* 637(2), 922.

Andrews, S. M., Huang, J., Pérez, L. M., Isella, A., Dullemond, C. P., Kurtovic, N. T., Guzmán, V. V., Carpenter, J. M., Wilner, D. J., Zhang, S., et al. (2018). The disk substructures at high angular resolution project (DSHARP). I. Motivation, sample, calibration, and overview. *The Astrophysical Journal Letters* 869(2), L41.

Andrews, S. M., Wilner, D. J., Zhu, Z., Birnstiel, T., Carpenter, J. M., Pérez, L. M., Bai, X.-N., Öberg, K. I., Hughes, A. M., Isella, A., et al. (2016). Ringed substructure and a gap at 1 au in the nearest protoplanetary disk. *The Astrophysical Journal Letters* 820(2), L40.

Andrews, S. M., Wilner, D., Hughes, A., Qi, C., and Dullemond, C. (2009). Protoplanetary disk structures in Ophiuchus. *The Astrophysical Journal* 700(2), 1502.

Ansdell, M., Williams, J., Trapman, L., Terwisga, S. van, Facchini, S., Manara, C., Marel, N. van der, Miotello, A., Tazzari, M., Hogerheijde, M., et al. (2018). ALMA survey of Lupus protoplanetary disks. II. Gas disk radii. *The Astrophysical Journal* 859(1), 21.

Ansdell, M., Williams, J. P., Marel, N. van der, Carpenter, J. M., Guidi, G., Hogerheijde, M., Mathews, G. S., Manara, C. F., Miotello, A., Natta, A., et al. (2016). ALMA survey of lupus protoplanetary disks. I. Dust and gas masses. *The Astrophysical Journal* 828(1), 46.

Armitage, P. J. (2020). *Astrophysics of planet formation*. Cambridge University Press.

Ayliffe, B. A. and Bate, M. R. (2012). The growth and hydrodynamic collapse of a protoplanet envelope. *Monthly Notices of the Royal Astronomical Society* 427(3), 2597–2612.

Bai, X.-N. and Stone, J. M. (2010a). Dynamics of solids in the midplane of protoplanetary disks: Implications for planetesimal formation. *The Astrophysical Journal* 722(2), 1437.

Bai, X.-N. and Stone, J. M. (2010b). Particle-Gas Dynamics with Athena: Method and Convergence. *The Astrophysical Journal Supplement Series* 190(2), 297.

Bai, X.-N. and Stone, J. M. (2013). Local study of accretion disks with a strong vertical magnetic field: Magnetorotational instability and disk outflow. *The Astrophysical Journal* 767(1), 30.

Balbus, S. A. and Hawley, J. F. (1991). A powerful local shear instability in weakly magnetized disks. I-Linear analysis. II-Nonlinear evolution. *The Astrophysical Journal* 376, 214–233.

Bate, M. R. (2018). On the diversity and statistical properties of protostellar discs. *Monthly Notices of the Royal Astronomical Society* 475(4), 5618–5658.

Birnstiel, T., Dullemond, C., and Brauer, F. (2010). Gas-and dust evolution in protoplanetary disks. *Astronomy & Astrophysics* 513, A79.

Birnstiel, T., Fang, M., and Johansen, A. (2016). Dust evolution and the formation of planetesimals. *Space Science Reviews* 205(1), 41–75.

Birnstiel, T., Klahr, H., and Ercolano, B. (2012). A simple model for the evolution of the dust population in protoplanetary disks. *Astronomy & Astrophysics* 539, A148.

Bitsch, B., Johansen, A., Lambrechts, M., and Morbidelli, A. (2015). The structure of protoplanetary discs around evolving young stars. *Astronomy & Astrophysics* 575, A28.

Blum, J. and Wurm, G. (2008). The growth mechanisms of macroscopic bodies in protoplanetary disks. *Annu. Rev. Astron. Astrophys.* 46, 21–56.

Bohlin, R. C., Savage, B. D., and Drake, J. (1978). A survey of interstellar HI from L-alpha absorption measurements. II. *The Astrophysical Journal* 224, 132–142.

Brauer, F., Dullemond, C., and Henning, T. (2008). Coagulation, fragmentation and radial motion of solid particles in protoplanetary disks. *Astronomy & Astrophysics* 480(3), 859–877.

Carrera, D., Johansen, A., and Davies, M. B. (2015). How to form planetesimals from mm-sized chondrules and chondrule aggregates. *Astronomy & Astrophysics* 579, A43.

Carrera, D. and Simon, J. B. (2022). The Streaming Instability Cannot Form Planetesimals from Millimeter-size Grains in Pressure Bumps. *The Astrophysical Journal Letters* 933(1), L10.

Carrera, D., Simon, J. B., Li, R., Kretke, K. A., and Klahr, H. (2021). Protoplanetary disk rings as sites for planetesimal formation. *The Astronomical Journal* 161(2), 96.

Chandrasekhar, S. (1961). *Hydrodynamic and Hydromagnetic Stability*.

Chiang, E. and Youdin, A. (2010). Forming Planetesimals in Solar and Extrasolar Nebulae. *Annual Review of Earth and Planetary Sciences* 38(1), 493–522.

Cleeves, L. I., Bergin, E. A., Qi, C., Adams, F. C., and Öberg, K. I. (2015). Constraining the X-ray and cosmic-ray ionization chemistry of the TW Hya protoplanetary disk: evidence for a sub-interstellar cosmic-ray rate. *The Astrophysical Journal* 799(2), 204.

Colella, P. (1990). Multidimensional upwind methods for hyperbolic conservation laws. *Journal of Computational Physics* 87(1), 171–200.

Cuzzi, J. N., Dobrovolskis, A. R., and Champney, J. M. (1993). Particle-gas dynamics in the midplane of a protoplanetary nebula. *Icarus* 106(1), 102–134.

Cuzzi, J. N., Hogan, R. C., Paque, J. M., and Dobrovolskis, A. R. (2001). Size-selective concentration of chondrules and other small particles in protoplanetary nebula turbulence. *The Astrophysical Journal* 546(1), 496.

Drążkowska, J., Stammler, S. M., and Birnstiel, T. (2021). How dust fragmentation may be beneficial to planetary growth by pebble accretion. *Astronomy & Astrophysics* 647, A15.

Drążkowska, J., Windmark, F., and Dullemond, C. (2013). Planetesimal formation via sweep-up growth at the inner edge of dead zones. *Astronomy & Astrophysics* 556, A37.

Dullemond, C. P. and Dominik, C. (2005). Dust coagulation in protoplanetary disks: A rapid depletion of small grains. *Astronomy & Astrophysics* 434(3), 971–986.

Epstein, P. S. (1924). On the resistance experienced by spheres in their motion through gases. *Physical Review* 23(6), 710.

Flaherty, K., Hughes, A. M., Simon, J. B., Qi, C., Bai, X.-N., Bulatek, A., Andrews, S. M., Wilner, D. J., and Kóspál, Á. (2020). Measuring turbulent motion in planet-forming disks with ALMA: A Detection around DM tau and nondetections around MWC 480 and V4046 Sgr. *The Astrophysical Journal* 895(2), 109.

Flaherty, K. M., Hughes, A. M., Rosenfeld, K. A., Andrews, S. M., Chiang, E., Simon, J. B., Kerzner, S., and Wilner, D. J. (2015). Weak turbulence in the HD 163296 protoplanetary disk revealed by ALMA CO observations. *The Astrophysical Journal* 813(2), 99.

Flaherty, K. M., Hughes, A. M., Teague, R., Simon, J. B., Andrews, S. M., and Wilner, D. J. (2018). Turbulence in the TW Hya disk. *The Astrophysical Journal* 856(2), 117.

Gammie, C. F. (2001). Nonlinear outcome of gravitational instability in cooling, gaseous disks. *The Astrophysical Journal* 553(1), 174.

Gerbig, K., Murray-Clay, R. A., Klahr, H., and Baehr, H. (2020). Requirements for Gravitational Collapse in Planetesimal Formation—The Impact of Scales Set by Kelvin-Helmholtz and Nonlinear Streaming Instability. *The Astrophysical Journal* 895(2), 91.

Goldreich, P. and Lynden-Bell, D. (1965). II. Spiral arms as sheared gravitational instabilities. *Monthly Notices of the Royal Astronomical Society* 130(2), 125–158.

Goldreich, P. and Ward, W. R. (1973). The formation of planetesimals. *The Astrophysical Journal* 183, 1051–1062.

Gole, D. A., Simon, J. B., Li, R., Youdin, A. N., and Armitage, P. J. (2020). Turbulence regulates the rate of planetesimal formation via gravitational collapse. *The Astrophysical Journal* 904(2), 132.

Gómez, G. C. and Ostriker, E. C. (2005). The effect of the Coriolis force on Kelvin-Helmholtz-driven mixing in protoplanetary disks. *The Astrophysical Journal* 630(2), 1093.

Gong, M., Ivlev, A. V., Akimkin, V., and Caselli, P. (2021). Impact of Magnetorotational Instability on Grain Growth in Protoplanetary Disks. II. Increased Grain Collisional Velocities. *The Astrophysical Journal* 917(2), 82.

Gonzalez, J.-F., Laibe, G., and Maddison, S. T. (2017). Self-induced dust traps: overcoming planet formation barriers. *Monthly Notices of the Royal Astronomical Society* 467(2), 1984–1996.

Guilloteau, S., Dutrey, A., Wakelam, V., Hersant, F., Semenov, D., Chapillon, E., Henning, T., and Piétu, V. (2012). Chemistry in disks-VIII. The CS molecule as an analytic tracer of turbulence in disks. *Astronomy & Astrophysics* 548, A70.

Gundlach, B. and Blum, J. (2014). The stickiness of micrometer-sized water-ice particles. *The Astrophysical Journal* 798(1), 34.

Hartmann, L., Calvet, N., Gullbring, E., and D'Alessio, P. (1998). Accretion and the evolution of T Tauri disks. *The Astrophysical Journal* 495(1), 385.

Hasegawa, Y. and Pudritz, R. E. (2011). The origin of planetary system architectures–I. Multiple planet traps in gaseous discs. *Monthly Notices of the Royal Astronomical Society* 417(2), 1236–1259.

Hawley, J. F., Gammie, C. F., and Balbus, S. A. (1995). Local three-dimensional magnetohydrodynamic simulations of accretion disks. *The Astrophysical Journal* 440, 742.

Hayashi, C. (1981). Structure of the solar nebula, growth and decay of magnetic fields and effects of magnetic and turbulent viscosities on the nebula. *Progress of Theoretical Physics Supplement* 70, 35–53.

Hueso, R. and Guillot, T. (2005). Evolution of protoplanetary disks: constraints from DM Tauri and GM Aurigae. *Astronomy & Astrophysics* 442(2), 703–725.

Incropera, F. P., DeWitt, D. P., Bergman, T. L., Lavine, A. S., et al. (1996). *Fundamentals of heat and mass transfer*. Vol. 6. Wiley New York.

Jewitt, D., Chizmadia, L., Grimm, R., and Prialnik, D. (2007). Water in the small bodies of the solar system. *Protostars and Planets V* 1, 863–878.

Johansen, A., Henning, T., and Klahr, H. (2006). Dust sedimentation and self-sustained Kelvin-Helmholtz turbulence in protoplanetary disk midplanes. *The Astrophysical Journal* 643(2), 1219.

Johansen, A., Oishi, J. S., Low, M.-M. M., Klahr, H., Henning, T., and Youdin, A. (2007). Rapid planetesimal formation in turbulent circumstellar disks. *Nature* 448(7157), 1022–1025.

Johansen, A. and Youdin, A. (2007). Protoplanetary disk turbulence driven by the streaming instability: nonlinear saturation and particle concentration. *The Astrophysical Journal* 662(1), 627.

Johnson, B. M., Guan, X., and Gammie, C. F. (2008). Addendum:"Orbital Advection by Interpolation: A Fast and Accurate Numerical Scheme for Super-Fast MHD Flows". *The Astrophysical Journal Supplement Series* 179(2), 553.

Kama, M., Trapman, L., Fedele, D., Bruderer, S., Hogerheijde, M., Miotello, A., Van Dishoeck, E., Clarke, C., and Bergin, E. (2020). Mass constraints for 15 protoplanetary discs from HD 1–0. *Astronomy & Astrophysics* 634, A88.

Kim, C.-G. and Ostriker, E. C. (2017). Three-phase interstellar medium in galaxies resolving evolution with star formation and supernova feedback (TIGRESS): algorithms, fiducial model, and convergence. *The Astrophysical Journal* 846(2), 133.

Kolmogorov, A. N. (1941). The local structure of turbulence in incompressible viscous fluid for very large Reynolds numbers. *Cr Acad. Sci. URSS* 30, 301–305.

Koyama, H. and Ostriker, E. C. (2009). Gas properties and implications for galactic star formation in numerical models of the turbulent, multiphase interstellar medium. *The Astrophysical Journal* 693(2), 1316.

Lecar, M., Podolak, M., Sasselov, D., and Chiang, E. (2006). On the location of the snow line in a protoplanetary disk. *The Astrophysical Journal* 640(2), 1115.

Li, R. and Youdin, A. N. (2021). Thresholds for Particle Clumping by the Streaming Instability. *The Astrophysical Journal* 919(2), 107.

Long, F., Herczeg, G. J., Pascucci, I., Drabek-Maunder, E., Mohanty, S., Testi, L., Apai, D., Hendler, N., Henning, T., Manara, C. F., et al. (2017). An ALMA survey of CO isotopologue emission from protoplanetary disks in Chamaeleon I. *The Astrophysical Journal* 844(2), 99.

Lynden-Bell, D. and Pringle, J. E. (1974). The evolution of viscous discs and the origin of the nebular variables. *Monthly Notices of the Royal Astronomical Society* 168(3), 603–637.

Lyra, W. and Umurhan, O. M. (2019). The initial conditions for planet formation: Turbulence driven by hydrodynamical instabilities in disks around young stars. *Publications of the Astronomical Society of the Pacific* 131(1001), 072001.

Mamajek, E. E. (2009). Initial Conditions of Planet Formation: Lifetimes of Primordial Disks. *AIP Conference Proceedings* 1158(1), 3–10.

Markiewicz, W., Mizuno, H., and Voelk, H. (1991). Turbulence induced relative velocity between two grains. *Astronomy and Astrophysics* 242, 286–289.

Masset, F. (2000). FARGO: A fast eulerian transport algorithm for differentially rotating disks. *Astronomy and Astrophysics Supplement Series* 141(1), 165–173.

Montmerle, T., Augereau, J.-C., Chaussidon, M., Gounelle, M., Marty, B., and Morbidelli, A. (2006). 3. Solar System formation and early evolution: the first 100 million years. *Earth, Moon, and Planets* 98(1), 39–95.

Myers, P. (1985). Molecular cloud cores. *Protostars and Planets II*, 81–103.

Nakagawa, Y., Sekiya, M., and Hayashi, C. (1986). Settling and growth of dust particles in a laminar phase of a low-mass solar nebula. *Icarus* 67(3), 375–390.

Nakamoto, T. and Nakagawa, Y. (1994). Formation, early evolution, and gravitational stability of protoplanetary disks. *The Astrophysical Journal* 421, 640–650.

Okuzumi, S. and Ormel, C. W. (2013). The fate of planetesimals in turbulent disks with dead zones. I. The turbulent stirring recipe. *The Astrophysical Journal* 771(1), 43.

Okuzumi, S., Tanaka, H., Kobayashi, H., and Wada, K. (2012). Rapid coagulation of porous dust aggregates outside the snow line: A pathway to successful icy planetesimal formation. *The Astrophysical Journal* 752(2), 106.

Ormel, C. and Cuzzi, J. (2007). Closed-form expressions for particle relative velocities induced by turbulence. *Astronomy & Astrophysics* 466(2), 413–420.

Pan, L. and Padoan, P. (2015). Turbulence-induced Relative Velocity of Dust Particles V. Testing Previous Models. *The Astrophysical Journal* 812(1), 10.

Perri, F. and Cameron, A. G. (1974). Hydrodynamic instability of the solar nebula in the presence of a planetary core. *Icarus* 22(4), 416–425.

Pinte, C., Price, D., Ménard, F., Duchêne, G., Christiaens, V., Andrews, S., Huang, J., Hill, T., Van Der Plas, G., Perez, L., et al. (2020). Nine localized deviations from Keplerian rotation in the DSHARP circumstellar disks: kinematic evidence for protoplanets carving the gaps. *The Astrophysical Journal Letters* 890(1), L9.

Pollack, J. B., Hubickyj, O., Bodenheimer, P., Lissauer, J. J., Podolak, M., and Greenzweig, Y. (1996). Formation of the giant planets by concurrent accretion of solids and gas. *icarus* 124(1), 62–85.

Pope, S. B. (2000). *Turbulent flows*. Cambridge university press.

Rappenglück, M. (2003). The anthropoid in the sky: Does a 32,000-year old ivory plate show the constellation Orion combined with a pregnancy calendar? *Uppsala Astronomical Observatory Reports* 59, 51.

Richardson, L. F. (1922). *Weather prediction by numerical process*. University Press.

Rucska, J. J. (2018). Numerical investigations of the early stages of planet formation. PhD thesis.

Rucska, J. J. (2022). Numerical Simulations of Planetesimal Formation. PhD thesis.

Sakurai, Y., Ishihara, T., Furuya, H., Umemura, M., and Shiraishi, K. (2021). Effects of the compressibility of turbulence on the dust coagulation process in protoplanetary disks. *The Astrophysical Journal* 911(2), 140.

San, O. and Maulik, R. (2018). Stratified Kelvin–Helmholtz turbulence of compressible shear flows. *Nonlinear Processes in Geophysics* 25(2), 457–476.

Schneider, J., Dedieu, C., Le Sidaner, P., Savalle, R., and Zolotukhin, I. (2011). Defining and cataloging exoplanets: the exoplanet. eu database. *Astronomy & Astrophysics* 532, A79.

Scott, J. F. (2022). Dynamic and static stability of a drop attached to an inhomogeneous plane wall. *Journal of Engineering Mathematics* 135(1), 1–32.

Sekiya, M. (1998). Quasi-equilibrium density distributions of small dust aggregations in the solar nebula. *Icarus* 133(2), 298–309.

Shakura, N. I. and Sunyaev, R. A. (1973). Black holes in binary systems. Observational appearance. *Astronomy and Astrophysics* 24, 337–355.

Simon, J. B., Armitage, P. J., Li, R., and Youdin, A. N. (2016). The mass and size distribution of planetesimals formed by the streaming instability. I. The role of self-gravity. *The Astrophysical Journal* 822(1), 55.

Simon, J. B., Bai, X.-N., Armitage, P. J., Stone, J. M., and Beckwith, K. (2013). Turbulence in the outer regions of protoplanetary disks. II. Strong accretion driven by a vertical magnetic field. *The Astrophysical Journal* 775(1), 73.

Simon, J. B., Beckwith, K., and Armitage, P. J. (2012). Emergent mesoscale phenomena in magnetized accretion disc turbulence. *Monthly Notices of the Royal Astronomical Society* 422(3), 2685–2700.

Simon, J. B. and Hawley, J. F. (2009). Viscous and resistive effects on the magnetorotational instability with a net toroidal field. *The Astrophysical Journal* 707(1), 833.

Simon, J. B., Lesur, G., Kunz, M. W., and Armitage, P. J. (2015). Magnetically driven accretion in protoplanetary discs. *Monthly Notices of the Royal Astronomical Society* 454(1), 1117–1131.

Squire, J. and Hopkins, P. F. (2018). Resonant drag instabilities in protoplanetary discs: the streaming instability and new, faster growing instabilities. *Monthly Notices of the Royal Astronomical Society* 477(4), 5011–5040.

Stone, J. M. and Gardiner, T. A. (2010). Implementation of the shearing box approximation in Athena. *The Astrophysical Journal Supplement Series* 189(1), 142.

Stone, J. M., Gardiner, T. A., Teuben, P., Hawley, J. F., and Simon, J. B. (2008). Athena: a new code for astrophysical MHD. *The Astrophysical Journal Supplement Series* 178(1), 137.

Teague, R., Guilloteau, S., Semenov, D., Henning, T., Dutrey, A., Pietu, V., Birnstiel, T., Chapillon, E., Hollenbach, D., and Gorti, U. (2016). Measuring turbulence in TW Hydrae with ALMA: methods and limitations. *Astronomy & Astrophysics* 592, A49.

Toomre, A. (1964). On the gravitational stability of a disk of stars. *The Astrophysical Journal* 139, 1217–1238.

Toro, E. F., Spruce, M., and Speares, W. (1994). Restoration of the contact surface in the HLL-Riemann solver. *Shock waves* 4(1), 25–34.

Turner, N. and Drake, J. (2009). Energetic protons, radionuclides, and magnetic activity in protostellar disks. *The Astrophysical Journal* 703(2), 2152.

Völk, H., Jones, F., Morfill, G., and Roeser, S. (1980). Collisions between grains in a turbulent gas. *Astronomy and Astrophysics* 85, 316–325.

Weidenschilling, S. (1977a). Aerodynamics of solid bodies in the solar nebula. *Monthly Notices of the Royal Astronomical Society* 180(2), 57–70.

Weidenschilling, S. (1977b). The distribution of mass in the planetary system and solar nebula. *Astrophysics and Space Science* 51(1), 153–158.

Whipple, F. L. (1972). On certain aerodynamic processes for asteroids and comets. In: *From plasma to planet*, 211.

Windmark, F., Birnstiel, T., Güttler, C., Blum, J., Dullemond, C. P., and Henning, T. (2012). Planetesimal formation by sweep-up: how the bouncing barrier can be beneficial to growth. *Astronomy & Astrophysics* 540, A73.

Yang, C.-C., Johansen, A., and Carrera, D. (2017). Concentrating small particles in protoplanetary disks through the streaming instability. *Astronomy & Astrophysics* 606, A80.

Yorke, H. W., Bodenheimer, P., and Laughlin, G. (1993). The formation of protostellar disks. I-1 M (solar). *The Astrophysical Journal* 411, 274–284.

Youdin, A. N. and Goodman, J. (2005). Streaming instabilities in protoplanetary disks. *The Astrophysical Journal* 620(1), 459.